

ULTRASONIC MEASUREMENT OF MEMBRANE FOULING DURING MICROFILTRATION OF NATURAL BROWN WATER

Thesis submitted in fulfilment of requirements for the degree of

Master of Technology in Engineering

at the

Cape Peninsula University of Technology

By

Mesuli Bonani Mbanjwa

March 2007

Supervisors:

Mrs. M. S. Sheldon (Cape Peninsula University of Technology)

Prof. R. D. Sanderson (University of Stellenbosch)

DECLARATION

I, the undersigned, hereby declare that the work contained in this thesis is my own original work and has not previously, in its entirety or in part, been submitted at any university for a degree.


.....

Signature

14 - 04 - 2007
.....

Date

ABSTRACT

The removal of the colour-causing natural organic matter (NOM) from natural brown water (NBW) to be used for drinking purposes is of paramount importance. One of the methods available to remove NOM from NBW is the use of pressure-driven membrane separation systems. One of the limitations in efficiently applying membrane filtration in the treatment of NOM-containing water is membrane fouling that is caused by foulants, such as NOM, that accumulate on the membrane surface and in the membrane pores. Microfiltration (MF), as a membrane separation system, is susceptible to severe membrane fouling during membrane filtration of NBW. Fouling is characterized by a rapid decline in permeate flux and loss of productivity.

Progress in developing more effective control and prevention of fouling is impeded by the absence of suitable fouling measurement and characterization techniques. An *in situ* method for measuring membrane fouling is necessary for detection of membrane fouling during MF of NBW at the earliest stages so that the corrective actions can be taken before fouling is permanently adsorbed onto the membrane surface.

In this study, an ultrasonic-based method was effectively used to detect and measure the growth of membrane fouling during MF of NBW, *in situ*. Fouling experiments results showed the formation of a new peak on the ultrasonic response echo signal due to the presence of a fouling layer on the surface of the membrane. The ultrasonic signals acquired during the in-situ detection of membrane fouling were analysed using wavelet transforms (WTs). Wavelet analysis was applied to differential signals to obtain additional information about fouling. Differential signals were calculated by subtracting the baseline measurement signals from the test signals. The presence of the fouling layer on membranes was verified by atomic force microscopy (AFM) and scanning electron microscopy (SEM) analyses of the fouled membranes.

ACKNOWLEDGEMENTS

Prof. RD Sanderson at the UNESCO Associated Centre for Macromolecules and Materials, Department of Chemistry and Polymer Science, University of Stellenbosch, for encouragement and advice.

Mrs. MS Sheldon at the Department of Chemical Engineering, Cape Peninsula University of Technology, for her patience, support and enthusiasm.

Dr. FJ Reineke for his guidance and mentorship throughout this study, and for coordinating my visit to Germany. May his soul rest in peace.

Water Research Commission (WRC) for financially supporting the project.

Dr. MJ Hurndall for assistance with editing this thesis.

Prof. LJ Balk (Bergische Universität Wuppertal, Germany) for affording me the wonderful opportunity to experience international research.

Proffs DS McLachlan (University of the Stellenbosch) and **W Scharff** (IfU GmbH, Germany) for their support.

Dr. SK Sikder and **Mr. DA Keuler** at Polymer Science, University of Stellenbosch.

Dr. O Sergeev (Bergische Universität Wuppertal, Germany), **Mrs. M Waldron** (University of Cape Town); **Mrs. E Spicer** (University of Stellenbosch); **Dr. M Meincken** (University of Stellenbosch); **Mr. M Louw** and his staff (CSIR, Stellenbosch).

Staff and students at Polymer Science, University of Stellenbosch.

My friends and family for their support, especially my mother, **Joyce Bulelwa**, whose efforts and toils never went unappreciated.

TABLE OF CONTENTS

DECLARATION	i
ABSTRACT	ii
ACKNOWLEDGEMENTS	iv
TABLE OF CONTENTS	v
LIST OF ABBREVIATIONS	viii
LIST OF SYMBOLS	x
LIST OF TABLES	xiii
LIST OF FIGURES	xiv
CHAPTER 1	1
INTRODUCTION	1
1.1 REMOVAL OF NATURAL ORGANIC MATTER FROM WATER	1
1.2 PROBLEM STATEMENT AND RATIONALE	2
1.3 RESEARCH OBJECTIVES	4
1.4 THESIS LAYOUT	5
CHAPTER 2	6
MEMBRANE FILTRATION: LITERATURE REVIEW AND THEORETICAL BACKGROUND	6
2.1 PRESSURE-DRIVEN MEMBRANE PROCESSES	6
2.2 FUNDAMENTALS OF MEMBRANE TRANSPORT	7
2.2.1 Solute rejection.....	7
2.2.2 Flux definition	7
2.2.3 Critical flux concept	10
2.3 MODES OF OPERATION	10
2.3.1 Dead-end vs. cross-flow filtration	10
2.3.2 Constant flux vs. constant pressure operation.....	12
2.4 CONCENTRATION POLARISATION AND MEMBRANE FOULING	13
2.4.1 Resistance-in-series model.....	14
2.4.2 Boundary layer film model.....	14
2.4.3 Pore blocking.....	16
2.5 FOULING MITIGATION	17
2.5.1 Fouling indices	17
2.5.2 Analysis of fouled membranes	18
2.5.3 Process monitoring of membrane fouling	19

2.5.4	Prevention and removal	21
2.6	CHARACTERISATION OF MEMBRANE FOULING BY MICROSCOPY	22
2.6.1	Scanning electron microscopy (SEM)	22
2.6.2	Atomic force microscopy (AFM)	23
CHAPTER 3	24
MEASUREMENT OF MEMBRANE FOULING BY ULTRASONIC METHOD: LITERATURE REVIEW		24
3.1	INTRODUCTION	24
3.2	BASIC ULTRASONIC PRINCIPLES	25
3.2.1	Types of waves	26
3.2.2	Ultrasound and ultrasonic waves	26
3.2.3	Reflection and transmission of waves	27
3.3	ULTRASONIC EQUIPMENT.....	32
3.3.1	Ultrasonic equipment for used for research	32
3.3.2	Ultrasonic transducers	33
3.3.3	Transducer sound field.....	34
3.3.4	Theoretical resolution of transducers	36
3.4	APPLICATION OF ULTRASONICS IN MEMBRANE FOULING STUDIES	36
3.5	WAVELET ANALYSIS AND INTEPRETATION OF ULTRASONIC SIGNALS	38
3.5.1	Introduction.....	38
3.5.2	Time-frequency representation of signals	39
3.5.3	Fourier transforms	40
3.5.4	Wavelet analysis	40
3.5.5	Agu-vallen wavelet software	41
CHAPTER 4	43
EXPERIMENTAL: MATERIALS AND METHODS		43
4.1	INTRODUCTION	43
4.2	EXPERIMENTAL EQUIPMENT.....	43
4.2.1	MF system.....	44
4.2.2	Ultrasonic measurement system.....	47
4.2.2.1	Pulser-receiver	47
4.2.2.2	Oscilloscope	49
4.2.2.3	Ultrasonic transducer	49
4.3	MATERIALS.....	50
4.3.1	NBW source	50
4.3.2	Membranes	52
4.4	METHODS.....	55
4.4.2	Ultrasonic measurements	55
4.4.3	Data processing and analysis	56
4.4.4	Fouling layer analysis.....	57

CHAPTER 5	58
RESULTS AND DISCUSSION	58
5.1 INTRODUCTION	58
5.2 ULTRASONIC RESPONSES.....	58
5.3 CROSS-FLOW FOULING EXPERIMENTS.....	60
5.3.1 Test conditions	61
5.3.2 Low cross-flow experiment (Re = 965)	61
5.3.2.1 Permeate flux decline	62
5.3.2.2 Ultrasonic response	63
5.3.2.3 WTs of ultrasonic signals	66
5.3.3 High Re cross-flow experiments (Re = 19 220)	75
5.3.3.1 Permeate flux decline	76
5.3.3.2 Ultrasonic response	77
5.3.3.3 WTs of differential signals.....	82
5.4 DEAD-END FOULING EXPERIMENTS	86
5.4.1 Test conditions	86
5.4.2 Permeate flux	87
5.4.3 Ultrasonic response	88
5.4.4 Wavelet transforms	89
5.5 CHARACTERISATION OF FOULED MEMBRANES BY MICROSCOPY.....	90
5.5.1 Scanning electron microscopy	90
5.5.2 Atomic force microscopy	91
CHAPTER 6	96
CONCLUSIONS AND RECOMMENDATIONS	96
REFERENCES	97
APPENDIX 1.....	105
ULTRASONIC FOULING/PLUGGING INDEX METER.....	105
APPENDIX 2.....	109
USER MANUAL FOR THE LABVIEW MEASUREMENT PROGRAM.....	109
APPENDIX 3.....	122
SUMMARY OF PRELIMINARY ULTRASONIC RESULTS.....	122
APPENDIX 4.....	125
LIST OF PUBLICATIONS: PAPERS AND PRESENTATIONS	125

LIST OF ABBREVIATIONS

ACH	Analog channel
AICH	Analog input channel
AFM	Atomic force microscope/microscopy
CP	Concentration polarization
CSTR	Continually stirred tank reactor
DOC	Dissolved organic carbon
EDS	<i>Electron dispersive spectroscopy</i>
FA	Fulvic acids
FT	Fourier transform
GAC	Granular activated carbon
HA	Humic acids
HS	Humic substance
MF	Microfiltration
NBW	Natural brown water
MFI	Modified fouling index
MMCO	<i>Molecular mass cut-off</i>
NDT	Non-destructive testing
NF	Nanofiltration
NOM	Natural organic matter
Nylon	Dupont trade name for polyamide 6,6
PAC	Powdered activated carbon
PRF	Preamplifier radio frequency
PVDF	Polyvinylidene fluoride
PWF	Pure water flux
PZT	<i>Lead zirconate titanate</i>
Re	Reynolds number
RF	Radio frequency
RO	Reverse osmosis
SDI	Silt density index
SEM	Scanning electronic microscope/ microscopy

SPM	Scanning probe microscopy
STFT	Short time Fourier transform
TMP	Transmembrane pressure
TOC	Total organic carbon
UFPIM	Ultrasonic fouling/plugging index meter
UF	Ultrafiltration
URM	Ultrasonic reflection modelling
UTDR	Ultrasonic-time-domain-reflectometry
UV/UV-VIS	Ultraviolet/Ultraviolet visible
V	volts
WFT	Windowed Fourier transform
WT	Wavelet transform
XPS	X-ray photoelectron spectroscopy
XRD	X-ray diffraction

LIST OF SYMBOLS

A_m	Effective membrane surface area
C_{iBL}	Concentration of material i in the bulk liquid
C_{iG}	Concentration of material i in the gel polarisation layer
C_{ip}	Concentration of material i in the permeate
C_{iw}	Concentration of material i at the membrane wall
C_r	Coefficient/amplitude of reflected wave
C_t	Coefficient/amplitude of transmitted wave
c	Velocity of sound wave in a medium
D	Transducer face diameter
D_i	Diffusion coefficient for material
E	Energy transmitted by a wave
F_0	Cantilever resonance frequency
f	Frequency
G_E	Fraction of reflected wave energy
G_E'	Fraction of reflected wave energy at angle less than the first critical angle
Δh	Vertical deflection of AFM probe
J	Permeate flux
J_c	Critical flux
J_{lim}	Limiting flux
k	Flux constant
l	Length of membrane pore
N_R	Near field distance
N	Number of pores per membrane square centimetre
ΔP	Differential pressure
P_i	The sound pressures of the incident wave
P_p	Permeate pressure
P_r	The sound pressures of the reflected wave
P_{ret}	Retentate pressure
P_s	Sound pressure
P_t	The sound pressures of the transmitted wave

q	Flow of a volume of liquid
Q	Particle displacement velocity
Q_i	Particle velocity of the incident wave
Q_r	Particle velocity of the reflected wave
Q_t	Particle velocity of the transmitted wave
r_i	Rejection of material i by a membrane
R	Distance between the sources (transducer)
R_C	Cake layer resistance
R_{CP}	Concentration polarisation resistance
R_E	Fraction of reflected wave energy
R_E'	Fraction of reflected wave energy at angle less than the first critical angle
R_F	Fouling resistance
R_g	Gel resistance
R_M	Clean membrane resistance
R_r	Reversible resistance
R_T	Total resistance
T_E	Fraction of transmitted wave energy
T_E'	Fraction of transmitted wave energy at angle less than the first critical angle
Δt	Difference in arrival times of a sound wave
dT	Change in time
ΔS	Thickness of material
u	Wave propagation constant
V_p	Permeate volume
W	Oscillations of molecules/atoms leading to a travelling wave
W_0	Maximum amplitude of excess wave pressure
x	Distance of amplitude and pressure variation
z	Acoustic impedance of material
z_T	Acoustic impedance of a transducer active element

Greek letters

α	Critical angle of wave reflection
δ	Boundary layer thickness
$\varepsilon/\varepsilon_m$	Porosity/Membrane porosity
$\Delta\Pi$	Differential osmotic pressure
ρ	Density of the material
τ	Time of wave's arrival (period)
μ	Viscosity of solution
ω	$2\pi/\tau$, rotational frequency
ω_{op}	Frequency of the self-oscillation of source (transducer) (radian per second)
σ	WFT constant
ζ	AFM probe spring constant
φ	Incident angle of transducer beam
ψ	Signal windowing time

LIST OF TABLES

CHAPTER 2

Table 2.1	Techniques for in situ investigation of membrane fouling and concentration polarisation	20
-----------	---	----

CHAPTER 3

Table 3.1	Types of waves	26
Table 3.2	Typical values of the percentage of ultrasonic energy reflected at a perfect boundary of normal incidence	31

CHAPTER 4

Table 4.1	Typical composition of the NBW from Buffelsrivier Municipal Reservoir	49
Table 4.2	Settings of wavelet calculations by AGU Vallen wavelet software	55

CHAPTER 5

Table 5.1	Summary of test conditions for the fouling experiment at low Re	60
Table 5.2	Summary of test conditions for the dead-end fouling experiment	85

LIST OF FIGURES

CHAPTER 2

Figure 2.1	Illustration of dead-end filtration	10
Figure 2.2	Illustration of cross-flow filtration	11
Figure 2.3	Illustration of constant flux and constant pressure operating conditions	12
Figure 2.4	Illustration of the concept of the boundary layer and concentration polarisation at a membrane surface	15
Figure 2.5	Schematic presentation of the pore blocking mechanism suggested by Jacobs <i>et al.</i> (2000)	16
Figure 2.6	Principle of AFM measurement	23

CHAPTER 3

Figure 3.1	Three frequency ranges of the acoustic spectrum	27
Figure 3.2	Reflection and transmission of a sound wave at a normal incidence on a boundary between two media of specific acoustic impedance, z_1 and z_2	29
Figure 3.3	Schematic presentation of pulser/receiver-oscilloscope connection for pulse-echo operation	32
Figure 3.4	Cut-away view showing internal components of an ultrasonic transducer	34
Figure 3.5	Illustration of a near field and far field in a transducer beam	36
Figure 3.6	Illustration of the principle of multiple wave reflections during ultrasonic measurement of fouling on a flat membrane test module	38
Figure 3.7	Ultrasonic time-domain response for the set-up in Figure 3.6	38
Figure 3.7	Several different families of wavelets. These figures were created using WaveLab	41

CHAPTER 4

Figure 4.1	Schematic representation of the MF system	44
------------	---	----

Figure 4.2	Top view of flat-sheet test module used in the MF system	45
Figure 4.3	Side view of the flat-sheet test modules used in the MF system	45
Figure 4.4	A photograph of the ultrasonic equipment used in the study showing the Panametrics 5058PR pulser-receiver, the HP 54602B oscilloscope and the computer	47
Figure 4.5	Schematic of the connections between the transducer, the pulser-receiver, the oscilloscope and the computer	48
Figure 4.6	Photograph of the Hewlett Packard 54602B oscilloscope	49
Figure 4.7	Typical composition of dam water	50
Figure 4.8	Typical composition of river water	52
Figure 4.9	Cross-section (microtome cut) through a clean and dry 0.2 μm nylon membrane	53
Figure 4.10	Electron micrographs of a clean Biodyne A membrane (0.2 μm) at 10 000 times magnification	53
Figure 4.11	AFM image of Biodyne A membrane	54
Figure 4.12	A graph of PWF plotted against TMP for a Biodyne A membrane	54

CHAPTER 5

Figure 5.1	Ultrasonic response spectrum of the flat-sheet filtration module	59
Figure 5.2	Ultrasonic response of a clean membrane	58
Figure 5.3	Flux decline as a time function for the low cross-flow velocity ($Re = 965$) fouling experiment	62
Figure 5.4	Ultrasonic response waveforms for low cross-flow MF fouling experiment ($Re = 965$)	63
Figure 5.5	Figure 5.5: Increase of fouling layer thickness and fouling peak amplitude with time ($Re = 965$)	64
Figure 5.6	Increase of fouling resistance as fouling layer thickness increases time ($Re = 965$)	65
Figure 5.7	WT of an ultrasonic signal from a clean membrane	66

Figure 5.8	3D representation of the WT of an ultrasonic signal of a clean membrane	67
Figure 5.9	WTs of the ultrasonic signals after 1min, 60 min and 240 min of operation (Re = 965, cross-flow fouling experiment)	69
Figure 5.10	WTs of the ultrasonic signals after 420 min, 600 min and 780 min of operation (Re = 965, cross-flow fouling experiment)	70
Figure 5.11	3D representation of the WT of an ultrasonic signal for a fouled membrane corresponding to the wavelet after 780 min of operation	71
Figure 5.12	Differential signals calculated from original signals in Figure 5.4	71
Figure 5.13	WTs of differential waveforms for the low cross-flow (Re = 965) fouling experiment after 10 s, 1 min and 60 min of operation	73
Figure 5.14	WTs of differential waveforms for the low cross-flow (Re = 965) fouling experiment after 240 min, 420 min, and 780 min of operation	74
Figure 5.15	Flux decline as a time function for the high cross-flow velocity (Re = 19 220) fouling experiment	76
Figure 5.16	Changes in the ultrasonic response during high Re cross-flow MF fouling experiment (Re = 19 220)	77
Figure 5.17	WTs of the ultrasonic signals at 0 min and after 10 s, 0.5 min and 1 min of operation (Re = 19 220, cross-flow fouling experiment)	79
Figure 5.18	WTs of the ultrasonic signals after 5 min, 60 min and 120 min of operation (Re = 19 220, cross-flow fouling experiment)	80
Figure 5.19	WTs of the ultrasonic signals after 360 min, 960 min and 1440 min of operation (Re = 19 220, cross-flow fouling experiment)	81
Figure 5.20	WTs of differential waveforms after 10s, 0.5 min, and 5 min	

	of operation ($Re = 19\ 220$, cross-flow fouling experiment)	83
Figure 5.21	WTs of differential waveforms after 30 min, 120 min, and 360 min of operation ($Re = 19\ 220$, cross-flow fouling experiment).	84
Figure 5.22	WTs of differential waveforms for the high Re cross-flow fouling experiment after 720 min, 960 min and 1440 of operation ($Re = 19\ 220$, cross-flow fouling experiment)	85
Figure 5.23	Flux decline as a time function for the dead-end fouling experiment	87
Figure 5.24	Changes in the ultrasonic response signals for the dead-end MF fouling experiment	88
Figure 5.25	WT of ultrasonic response signals at the start of the operation (0 min) and after 540 min of operation	89
Figure 5.26	SEM images of $0.2\ \mu\text{m}$ porous surface of nylon membrane after a fouling experiment	90
Figure 5.27	AFM cross-section image of the clean membrane	91
Figure 5.28	AFM cross-section image of the fouled membrane	92
Figure 5.29	AFM Topography images of a fouled membrane: (a) cross-flow filtration	93
Figure 5.30	3D AFM topography images of a fouled membrane	94f
Figure 5.31	Section view on AFM topography image of a fouled membrane	95

CHAPTER 1

INTRODUCTION

1.1 REMOVAL OF NATURAL ORGANIC MATTER FROM WATER

Natural organic matter (NOM) is present in natural waters as a result of the degradation of plants and micro-organisms and the synthesis activities of micro-organisms (Carroll *et al.*, 2002; Combe *et al.*, 1998). Although NOM is a very complex macromolecular material, it generally comprises of polyphenolic molecules with molecular weights that range from 5 000 to 50 000 daltons. NOM-containing natural water is referred to as natural brown water (NBW) because of its characteristic brown colour. Consumers supplied with potable NBW tend to reject it because of its colour, regardless of its suitability for use from the sanitary perspective (Swartz & De Villiers, 1998). Moreover, potentially carcinogenic compounds, such as organochlorines, can result during disinfection of NBW by chlorination (Carroll *et al.*, 2002; Maartens *et al.*, 1999). It is for these reasons therefore that there is a paramount concern to remove NOM from water to be supplied (with or without chlorination) for drinking purposes.

The use of semi-permeable pressure-driven membranes has found growing acceptance as a means by which to remove NOM and other pollutants from water. Pressure-driven membrane separation processes, which include microfiltration (MF), ultrafiltration (UF), nanofiltration (NF), and reverse osmosis (RO) are considered as alternatives to conventional methods (such as ion exchange, distillation, sand filtration, coagulation and settling) for water and wastewater treatment. MF is used to remove turbidity, including particulate contaminants, such as clay, algae, bacteria and cryptosporidia. MF can also retain colloid-associated dissolved compounds and, to a small extent, NOM (Meier-Haack *et al.*, 2003; Schäfer *et al.*, 2000b). MF is an alternative to coagulation, flocculation and sedimentation processes because of its ease of operation control, lower maintenance and lower sludge production (Jacangelo &

Buckley, 1996). MF is more cost effective than UF and NF in removing turbidity and micro-organisms and is, therefore, very useful for the pre-treatment of water (Schäfer *et al.*, 2000b).

The major limitation during the treatment of NBW by MF is the severe fouling of membranes, caused by retained matter on the membrane surface and within the membrane pores. Fouling results in a decline in the permeate flux, and the consequential reduction in productivity and increased operational costs. The presence of particulate matter, colloids, multivalent ions and organic material is a cause of substantial fouling in membranes used in the purification of NBW. *Membrane fouling is generally described as the deposition and accumulation of contaminants on a membrane surface and/or within a porous membrane, and the consequent inhibition of the passage of water. Fouling during membrane filtration of NBW is mainly attributed to NOM (Schäfer et al., 2000a, 2000b & 2000c).*

1.2 PROBLEM STATEMENT AND RATIONALE

Membrane fouling can reduce the performance of the MF process during the membrane filtration of NBW by causing decline in permeate flux (Carroll et al., 2002; Meier-Haack et al., 2003). In order to effectively control or prevent membrane fouling, suitable techniques for measuring membrane fouling during operation are a prerequisite (Mairal et al., 2000; Shetty & Chellam, 2003; Swart et al., 1998). The conventional method of monitoring fouling during operation, to date, depends on the observation of permeate flux and pressure changes. Although these changes indicate the presence of membrane fouling or concentration polarisation, this method does not provide information about the characteristics of the membrane fouling. In order to characterise membrane fouling, a destructive membrane autopsy procedure is performed and the fouled membrane is removed and investigated using analytical methods such as scanning electron microscopy (SEM) and atomic force microscopy (AFM) so as to gather information about the nature of membrane fouling (Dudley & Darton, 1996). During such an autopsy procedure the membrane filtration process has

to be stopped, and hence the productivity is reduced. Furthermore, a membrane on which an autopsy has been performed cannot be re-used in the filtration process.

Essentially, a technique that is suitable for the measurement and monitoring of membrane fouling needs to be non-destructive and able to give information about the nature of membrane fouling *in situ*. The suitability of the ultrasonic measurement technique as a non-interfering method for measuring membrane fouling, *in situ*, has been well investigated (Koen, 2000; Li, 2002; Li *et al.*, 2002a, 2002b, 2002c, 2002d, 2002e, 2003 & 2005; Mairal *et al.*, 1999 & 2000; Peterson *et al.*, 1998; Reinsch *et al.*, 2000). Ultrasonic measurements are based on the propagation of sound waves which are generated at frequencies above 20 kHz.

The signals obtained using standard ultrasonic non-destructive testing instruments, such as those used in the characterisation of membrane fouling, are represented in a time-amplitude domain. However, it is necessary to be able to determine all the frequencies present in a transient ultrasonic signal, especially when non-homogeneous materials, such as flaws in solid materials, composite materials, membranes, fouling layers, and their structures are being investigated. Mathematical functions called wavelet transforms (WTs), also known as wavelets, can be used to represent data from ultrasonic signals in both time and frequency domains, simultaneously (Graps, 1995). Wavelets have been found to be useful in the analysis and processing of ultrasonic signals obtained during testing of thin multilayer structures (Angrisani & Daponte, 1997).

The ultrasonic method is a useful technique for measuring and detecting membrane fouling and its progression caused by NOM and other potential foulants present in NBW during microfiltration of NBW, *in situ*. Wavelet transforms, as applied to the ultrasonic signals from fouling measurement can be applied to improve the use of the ultrasonic technique by providing information in the time-frequency domain.

1.3 RESEARCH OBJECTIVES

The main objective of this study was to use the ultrasonic measurement technique to detect and measure membrane fouling during MF of NBW. Results obtained were then to be compared to the results of existing methods used for the detection of fouling, namely permeate flux decline and morphological analysis. The following specific goals were set in order to achieve the overall objective:

1. Based on previous studies (Li, 2002), design and develop a MF set-up suitable for use in fouling experiments and ultrasonic measurements.
2. Conduct membrane fouling experiments on the designed experimental set-up by filtering NBW collected from a NOM-containing water source.
3. Record the ultrasonic and hydrodynamic data during the experiments.
4. Apply the wavelet analysis technique to the analysis and interpretation of ultrasonic data.
5. Identify membrane fouling on membranes used for fouling experiments, using SEM and AFM.
6. Use the hydrodynamic technique (permeate flux monitoring) to correlate results of fouling measurements obtained using the ultrasonic technique.

1.4 THESIS LAYOUT

This thesis is organised into six chapters. Chapter 1 gives an introduction to the research work and states the objectives. The main focus of this chapter is the formulation of the problem statement and stating the research goals. Chapter 2 presents the theoretical background and literature review to the pressure-driven membrane processes. Chapter 3 gives the theoretical and technical background to the application of the ultrasonic technique in the measurement of fouling. Chapter 4 contains the experimental details: materials and methods. In Chapter 5 results are presented and discussed. These results were published in *Journal of Membrane Science* Vol. 271 pp 125- 139 (2006). Conclusions and recommendations are presented in Chapter 6. All references are listed at the end of the document. There are four appendices that follow.

CHAPTER 2

MEMBRANE FILTRATION: LITERATURE REVIEW AND THEORETICAL BACKGROUND

2.1 PRESSURE-DRIVEN MEMBRANE PROCESSES

Pressure-driven membrane processes are membrane systems in which pressure is used as a driving force to obtain transport of a fluid through a semi-permeable barrier or membrane. The part of the fluid that passes through the permeable membrane is the filtrate or permeate and the fluid composed of the elements that have been progressively rejected or that do not pass through is the retentate (also referred to as the concentrate). The pressure difference between the feed-side pressure and the permeate pressure across the membrane is referred to as the transmembrane pressure (TMP) or differential pressure (ΔP). ΔP is the driving force for the membrane separation.

Pressure-driven membrane separation processes are classified according to the pore sizes of the membranes or the sizes of particles that are retained by the membrane, and the operating pressures, into MF, UF, NF and RO.

- MF is a separation process that operates at low pressures of 30 to 330 kPa and can retain particles with sizes above 0.1 μm .
- UF operates between 50 and 1 000 kPa and separates materials in the range of 0.001 to 0.1 μm .
- NF is a high-pressure membrane separation process used for separating materials less than 0.001 μm in size. NF is growing in popularity, and is regarded as an alternative to RO as it uses less energy than RO. Typical NF operating pressures are between those of UF and RO.
- RO membranes are permeable to water but not permeable to dissolved ions. RO separation is based on the principle of reversal of the natural osmosis process and operates at high pressures between 350 kPa and 10 000 kPa.

2.2 FUNDAMENTALS OF MEMBRANE TRANSPORT

2.2.1 Solute rejection

Rejection (r_i) of any solute i in a solution separated by a semi-permeable membrane can be defined by equation (2.1). C_{BL} is the concentration in the bulk liquid and C_p is the permeate concentration.

$$r_i = 100 \left(1 - \frac{C_{iP}}{C_{iBL}} \right) \quad (2.1)$$

The formation of a layer or cake on the membrane surface results in the creation of another 'membrane layer', which can then reject particles smaller than the pore size of the original membrane. Therefore, the true membrane rejection is usually higher than the one defined by equation (2.1).

2.2.2 Flux definition

Permeate flux (or flux) is defined as the rate at which the permeate passes through a unit area of the membrane. Flux is the most critical parameter in the characterisation of membranes. Instantaneous flux is defined by equation (2.2), where V_p is the permeate volume, t is the filtration time and A_m is the effective membrane surface area.

$$J \equiv \frac{1}{A_m} \frac{dV_p}{dt} \quad (2.2)$$

In pressure-driven membrane filtration where the ΔP is the driving force, the flux (J) is described by Darcy's Law (Baker, 2004):

$$J = k \Delta P \quad (2.3)$$

k is the flux constant, which is determined by properties of the membrane, ΔP is the differential pressure and can be calculated using equation (2.4):

$$\Delta P = 0.5(P_f + P_{ret}) - P_p \quad (2.4)$$

P_f , P_{ret} and P_p are the feed, retentate and permeate pressures, respectively.

The maximum flux that can be achieved during filtration if the ΔP is increased indefinitely is referred to as the limiting flux (J_{lim}).

Another definition of flux can be derived from the pore flow model. The pore flow model is based on the Hagen-Poiseuille equation and describes the flow of a liquid (q), with a viscosity μ , through a membrane with a number of cylindrical capillary pores with a diameter d_p and length ℓ .

$$q = \frac{\pi d_p^4 \Delta P}{128 \mu \ell} \quad (2.5)$$

Flux, through a number of pores (N), per square centimeter of membrane, is then expressed as:

$$J = N \frac{\pi d_p^4 \Delta P}{32 \mu \ell} \quad (2.6)$$

For a membrane area of porosity, ϵ , that has pores with equal diameter, d_p , the number of pores per square centimeter is inversely proportional to the square of the pore diameter:

$$N = \frac{\epsilon^4}{\pi d_p^2} \quad (2.7)$$

By combination of the equations (2.6) and (2.7), the flux can be given by:

$$J = \frac{\epsilon_m^4 d_p^2 \Delta P}{32 \mu \ell} \quad (2.8)$$

where ϵ_m is the membrane porosity.

This model, however, does not account for flux limitations that are influenced by factors such as friction or resistances to permeate flow.

The basic equation that accounts for the flow losses is equation (2.9). The flux of pure water through a tortuous porous barrier under laminar conditions is inversely proportional to the water viscosity (μ) and the resistance of the clean membrane (R_M). This flux is sometimes referred to as pure water flux (PWF) and can be determined experimentally (Baker, 2004).

$$J = \frac{\Delta P}{\mu R_M} \quad (2.9)$$

This definition can be expanded into a resistance-in-series model, which is discussed in subsection 2.4.1. For solutions where the retained material has a differential osmotic pressure ($\Delta\Pi$) acting against the differential pressure, flux is expressed as:

$$J = \frac{\Delta P - \Delta\Pi}{\mu R_M} \quad (2.10)$$

Equation (2.10) is called the osmotic pressure model. In MF, the rejected solutes are usually large and have a small osmotic pressure and therefore the osmotic pressure term is negligible (Baker, 2004).

Generally, a decline in permeate flux is a good indicator of the presence of fouling or concentration polarisation during membrane filtration. During operation, the flux decreases exponentially as a function of time.

2.2.3 Critical flux concept

The theory of critical flux (J_c) emerged in the mid 1990's (Field *et al.*, 1995). It was defined as that flux, in MF, below which a flux decline is not observed and above which fouling is observed. There are two distinct forms of critical flux: the strong form and the weak form (Field *et al.*, 1995). The strong form comes into play when the flux, up to a point, is equivalent to the corresponding pure water flux at the same pressure. The weak form exists when the flux deviates from the pure water flux, but increases linearly with pressure.

2.3 MODES OF OPERATION

2.3.1 Dead-end vs. cross-flow filtration

The separation process can be achieved in either cross-flow or dead-end mode of operation. In dead-end, fundamentally, all of the fluid entering the system has to pass through as permeate. This concept is illustrated in Figure 2.1. Dead-end filtration is an energy efficient mode and is suitable for fluids that have little membrane fouling potential (Jacobs *et al.*, 2000).

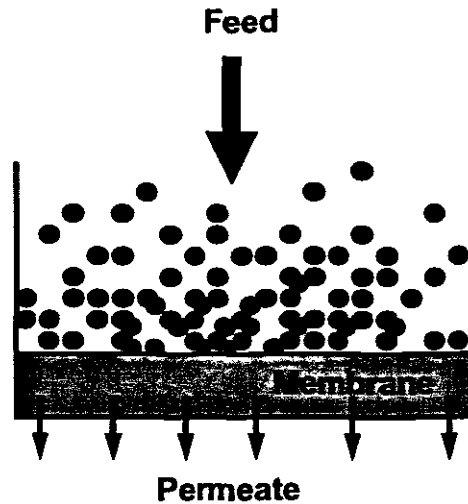


Figure 2.1: Illustration of dead-end filtration.

In cross-flow mode (Figure 2.2), the effluent is fed tangentially to the surface of the membrane and most of the fluid passes through as retentate and less of the feed passes through as permeate. Due to the shear exerted by the cross-flow velocity of the fluid, the foulant particles are scoured from the surface of the membrane. This mode of filtration is used to minimise particulate matter from settling on to the membrane surface and to stabilise flux decline rates (Jacobs *et al.*, 2003).

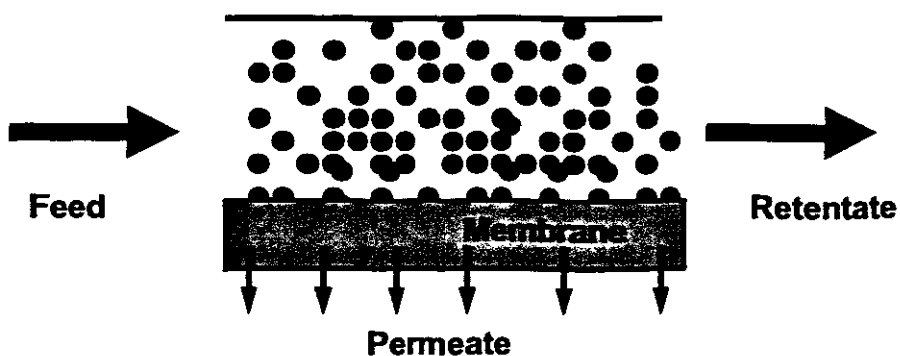


Figure 2.2: Illustration of cross-flow filtration.

2.3.2 Constant flux vs. constant pressure operation

Membrane systems can also be operated by achieving a constant flux or a constant pressure (Jacobs *et al.*, 2003). The difference in these two approaches is illustrated in Figure 2.3. These strategies can be achieved in either dead-end or cross-flow modes. The ensuing combinations are discussed in Section 2.3.3.

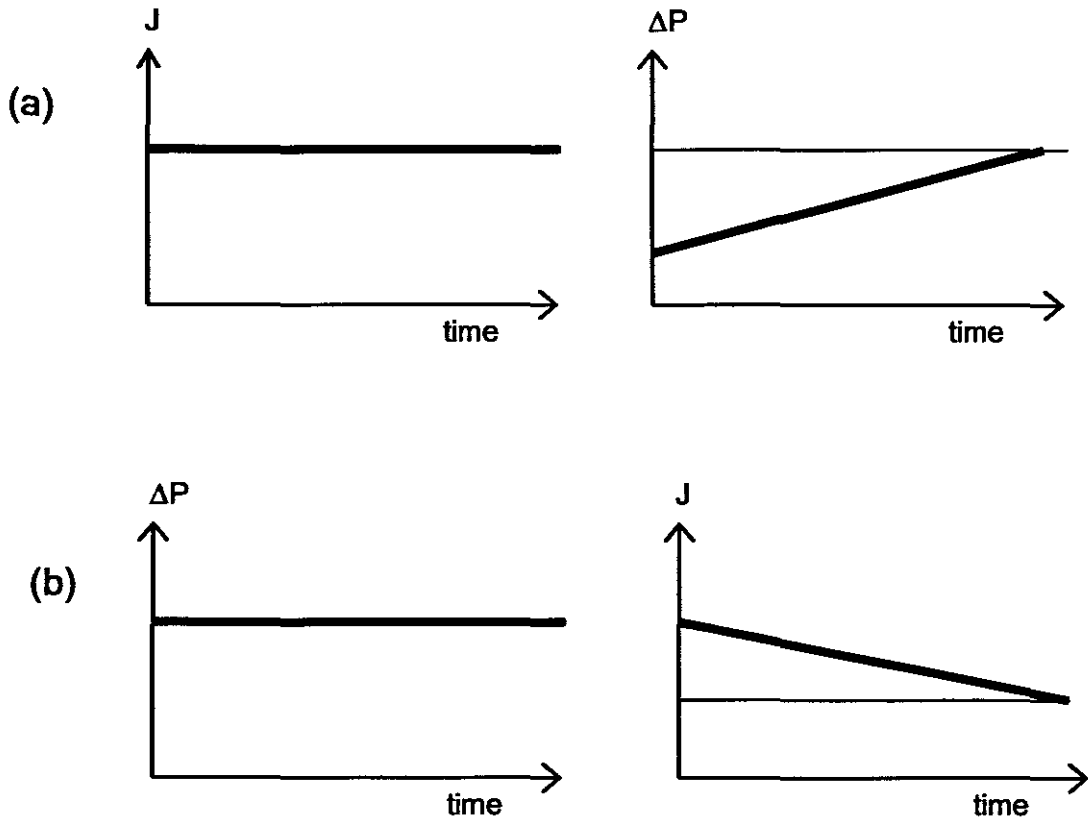


Figure 2.3: Illustration of (a) constant flux and (b) constant pressure operating conditions (Jacobs *et al.*, 2003).

Figure 2.3 (a) represents the operation of the membrane under constant flux conditions - there is a gradual increase in ΔP as a function of time. This increase is caused by the increasing resistance as a result of fouling accumulation on the surface of the membrane. This action is continued until a pressure limit is reached and then membrane cleaning strategies are required (Jacobs *et al.*, 2003).

The operation under constant ΔP conditions is illustrated in Figure 2.3 (b). The flux declines during operation as a function of time. When the flux decline reaches a minimum point due to fouling resistance, cleaning strategies need to be employed. This approach was used in the present study in order to monitor resultant flux decline caused by membrane fouling.

A membrane plant or system may be operated in the following permutations, as described by Jacobs *et al.* (2000):

- constant ΔP conditions in a cross-flow or dead-end filtration mode
- constant flux conditions in a cross-flow or dead-end filtration mode.

A condition with constant ΔP in cross-flow filtration is the most common approach to membrane filtration (Jacobs *et al.*, 2000). Although the shear exerted by cross-flow velocity helps to destabilise concentration polarisation and/or fouling, there is eventually a dominance of fouling resistance and, therefore, the subsequent flux decline.

As mentioned, it is this approach that was used in this study, together with that of constant ΔP in a dead-end filtration mode.

2.4 CONCENTRATION POLARISATION AND MEMBRANE FOULING

Concentration polarisation and membrane fouling are accepted as the primary causes of flux decline during the operation of pressure-driven membranes. Mathematical models that seek to describe membrane filtration have to take into account these factors, among others. There are numerous mathematical models that have been developed to describe concentration polarisation and fouling in various membrane systems. Some of these mathematical equations are very complex and can often be difficult, as well as time-consuming to handle. However, the model and the boundary layer film model are the basic and most widely used models to describe flux changes in systems due to

concentration polarisation and fouling in membrane systems (Baker, 2004). With applicable assumptions, these equations can then be expanded or simplified for a specific membrane system.

2.4.1 Resistance-in-series model

The PWF of a filtration system is described by equation (2.9). For systems where concentration polarisation and fouling have taken place, flux is given by the resistance-in-series model (Baker, 2004):

$$J = \frac{\Delta P}{\mu(R_M + R_{CP} + R_F)} \quad (2.11)$$

R_{CP} and R_F are the additional resistances from concentration polarisation and fouling effects, respectively. The fouling resistance, R_F , can either be from internal pore fouling (R_P) and/or from the presence of the cake layer (R_C). Then equation (2.11) becomes:

$$J = \frac{\Delta P}{\mu(R_M + R_{CP} + R_P + R_C)} \quad (2.12)$$

2.4.2 Boundary layer film model

Accumulation of solutes in solution on the surface of a membrane from the bulk liquid or solution, due to convective transport of both the solute and the solvent, is called concentration polarisation. The concentration gradients due to concentration polarisation are assumed to be confined to the boundary layer due to the depletion of the solvent and rejection of solute at the surface of the membrane.

In the boundary layer, the solute flux through the membrane is given by the permeate flux (J) and solute concentration (C_{ip}). With necessary assumptions

under steady state conditions, the net flux of solute at any point in the boundary layer is equal to the difference between flux by convection towards the membrane and the salt flux away from the membrane surface by diffusion. The diffusive flux away from the membrane surface is described by Fick's first law of diffusion as: $D_i \frac{dC_{iBL}}{dY}$, where D_i is the diffusion coefficient of the solute and Y is the coordinate perpendicular to the membrane surface.

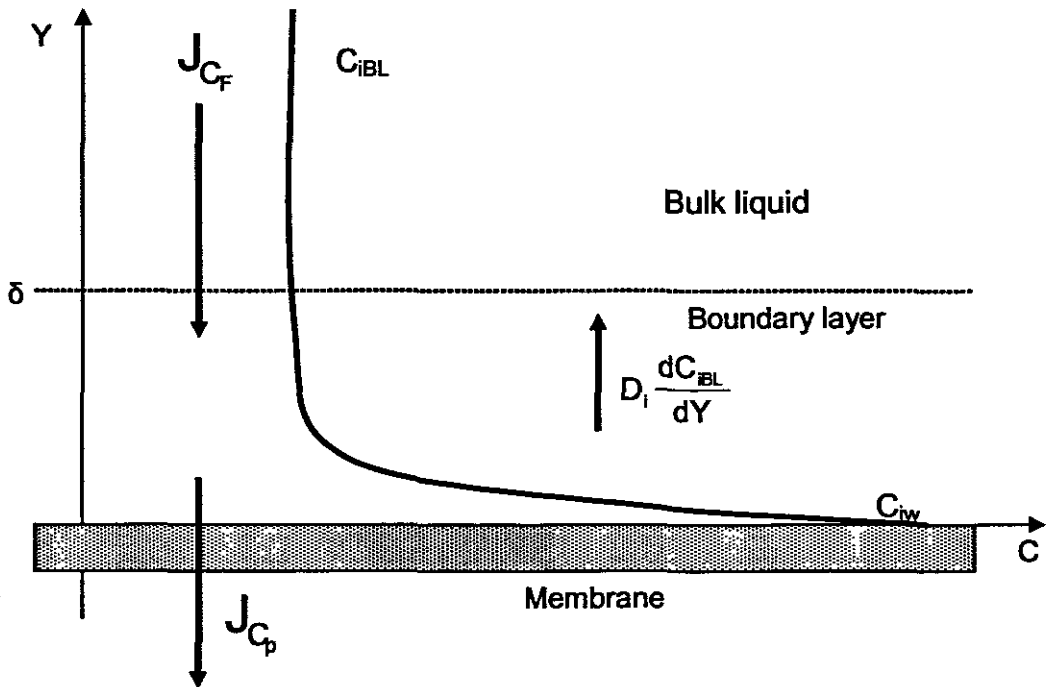


Figure 2.4: Illustration of the concept of the boundary layer and concentration polarisation at a membrane surface (Baker, 2004).

When a mass balance is performed around the boundary layer film (Figure 2.4), the solute transport is described by the boundary layer film model (Baker, 2004):

$$J_{C_f} - D_i \frac{dC_{iBL}}{dY} = J_{C_p} \quad (2.13)$$

The mass balance equation integrated over the thickness of the boundary layer (δ) yields:

$$J = k_s \ln \left(\frac{C_{iw} - C_{ip}}{C_{iBL} - C_{ip}} \right) \quad (2.14)$$

where: $k_s = D_i / \delta$

Equation (2.14) can be simplified to express flux due to gel polarisation effects on the membrane surface. The assumption made is that there is 100% rejection. When a gel layer with material i , of concentration C_{iG} , is present at the surface, then flux is given as:

$$J = k_s \ln \left(\frac{C_{iG}}{C_{iBL}} \right) \quad (2.15)$$

2.4.3 Pore blocking

There are various ways by which the membrane pores are blocked by fouling. Jacobs *et al.* (2000) presented a diagrammatic model to describe how the pores of the membrane are blocked during fouling. These pore blocking mechanisms are illustrated in Figure 2.5.

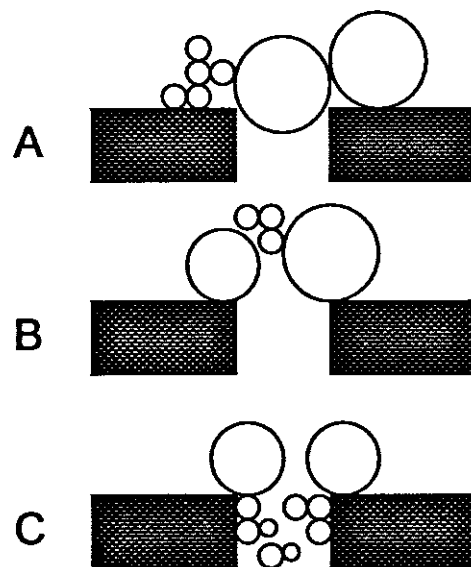


Figure 2.5: Schematic presentation of the pore blocking mechanism suggested by Jacobs *et al.* (2000). A - Complete pore blocking, B - Pore bridging, C - Internal pore blinding.

In the schematic A, the entrance to the pore is sealed by a particle with a diameter equal to or larger than the membrane pore. In schematic B, the diameter of the pore is reduced because of the partial obstruction of the entrance by the particles. The entrapment/adsorption of non-retained material occurs on the inside walls of the pores. The diameters of the material are smaller than the diameter of the pores. In schematic C, the smaller particles are lodged inside the membrane pores and often bridge against the walls. This mechanism is also called plugging.

2.5 FOULING MITIGATION

In the membrane industry, there are many methods that have been used to try to achieve meaningful control of membrane fouling. These include fouling prediction; *in situ* fouling monitoring; offline fouling studies; process optimisation; preventative measures; fouling removal techniques. Prediction methods can include fundamental mathematical models such as the resistance-in-series and concentration polarisation models or more complicated mathematical models that can often be difficult to comprehend or solve (Baker, 2004; Mulder, 1991). Destructive autopsy procedures, whereby the surface of a fouled membrane is thoroughly examined, are also used during the analysis of fouled membranes (Dudley & Darton, 1996). Methods for *in situ* monitoring and/or measurement of fouling are also useful in helping to determine the extent of membrane fouling during operation (Chen *et al.*, 2004). Preventative methods used include pre-treatment methods and removal of foulants by physical, chemical and biological means.

2.5.1 Fouling indices

Fouling indices are a combination of empirical and mathematical methods predicting the extent to which a specific effluent can foul a membrane. Two well known fouling indices are the silt-density index (SDI) and the modified fouling index (MFI) (Koen, 2000; Mairal, 1998; Mulder, 1991). SDI values greater than 3 indicate a significant fouling potential for RO membranes (Mairal, 1998).

To determine the MFI of particular feed water, a filtration test is carried out for 20 minutes at a constant differential pressure of 210 kPa at 20 °C. A cumulative filtrate volume is collected at every 30-second interval. At the end of the test, the ratio of the time elapsed (in seconds) to the cumulative filtrate volume is plotted as the function of cumulative filtrate volume. The MFI is given by the linear part of the plot.

Another form of modified fouling and plugging index has been recently proposed (Sanderson *et al.*, 2002 & 2004). This prediction method is based on ultrasonic measurement (Li, 2002 & Li *et al.*, 2002a, 2002b, 2002c, 2002d, 2002e, 2003 & 2005). Water, of which the fouling potential is to be determined, is fed through an ultrasonic measurement instrument that contains a flat-sheet membrane cell. The concept involves determining the fouling index of the water from the ultrasonic testing of the fouling formed on the membrane. This instrument is called a Fouling/Plugging Index Meter (UFPIM). It is currently in the early stages of development by the Department of Chemistry and Polymer Science, University of Stellenbosch and IfU GmbH (Germany). Functioning of the UFPIM is summarised in Appendix 1.

2.5.2 Analysis of fouled membranes

Fouled membranes often need to be analysed to determine the extent to which they have fouled. In industry, a scientific procedure called membrane autopsy is used; a membrane module is cut open and a scientific investigation is performed on the membrane (Dudley & Darton, 1995). This technique is usually case specific, and includes surface characterisation and elemental analysis of the fouled membranes. Characterisation methods include: scanning electron microscopy (SEM), scanning probe microscopy (SPM), electron dispersive spectroscopy (EDS), X-ray photoelectron spectroscopy (XPS) and X-ray diffraction (XRD) (Dudley & Darton, 1995).

2.5.3 Process monitoring of membrane fouling

Understanding the dynamics of fouling formation and cake layer deposition requires *in situ* measurement methods that are able to produce reliable real-time data. However, numerous techniques for investigating membrane fouling in real-time have been tried and most seem unsuccessful or insufficient for this purpose. Most of these techniques have been reviewed by Chen *et al.* (2004), and are summarised here in Table 2.2.

The ultrasonic method of fouling investigation has been effectively applied to detect fouling in flat-sheet and tubular membranes. However the signals obtained during tests performed in spiral wound and capillary modules were more difficult to interpret (Koen, 2000; Li, 2002). The main advantage that the ultrasonic technique has over other fouling detection methods is that it has a potential of economic viability (Chen *et al.*, 2004).

Table 2.1: Techniques for *in situ* investigation of membrane fouling and concentration polarisation (Chen *et al.*, 2004; Li, 2002)

Technique	Method	Limitations
Light deflection techniques	Shadowgraphy Refractometry Photo-interrupt sensor	Growth of fouling layer thickness
Magnetic resonance imaging	Nuclear magnetic resonance (NMR)	Expensive and not viable for industrial applications
Radioisotope techniques	Micro-array of semiconductor	Small range of flow conditions; No information for fouling <20 um
Electron beam techniques	Electron diode microscope (EDAM) Electron paramagnetic response (EPR) spectroscopy	Radioactive or spin-labelling of the foulants required
Optical and photography techniques	Direct observation through membrane (DOTM) Direct observation above membrane	Further development of cake and fouling layers; Transparent membrane and module required.
Laser techniques	Interferometry Triangulometry Optical laser sensor method	Requires steady state; No correlation with flux data
Electrical conductivity	Electrical conductivity	Interference in water system
Ultrasonic technique	Ultrasonic time domain reflectometry (UTDR)	Signal complexity in spiral wound and capillary membranes

2.5.4 Prevention and removal

Pre-treatment of feed water prior to membrane filtration is one of the common ways of preventing or minimising fouling in membranes. Pre-treatment methods include chemical remedies, pre-filtration and adsorption of potential foulants by activated carbon. As a pre-treatment procedure, certain chemicals are added to feed water so as to change its chemical properties. For example, a pH change can be used to coagulate and settle potentially fouling matter in the water. MF and/or UF can be used as prefiltration for NF and RO membranes. Adsorption by granular activated carbon (GAC) and powdered activated carbon (PAC) is also a preferred method of pre-treating effluents before they are fed to membrane systems (Shon *et al.*, 2004; Tsujimoto *et al.*, 1998).

Membrane fouling can be minimised by cleaning of membranes by chemical, physical or biological means, to remove the cake layers and to dislodge foulants from the surface and the pores of the membranes. Typical cleaning agents include alkalis, peroxides, acids and hypochlorides.

Physical cleaning of membranes is achieved by the use of a wide range of techniques, such as utilisation of sponge balls, air scouring, ultrasonic cleaning, water jets and hydraulic pressure (backflushing, backwashing, backpulsing), to mechanically remove or dislodge particles or fouling cake layer from the membrane surfaces (Cakl *et al.*, 2000; Chai *et al.*, 1999; Kennedy *et al.*, 1998; Li & Li *et al.*, 2002).

Enzymatic cleaning is one of the effective biological tools used on membranes fouled by foulants such as whey proteins and abattoir effluent (Argüello *et al.*, 2003; Maartens, 1998).

There are many other examples of techniques employed in order to counteract membrane fouling; for example, membranes can be pre-coated with surfactant to reduce adsorption of NOM and aromatic substances onto the membranes (Maartens, 1998).

Modification of module designs and optimisation of process variables are also other strategies used to mitigate the fouling problem. For example, promotion of turbulence and vortices by increasing cross-flow-rates, use of channel spacers and modification of hydraulic geometries (e.g. channel heights) are used to induce shear (Hoek *et al.*, 2002).

Cross-flow velocity and operation pressures below critical fluxes are further process variables that can be monitored and controlled to minimise the effect of membrane fouling and concentration polarisation (Bian *et al.*, 2000).

2.6 CHARACTERISATION OF MEMBRANE FOULING BY MICROSCOPY

Microscopy techniques are available methods used to analyse structural characteristics of membranes and membrane fouling. The most popular microscopy techniques for this purpose are the scanning electron microscopy (SEM) and the atomic force microscopy (AFM).

2.6.1 Scanning electron microscopy (SEM)

SEM has been widely used in membrane and membrane fouling studies for obtaining direct surface analysis of membrane. Distinctions between the pores and the surface fouling can be made using SEM. The major advantage of SEM is that it has a very high imaging resolution (Scott, 1996). A thin conductive layer is applied on the surface to be imaged to make it conductive. However, covering of membrane surface can result in modification of pore dimensions and roughness, thus, leading to errors in topographic images. A thin gold coating can be used to minimise relative errors. Gold coating was found to be adequate for MF membranes as they have larger pores and not too rough surfaces.

2.6.2 Atomic force microscopy (AFM)

AFM is a microscopic technique that relies on a tip of a probe to measure the properties of a sample, such as the surface topography and surface roughness. AFM has the capability of measuring both wet and dry samples.

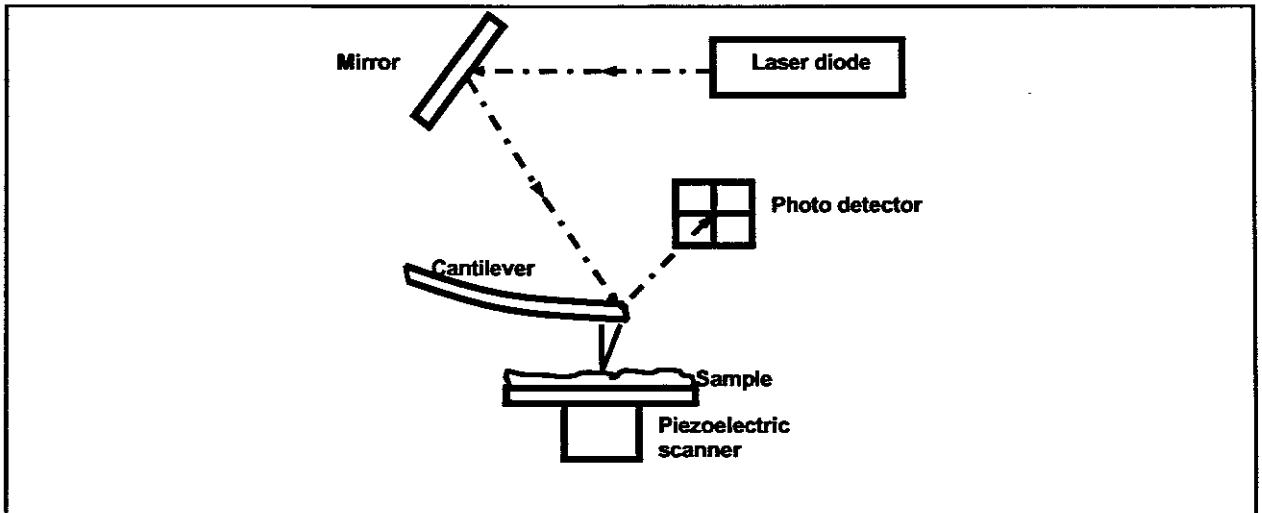


Figure 2.6: Principle of AFM measurements.

It is important that the probe does not change or damage the sample topography. It is possible that softer samples e.g. polymers may be damaged through scratching. One of the requisites that should be considered when probes are selected is that it should be soft enough (with low spring constants) not to damage the sample surface (especially for soft materials such as polymers). The force acting on the cantilever is described by:

$$F = \zeta \Delta h \quad (2.16)$$

where ζ is the spring constant and h is the vertical deflection.

CHAPTER 3

MEASUREMENT OF MEMBRANE FOULING BY ULTRASONIC METHOD: LITERATURE REVIEW

3.1 INTRODUCTION

There are numerous methods and strategies for mitigation of membrane fouling that have been studied and used in an effort to control the problem. Information about the progression of membrane fouling is a very important aspect in finding means of membrane fouling alleviation. The ultrasonic technique has the capability to provide real-time measurements during investigation of membrane fouling.

In the late 1990's the ultrasonic technique demonstrated its capability as a non-invasive and real-time measurement technique for the investigation of membrane fouling (Mairal *et al.*, 1999; Mairal *et al.*, 2000; Peterson *et al.*, 1998).. The technique was studied further and successfully applied to monitor membrane compaction and membrane fouling thickness in real-time. (Koen, 2000; Li, 2002 & Li *et al.*, 2002a, 2002b, 2002c, 2002d, 2002e, 2003 & 2005; Reinsch *et al.*, 2000).

Peterson *et al.* (1998) first showed that ultrasonic-time-domain-reflectometry (UTDR) could be used for the real-time measurement of membrane thickness and compaction during high-pressure operation. Mairal *et al.* (1999) then described the first systematic attempt to adapt and employ UTDR for the non-invasive measurement of RO membrane fouling and cleaning in real-time. Results showed that the amplitude of the ultrasonic signal reflected from the membrane changed as fouling developed on the membrane surface and proved the suitability of UTDR for the real-time monitoring of membrane fouling. Further progress has since been made in the use of the non-invasive ultrasonic technique in investigating fouling in membrane systems (Koen, 2000; Li, 2002;

& Li *et al.*, 2002a, 2002b, 2002c, 2002d, 2002e, 2003 & 2005; Mairal *et al.*, 2000).

Koen (2000) investigated the use of UTDR in the fouling and cleaning of flat-sheet RO membranes. Results showed that an ultrasonic echo formed in the waveform as fouling started on the membrane surface and it disappeared as cleaning progressed.

Li (2000) and co-workers (Li *et al.*, 2002a, 2002b, 2002c, 2002d, 2002e, 2003 & 2005) used UTDR for monitoring membrane cleaning and evaluating cleaning methods in membrane filtration. It was found out that the UTDR technique could provide a means of producing a differential signal (an echo signal from a fouling layer) by comparing the difference between the reference and test waveform. A predictive modelling program, ultrasonic reflection modelling (URM), was developed, to understand deposition of fouling layers on membrane surfaces.

It is apparent that the ultrasonic measurement technique is currently among the techniques at the forefront of *in situ* monitoring of membrane fouling in laboratory and industrial applications.

3.2 BASIC ULTRASONIC PRINCIPLES

The ultrasonic measurement is based on the principle of sound travelling by vibrations of atoms and molecules present in a material. The sound travels with a velocity depending on the mechanical properties of the material. Discontinuities and boundaries cause sound waves to be scattered or reflected, resulting in echoes and reverberations of the sound wave (Cartz, 1995 & McIntire, 1991).

3.2.1 Types of waves

When an ultrasonic wave is being propagated in a material it can be of several forms. Each type results in a certain motion of particles (atoms and molecules) of a material in response to the wave. In ultrasonic testing the most commonly used forms are either longitudinal or shear waves. Surface waves and lamb waves are other forms of sound propagation that exist (McIntire, 1991)

The types of waves and their typical characteristics are shown in Table 3.1.

Table 3.1: Types of waves propagated in a material

Wave type	Direction of propagation	Characteristic velocity
Longitudinal (compression) waves	same direction or parallel to the direction of wave propagation	short wavelengths and high velocities
Shear waves	particle motion is perpendicular to the direction of wave propagation	velocity approximately half of that of longitudinal waves.
Surface or Rayleigh waves	elliptical particle motion, and can be propagated on the surface of the material	velocity is about 90% of the velocity of shear waves of a material
Lamb or plate waves	complex vibratory movements	complex velocities in the direction of the vibratory movements

3.2.2. Ultrasound and ultrasonic waves

Ultrasound refers to the sound generated beyond the human hearing range, which is typically 20 kHz. Figure 3.1 shows the three ranges of frequencies of the acoustic spectrum. The frequency below the hearing range is called infrasound. The sound waves of this nature are characterised by large wavelengths.

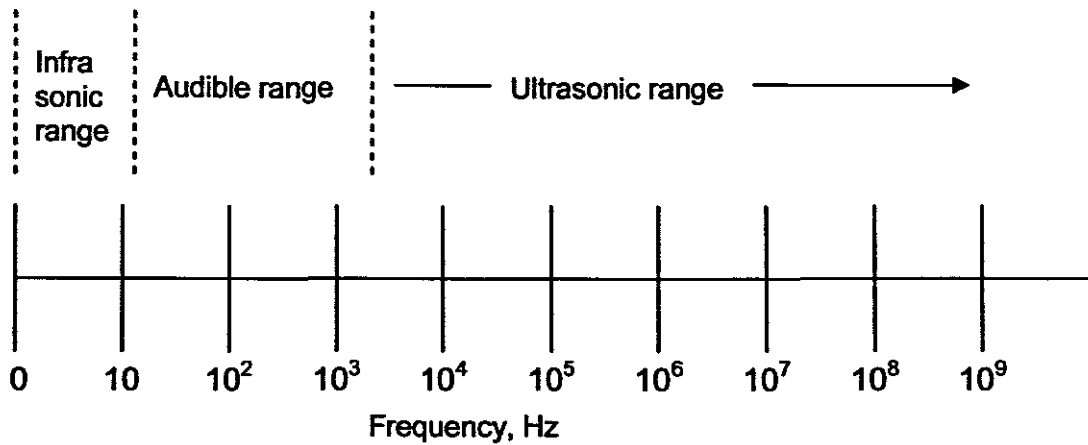


Figure 3.1: Three frequency ranges of the acoustic spectrum.

In ultrasonic non-destructive testing, frequencies between 1 MHz and 25 MHz are used. In other applications, frequencies as low as 25 kHz and as high as 100 GHz are used (McIntire, 1991).

3.2.3 Reflection and transmission of waves

Sound travelling in a material under the influence of a sound pressure will result in the displacement of the particles of that material. The material will resist the change in displacement by virtue of its elastic property. This elastic property of a material is called its specific acoustic impedance. The specific acoustic impedance of a material (z) is equal to the product of the density of that material (ρ) and the velocity of a sound wave, through that material (c):

$$z = \rho c \quad (3.1)$$

The behaviour of sound waves through a material is characterised by z . A wave can travel through a material because its molecules or atoms are elastically bound to one another and oscillate when an excess pressure is exerted on the material. The expression for the oscillations, of the molecules, atoms, or clusters of atoms or molecules that lead to a travelling wave, is given by either of the following two equations (McIntire, 1991):

$$W = W_0 \sin 2\pi \left(\frac{t}{\tau} - \frac{x}{\lambda} \right) \quad (3.2)$$

$$W = W_0 \sin(\omega t - ux) \quad (3.3)$$

where W_0 is the maximum amplitude of excess pressure, t is the propagation time, λ is the wavelength, $u = 2\pi/\lambda$ is the propagation constant (or wave number), $\omega = 2\pi/\tau$ is the rotational frequency (in radians per second) and τ is a wave period (cycles per second). The amplitude variation of pressure at a distance x and time t for a travelling wave can also be given by equation (3.4), where $f = 1/\tau$ is the frequency of the waves in cycles per second (Hz).

$$W = W_0 \sin 2\pi \left(ft - \frac{x}{\lambda} \right) \quad (3.4)$$

The wave is a function of x and t variables. The wave is generally described in terms of its frequency f and wavelength λ , where the velocity of the wave is expressed as:

$$c = \lambda f = \lambda \tau \quad (3.5)$$

The energy transmitted by a sound wave is expressed as (Cartz, 1995):

$$E = \frac{P_s^2}{2\rho c} \quad (3.6)$$

where P_s is the sound pressure (excess above the atmospheric pressure) that causes propagation of the sound wave. The sound pressure results in particles to be displaced with a velocity, Q .

Figure 3.2 shows a case where a wave (i) of normal incidence to the boundary of medium I (with a specific acoustic impedance, z_1) is propagated across to medium II (with a specific acoustic impedance, z_2). Upon striking of the boundary by the incident wave, i , resulting a reflected wave, r , and transmitted wave, t , there are conditions that must be satisfied.

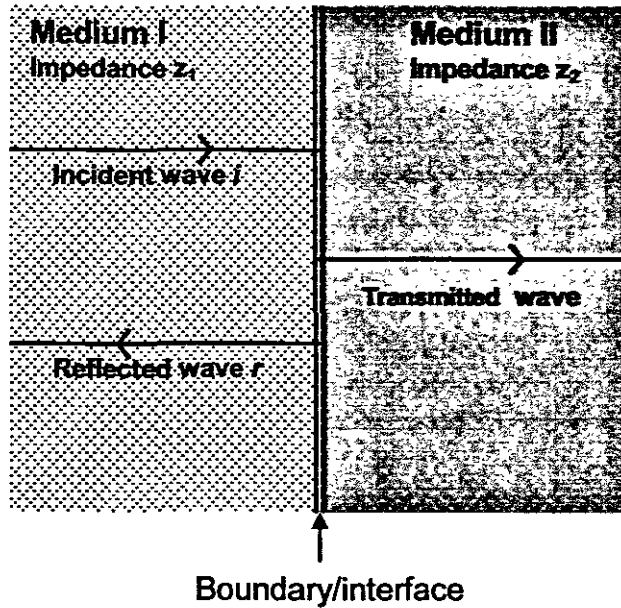


Figure 3.2: Reflection and transmission of a sound wave at a normal incidence on a boundary between two media of specific acoustic impedance, z_1 and z_2 (Cartz, 1995).

The first condition of continuity is that the particle velocity is continuous across the boundary,

$$Q_i + Q_r = Q_t \quad (3.7)$$

where Q_i , Q_r and Q_t are particle velocities at the boundary of the incident, reflected and transmitted waves.

The other condition of continuity (based on the fundamental law of continuum of pressure in a fluid) is that the sound pressures on the two sides of the boundary are equal (Cartz, 1995):

$$P_i + P_r = P_t \quad (3.8)$$

where P_i and P_r are the incident and reflected pressure components of the sound pressure at a point in medium I and P_t is a sound pressure at a point in medium II.

At the boundary of the two materials the energy is divided such that there is reflected energy and transmitted energy. The fraction of reflected energy, G_E , is represented as:

$$G_E = \frac{z_2 - z_1}{z_2 + z_1}^2 \quad (3.9)$$

The fraction of the transmitted energy is such that the sum of the fractions of the reflected and transmitted energies is equal to 1. Then it follows that the fraction of the transmitted energy, T_E , equals to $1 - G_E$ (Cartz, 1995):

$$T_E = 1 - G_E = \frac{4z_1z_2}{(z_1 + z_2)^2} \quad (3.10)$$

If a wave incidents a surface obliquely at an angle α_1 (less than the first critical angle), then the fraction of the reflected energy is given by (Cartz, 1995):

$$G_E = \frac{z_2 \cos \alpha_1 - z_1 \cos \alpha_2}{z_2 \cos \alpha_1 + z_1 \cos \alpha_2}^2 \quad (3.11)$$

The fraction of the transmitted energy is given by:

$$T_E = \frac{4z_2z_1 \cos \alpha_1 \cos \alpha_2}{z_2 \cos \alpha_1 + z_1 \cos \alpha_2}^2 \quad (3.12)$$

Table 3.2: Typical values of the percentage of ultrasonic energy reflected at a perfect boundary of normal incidence (Cartz, 1995)

1 st Medium	Impedance (z) kgm ⁻² s ⁻¹ x 10 ⁶	2 nd Medium												
		Steel	Nickel	Copper	Brass	Lead	Mercury	Glass	Quartz	Polystyrene	Bakelite	Water	Oil (transformer)	Air
Aluminium	17	21	24	18	13	3	0.7	2	0.4	49	38	70	74	100
Steel	46		0.2	0.1	1	10	16	31	26	77	71	88	89	100
Nickel	50			0.8	3	12	18	34	29	79	73	89	89	100
Copper	42				0.6	7	13	28	22	75	68	87	88	100
Brass	36					4	8	22	17	72	64	85	86	100
Lead	24						0.8	9	5	60	51	78	79	100
Mercury	20							4	2	55	44	74	76	100
Glass	13								0.5	39	28	63	65	100
Quartz	15									44	34	67	69	100
Polystyrene	3										2	11	13	100
Bakelite	4											21	23	100
Water	1.5												0.1	100
Oil	1.4													100
Air	4 x 10 ² kgm ⁻² s ⁻¹													100

At all the air-solid interfaces, 100% energy is reflected. The impedance of air is in units of 10² kgm⁻²s⁻¹ while those of liquids and solids are in units of 10⁶ kgm⁻²s⁻¹.

In ultrasonic NDT, waves reflected at interfaces or discontinuities are detected and analysed. The principle of detection of interface or discontinuity echoes between the water-membrane interface is used in the ultrasonic measurement of membrane fouling (Koen, 2000; Li, 2002; & Li *et al.*, 2002a, 2002b, 2002c, 2002d, 2002e, 2003 & 2005; Mairal *et al.*, 2000).

3.3 ULTRASONIC EQUIPMENT

A typical ultrasonic test instrument provides basic functions that include the generation of elastic waves, reception of ultrasonic waves, signal conditioning and processing. Ultrasonic equipment can differ in functionality, depending on the intended application, and may incorporate functions including multi-channel capability, additional signal gates, filters, computer interfaces and methods that compensate for signal loss as a function of distance traveled and attenuation (McIntire, 1991). Some ultrasonic instruments used in pulse-echo operation are portable and modular instruments, others are general purpose test equipment and others are laboratory test instruments. In pulse-echo operation, the instrument sends ultrasonic signals to a test material and detects signals reflected from the test material.

3.3.1 Ultrasonic equipment for used for research

The design of instruments used in ultrasonic testing research, such as those used in this study, are designed such that they can be used with other high performance instrumentation in the laboratory environment such as oscilloscopes and data-logging computers. High-speed computer interfaces are usually incorporated in designs, for fast data logging. A typical set-up for pulse-echo-operation is illustrated in Figure 3.3.

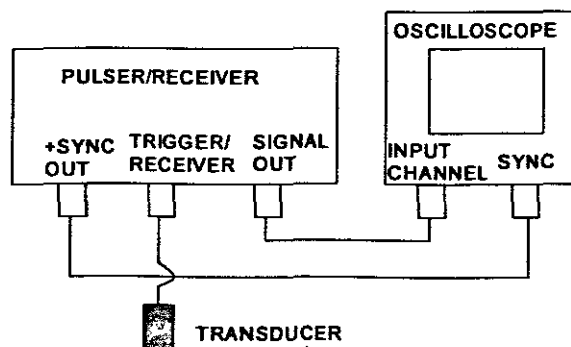


Figure 3.3: Schematic representation of pulser/receiver-oscilloscope connection for pulse-echo operation (Li, 2002).

A pulser/receiver is used to generate the voltage signal that triggers the transducer to send out ultrasonic waves. The transducer then picks up the reflected waves and transmits them as a voltage signal back to the pulser/receiver. The oscilloscope captures and displays data received from the pulser/receiver. This data is displayed as amplitude changes and can be displayed and stored on a computer.

3.3.2 Ultrasonic transducers

The ultrasonic transducers convert electrical energy into vibrational energy or vibrational energy to electrical energy. The vibrational energy is the mechanical energy in the form of sound.

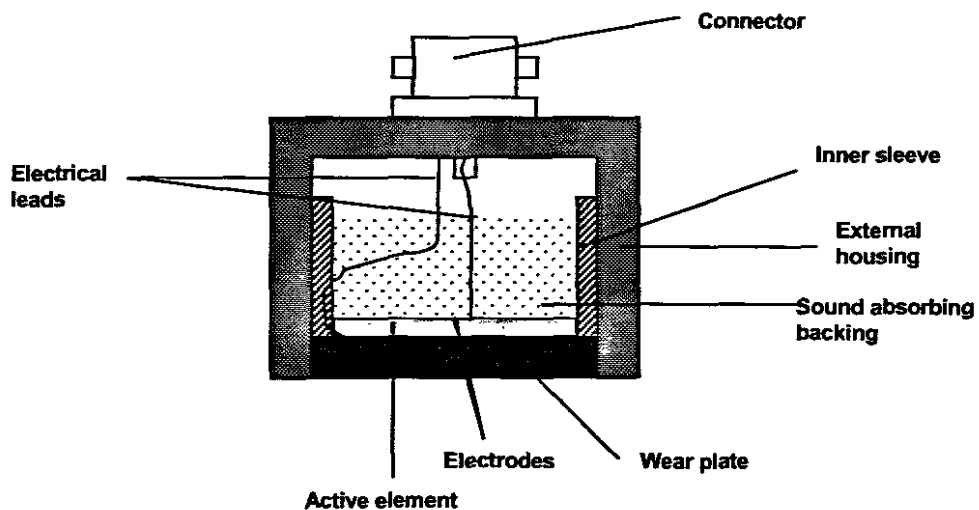


Figure 3.4: Cutaway view showing internal components of an ultrasonic transducer

The functional components of an ultrasonic transducer are shown in Figure 3.4. The active element is usually made of a ferroelectric or piezoelectric material such as lead zirconate titanate (PZT), quartz and polyvinylidene fluoride (PVDF). Piezoelectric materials are able to transform the excitation electrical pulse to ultrasonic energy and vice versa. The electrical leads are connected to the active element via the electrodes at the two faces of the active element. A high

attenuation, high density material is used to absorb sound from the back face of the active element. The transducer element is protected, by a wear plate, from the testing conditions such as abrasion and wear.

There is a wide range of piezoelectric transducers available in the field of ultrasonic NDT. These transducers differ in their design and functionality. Functional characteristics of the transducer types available are shown in Table 3.3.

Table 3.3 : Functional characteristics of available transducer types

Type	Characteristics
Dual element transducers	Utilise separate transmitting and receiving elements
Delay line transducers	Single element longitudinal wave transducer used in conjunction
Immersion transducers	Available in unfocused (flat), spherically (spot) focused and cylindrically (line) focused
Angle beam transducers	Uses the principles of refraction and mode conversion to produce refracted shear or longitudinal waves in a test material
Normal incidence shear wave transducers	Incorporate a shear wave crystal. These transducers are used for velocity measurements and were the type used in this study.

3.3.3 Transducer sound field

The waves transmitted by a transducer follow a pattern that is referred to as the sound field. The sound field of a transducer is divided into two zones, the near field and the far field (Cartz, 1995). These are illustrated in Figure 3.5.

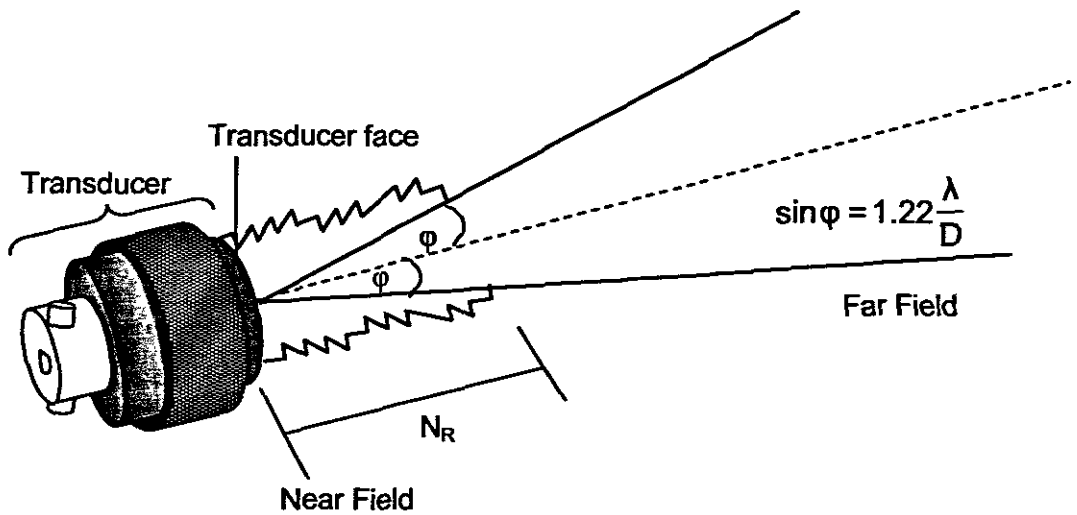


Figure 3.5: Illustration of near field and far field zones in a transducer beam.

Near field intensity fluctuations (represented by the zigzag lines) extend out to the distance N_R , beyond which the beam is more uniform (in the far field zone). The impedance of the active element can be described by equation (3.13) (Cartz, 1995).

$$Z_T = \frac{D^2 - \lambda^2}{4\lambda} \quad (3.13)$$

where D is the diameter of the transducer active element. Because D is much bigger than λ , the second term of the numerator in equation (3.13) can be neglected to obtain an equation that describes the distance of the near field, N_R :

$$N_R = \frac{D^2}{4\lambda} \quad (3.14)$$

The angular spread of the far field is described by:

$$\sin \phi = 1.22 \frac{\lambda}{D} \quad (3.15)$$

where ϕ is the incident angle of the transducer beam.

3.3.4 Theoretical resolution of transducers

The theoretical resolution of a specific frequency transducer can be calculated if the speed of the sound wave in the medium that is under investigation is known. The wavelength can be calculated from equation (3.16) (Cartz, 1995):

$$c = \lambda f \quad (3.16)$$

where λ is the wavelength, c is the speed of sound wave (m/s) and f is the transducer frequency. The smallest detail that the transducer will pick up is 0.25 of the sound wave's wavelength. The theoretical resolution can thus be calculated with equation (3.17) (Li, 2002):

$$\text{Resolution} = 0.25 \lambda \quad (3.17)$$

3.4 APPLICATION OF ULTRASONICS IN MEMBRANE FOULING STUDIES

Figure 3.7 illustrates the cross-sectional view of a typical single-membrane flat-sheet module, similar to that used by Li *et al.* (2002). During ultrasonic testing of membrane fouling, a transducer was coupled with an ultrasonic gel on the top plate of the module. Permeate was withdrawn from the bottom side of the module. The arrowed lines (A to F) illustrate how the waves normal to the module travel through the module. Some of energy propagated by the transducer into the module (A) is reflected at various interfaces in the module (B to F) back to the transducer while some energy will be transmitted through the bottom perspex plate. A corresponding ultrasonic signal is shown in Figure 3.7.

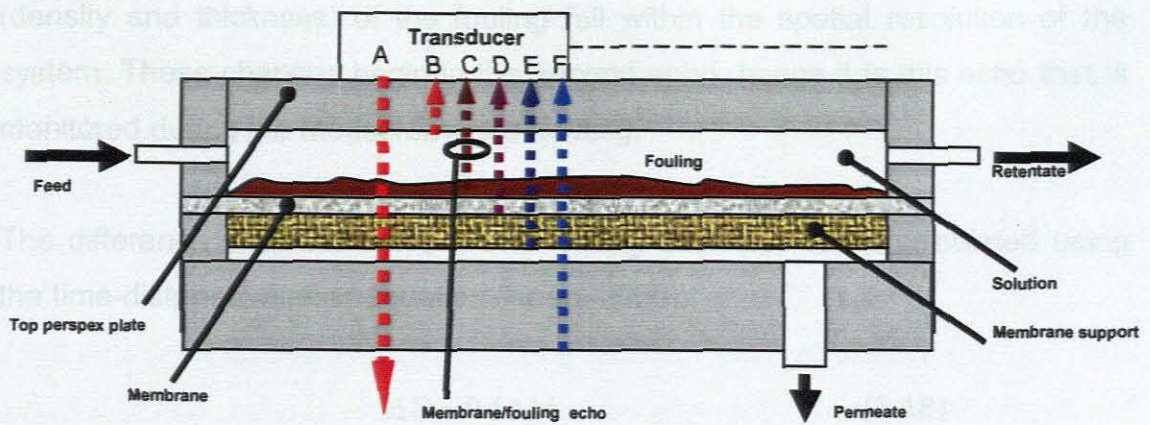


Figure 3.6: Illustration of the principle of multiple wave reflections during ultrasonic measurement of fouling on a flat-sheet test module.

It should be noted that the monitored incident and reflected acoustic waves are longitudinal waves and travel on the same path. The lines labelled A to F, shown in Figure 3.6 are for illustration purposes.

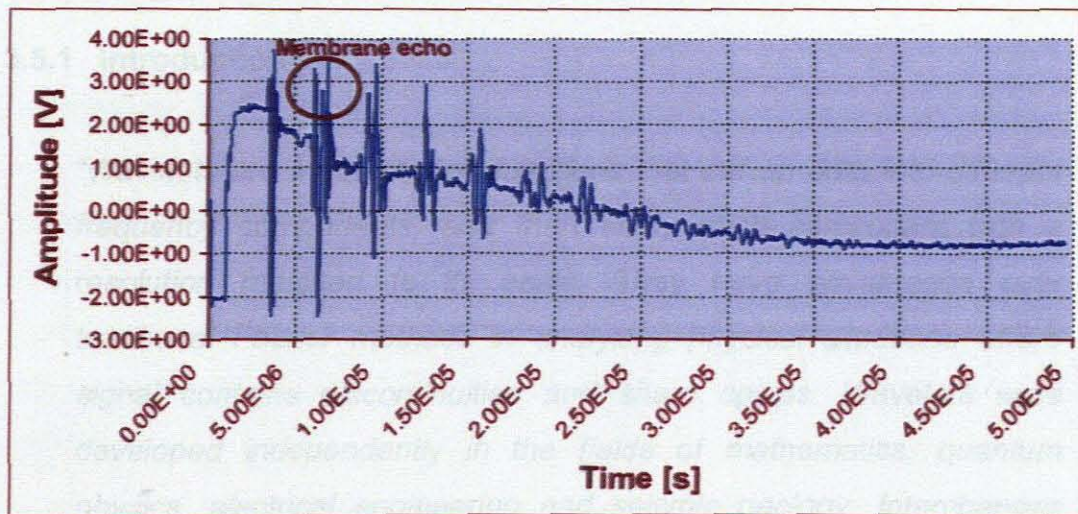


Figure 3.7: Ultrasonic time-domain response signal for the set-up in Figure 3.6.

Each set of echoes except the first echo contains energy from a preceding echo. After $50 \mu\text{s}$, the decaying energy falls below the resolution of the system. The second echo is of prime interest as it comes from the interface between the solution and the membrane. When fouling occurs, the properties of the membrane may change due to foulants accumulating inside the pores and on the surface of the membrane. A new echo will form when the properties

(density and thickness) of the fouling fall within the spatial resolution of the system. These changes begin in the second echo, hence it is this echo that is monitored during the measurement of fouling.

The difference in arrival times allows fouling thickness to be calculated using the time-distance relation equation (Koen, 2000):

$$\Delta S = 0.5c\Delta t \quad (3.18)$$

where ΔS is the change in fouling thickness, c is the sound velocity in the fouling material and Δt is the change in arrival time of the fouling peak.

3.5 WAVELET ANALYSIS AND INTERPRETATION OF ULTRASONIC SIGNALS

3.5.1 Introduction

“Wavelets are mathematical functions that cut up data into different frequency components, and then study each component with a resolution matched to its scale. They have advantages over traditional Fourier methods in analyzing physical situations where signal contains discontinuities and sharp spikes. Wavelets were developed independently in the fields of mathematics, quantum physics, electrical engineering and seismic geology. Interchanges between these fields during the last ten years have led to many new wavelet applications...”

Amara Graps (Graps, 1995)

Wavelet theory has inspired the development of a powerful signal processing methodology and wavelets are continually finding applications across the different disciplines of engineering and science. This methodology includes wavelet transformation and time-frequency representation with wavelet software (Bruce & Gao, 1996). Many wavelet researchers (e.g. in the fields of physics, mathematics and electrical engineering) tend to focus on derivation of theorems and mathematical equations and creation of algorithms or 'code books'. In this study, it was practical to use existing mathematical methods for performing transforms of the ultrasonic signals. The wavelets work in this study seeks to advance the ultrasonic technique used in membrane fouling studies. However, it was essential create a sound understanding of the basic wavelet theory from an application standpoint so as avoid using wavelet software as a 'black box'. Therefore, in this literature review proof of mathematical theorems and equation derivations are not given.

3.5.2 Time-frequency representation of signals

In ultrasonic NDT, signals obtained during measurement are of transient nature and the standard instrumentation represents these signals in the time-amplitude domain. Most of the energy of these signals is often concentrated in a given frequency interval. In some cases it becomes necessary to view the information contained in the frequency component of the signal as it might contain valuable information that is not available in time-amplitude domain (Angrisain & Daponte, 1997).

Use of time-frequency representations for signal analysis is widespread. Time-frequency representations of signals include Fourier transforms and wavelet transforms. The simplified explanation of these representations is that they use scale-varying basis functions for relating to a signal. The scale-varying basis functions are mathematical functions that can be used to cut up data using different scale sizes. An example given by Graps (1995) to explain scale-varying basis functions is that of the signal in the domain of between 0 and 1 that can be divided with step functions that range from 0 to 0.5 and 0.5 to 1.

The original could be divided four step functions from 0 to 0.25, 0.25 to 0.5 and 0.5 to 0.75 and 0.75 to 1. Now each set of the representation code the original signal with a particular scale.

3.5.3 Fourier transforms

The classical Fourier transform theory was established by Joseph Fourier in the 1800's and is omnipresent in analysis and treatment of signals (Graps, 1995). The Fourier transform can be used to analyse the frequency content of the signal in time domain. The transformed signal is expressed as a linear sum of sine and cosines. The inverse of a Fourier transform reconstructs the original signal in time-amplitude domain and for this reason, it is termed reversible transform.

The well known FT's are the Discrete Fourier transform (DFT), windowed Fourier transform (WFT) and the Fast Fourier transform (FFT). The DFT estimates the Fourier transform of signal function from a finite number of its sampled points. The sampled points are supposed to represent how the signal looks at all other times. FFT is a DFT algorithm that can approximate Fourier. The WFT or short-time Fourier transform (STFT).

The major disadvantage associated with the Fourier transform is that it can only represent the signal in frequency amplitude domain. The transform is unable to show when in time (*position*) do the frequency components exist. The wavelet transforms and wavelet-based time frequency representations

3.5.4 Wavelet analysis

Wavelet analysis techniques have used in the interpretation of ultrasonic signals in a range of application fields. Examples that are more relevant to this study are where the use of wavelet analysis of ultrasonic signals during

measurement of thin multilayer structures (Angrisani & Daponte, 1997; Chona *et al.*, 2003).

Unlike Fourier transforms, wavelets have a variable resolution and are able to represent ultrasonic signals in both time and frequency domains. Wavelet analysis procedure involves adopting a model wavelet function, called the mother wavelet. Figure 3.8 shows some families of wavelets viz. Daubechies, Coiflet, Haar and Symmlet. Level of iteration and number of coefficient differentiate between the subcategories present with the wavelet families. Often the number of vanishing moments distinguishes the wavelet categories within a family (Graps, 1995). Vanishing moments are mathematical functions for wavelet coefficient that must be satisfied and are linked to the number of wavelet coefficients.

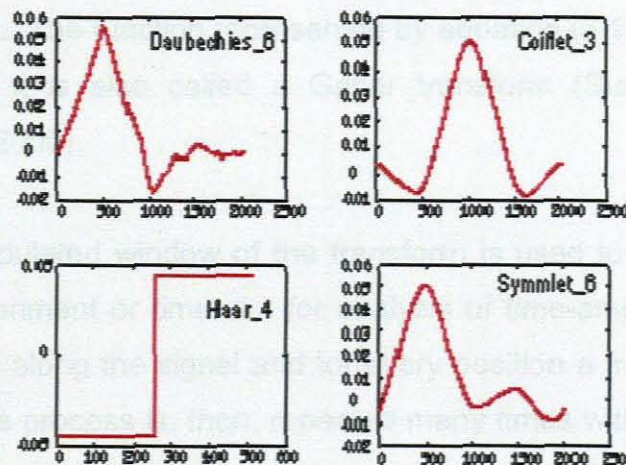


Figure 3.8: Some of different families of wavelets. These figures were created using WaveLab (Graps, 1995).

3.5.5 AGU-Vallen Wavelet software

The Gabor transformation of ultrasonic signals was achieved using wavelet software program, AGU-Vallen Wavelet, which was developed in collaboration between Vallen-Systeme GmbH (Munich, Germany) and Aoyama Gakuin University (AGU) (Tokyo, Japan). The principle of transformation is based on windowing of a signal function $s(t)$ by a window function $w(t)$ around the time ψ ,

or $w(t - \psi)$, utilising a short-time Fourier transform. The window function is shifted in time by changing ψ over the whole signal and consecutive overlapped transforms are performed. The frequency spectrum of the signal is presented as a function of time. A STFT of a signal function, $s(t)$ is defined as:

$$[STFT](\omega, \psi) = \int_{-\infty}^{\infty} s(t)w(t - \psi) \exp(-i2\pi\omega t) dt \quad (3.19)$$

where $s(t)$ is the signal to be analysed and $w(t - \psi)\exp(i2\pi\omega t)$ is a time-shifted and modulated version of window function $w(t)$ (Suzuki *et al.*, 1996). When the window function is Gaussian, $w(t)$ becomes:

$$w(t - \psi) = \exp \frac{[-(t - \psi)^2]}{\sigma^2} \quad (3.20)$$

where σ constant. The function represented by equation (3.19) has a Gaussian window function it is also called a Gabor transform (Suzuki *et al.*, 1996; Takemoto *et al.*, 2000).

The scalable modulated window of the transform is used to select the correct signal-time environment or time slot for analysis of time-amplitude signal. The window is shifted along the signal and for every position a frequency spectrum is calculated. This process is, then, repeated many times with a slightly shorter or longer window for every new cycle, resulting in windows that overlap to produce a complete coverage of the signal. Eventually, there is a group of time-frequency representations of the signal, with varying resolutions. The individual time-frequency representations contain data as a function of time, frequency and magnitude, which are then assembled to a three-dimensional graph or contour map on x, y and z coordinate system (Suzuki *et al.*, 1996; Takemoto *et al.*, 2000). The data can then be stored as transient files (*.tm). The sampling interval for the stored signals must satisfy the Nyquist Theorem, which states that the sampling rate or frequency must be greater than twice the highest frequency of the input signal (Roland-Mieszkowski & Young, 1991).

CHAPTER 4

EXPERIMENTAL: MATERIALS AND METHODS

4.1 INTRODUCTION

NOM is a major contributor to fouling during membrane filtration of NBW. NOM was characterised by organic carbon content as total organic carbon (TOC) and dissolved organic carbon (DOC) before membrane filtration of NBW. The organic carbon content of the NBW was used as the indicator of NOM concentration.

MF experiments were carried out on a two-part experimental unit. The first part was the MF system shown in Figure 4.1, for performing filtration experiments, and the second part was the ultrasonic measurement system, shown in Figures 4.3 and 4.4, for capturing ultrasonic data. The ultrasonic data were recorded and stored in electronic form and later retrieved for analysis and interpretation.

The experiments were performed in triplicate, under the same conditions, to ensure reproducibility of measurements. Membrane samples removed from the experiments were then prepared for microtome cuts and examined by SEM and AFM for observation of surface properties. AFM and the SEM were used for complementary purposes rather than for direct comparison.

4.2 EXPERIMENTAL EQUIPMENT

The experimental set-up was a two-part system made up of a MF system and an ultrasonic measurement system. These two systems were operated simultaneously, as one unit.

4.2.1 MF system

Figure 4.1 illustrates of the membrane filtration system used for the experiments. The system consisted of a de-ionised water feed tank, a NBW feed tank, a peristaltic feed pump, a flat-sheet filtration module, pressure gauges and a flow meter. The feed water was pumped from either the de-ionised water vessel or the NBW feed vessel. Flow was switched between the two vessels with a 3-way valve. This action was essential for conditioning and calibrating the system for the fouling experiments before ultrasonic measurements were made. TMP was controlled by adjusting the needle valve on the retentate line. The permeate flow-rate was measured with a balance and a timer.

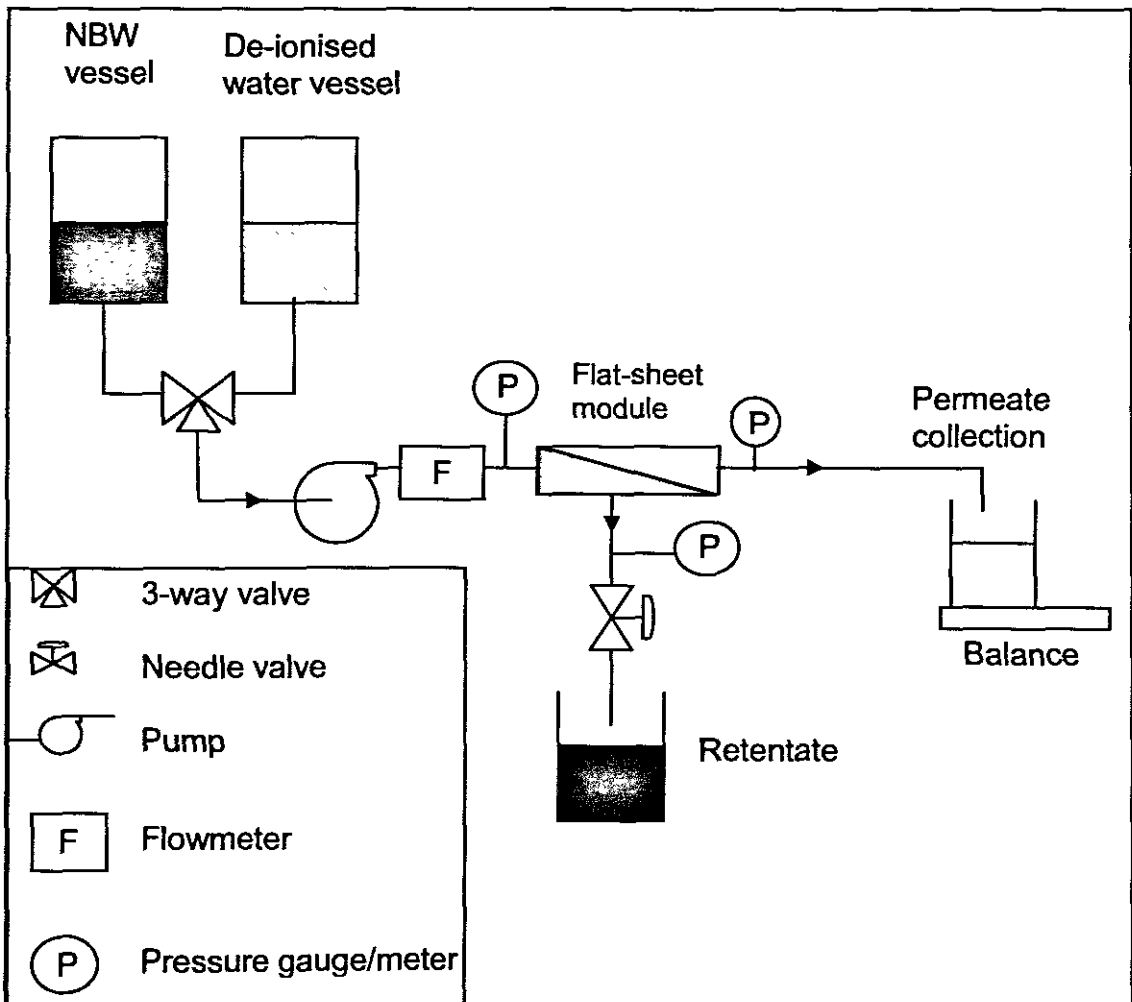


Figure 4.1: Schematic representation of the MF system.

The flat-sheet module (Figure 4.2) in the MF system was made up of two polymethyl methacrylate (perspex) plates that were assembled together. Perspex material was chosen because of its acoustic properties. It has been reported that the use of perspex is suitable in ultrasonic measurements because of its acoustic impedance, resulting in reduced attenuation in signals obtained during the measurement of membrane fouling (Li, 2002). Attenuation is the decrease in the intensity of the ultrasonic signal, which affects the accuracy or resolution of measurements.

Each perspex plate had a thickness of 19 mm, a width of 90 mm and length of 200 mm. The top plate had a cavity on the top side, 13 mm deep, 88 mm long and 30 mm wide. On the underside, the top plate had a groove that formed the filtration flow channel of the cell. The rectangular flow channel was 100 mm long, 32 mm wide and 3 mm high. Therefore the effective membrane area was 0.0032 m². The bottom plate had a rectangular groove, fitted with a flat sintered-brass membrane support of the same dimensions as the effective membrane area. To form an assembled module, the two perspex plates were fastened together with M6 bolts and sealed with a rubber o-ring.

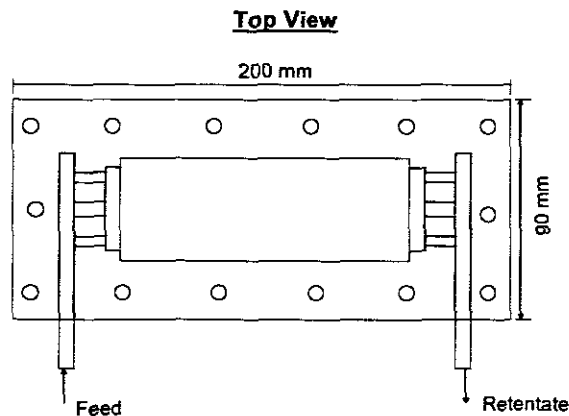


Figure 4.2: Top view of flat-sheet test module used in the MF system (Li, 2002).

4.2.2 Ultrasonic measurement system

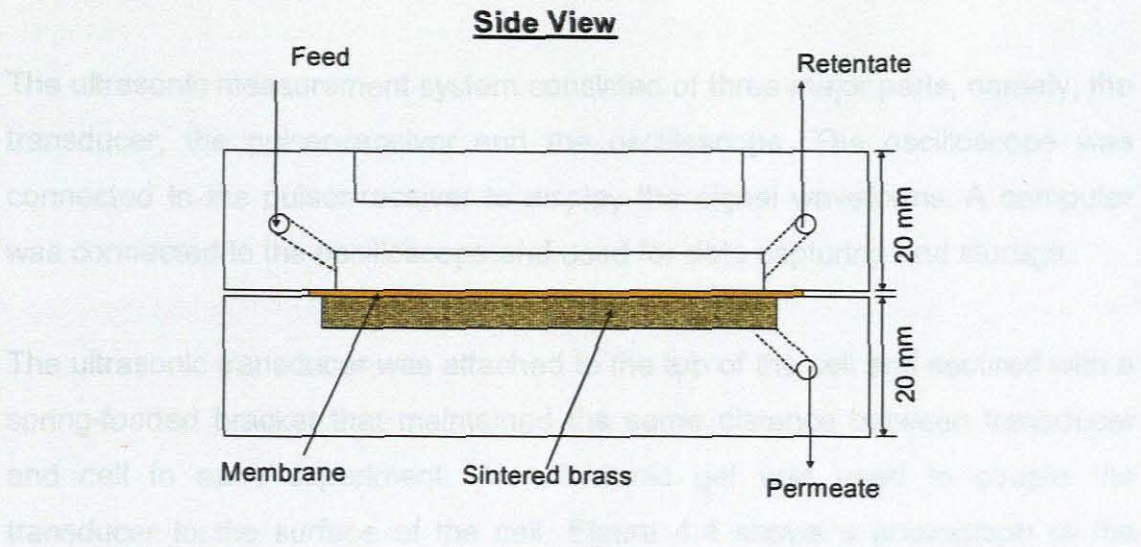


Figure 4.3: Side view of flat-sheet test module used in the MF system (Li, 2002).

It is important to obtain accurate pressure and flow readings during the experiments. In order to achieve this, the pressure and flow sensors were used for automated measurements. Three pressure transducers and a Burkert magnetic flow meter (WIKA Instruments; Milnerton) were incorporated into the system. A flow meter was installed on the feed line. The pressure sensors were installed on the feed, retentate and permeate lines.

The sensors were interfaced with a 16-bit NI PCI-6014 data acquisition card (NI Solutions, Midrand) to a computer. The data acquisition card digitised the analog measurements. This allowed measurements to be displayed, logged and recorded with a data acquisition program. This program was written/programmed with LabVIEW® 7.1 software (NI Solutions (PTY) LTD, Midrand) and was used to log and record measurement data at set intervals. A user manual for the use of the program was compiled (see Appendix 2).

A high voltage pulser-receiver (Panametrics 5050PR) was used for sending electrical impulses to and receiving measurement signals from the transducer. The pulser-receiver design was suitable for ultrasonic testing and measurement applications that require a high material penetration capability. The instrument had a bandwidth of 10 MHz. The Panametrics had a maximum voltage pulse

4.2.2 Ultrasonic measurement system

The ultrasonic measurement system consisted of three major parts, namely, the transducer, the pulser-receiver and the oscilloscope. The oscilloscope was connected to the pulser-receiver to display the signal waveforms. A computer was connected to the oscilloscope and used for data capturing and storage.

The ultrasonic transducer was attached to the top of the cell and secured with a spring-loaded bracket that maintained the same distance between transducer and cell in each experiment. An ultrasonic gel was used to couple the transducer to the surface of the cell. Figure 4.4 shows a photograph of the oscilloscope, the pulser-receiver and the computer used for the experiments.



Figure 4.4: A photograph of the ultrasonic equipment used in the study, showing the Panametrics 5058PR pulser-receiver under the HP 54602B oscilloscope and a computer on the far right.

4.2.2.1 Pulser-receiver

A high voltage, pulser-receiver (Panametrics 5058PR) was used for sending electrical impulses to and receiving measurement signals from the transducer. The pulser-receiver design was suitable for ultrasonic testing and measurement applications that require a high material penetration capability. The instrument had a bandwidth of 10 MHz. The Panametrics had a maximum excitation pulse

of up to 900 volts. The receiver section provided 60 dB RF gain, with an additional 30 dB available from an integral auxiliary pre-amplifier. Pulse voltage was adjusted by four values, from 100 to 900 volts. A front panel meter was used to monitor the voltage applied to the transducer. The receiver gain knob was selectable as either 40 or 60 dB, while the receiver attenuation knob was adjustable from 0 to 80 dB in 1dB steps, with a vernier setting of ± 1 dB for precision control.

The following parameters were set on the pulser-receiver:

Repetition rate: 200 Hz

Damping: 50 ohms

Pulse height: 200 V

Attenuation: 25 dB

Gain: 60 dB

The high-pass filter and the low-pass filter were not used. The instrument was operated in the pulse-echo mode.

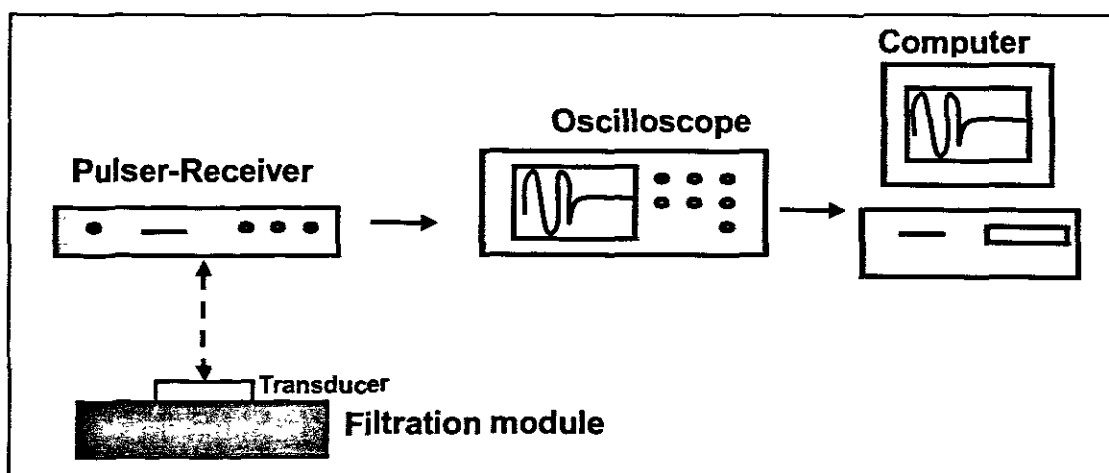


Figure 4.5: Schematic representation of the connections between the transducer, the pulser-receiver, the oscilloscope and the computer.

4.2.2.2 Oscilloscope

A Hewlett Packard 54602B oscilloscope (shown in Figure 4.5) with the bandwidth of 150 MHz was used. The other important parameters of the HP oscilloscope were: sweep speed varying between 5 seconds per division to 2 nanoseconds per division and the vertical sensitivity was 1 mV per division. The sampling rate of the instrument was 150 megasamples per second. The input-output function consisted of an 8-bit digitiser and a RS 232 serial interface. The ultrasonic data was captured at required regular intervals and the data saved on the computer.



Figure 4.6: Photograph of the Hewlett Packard 54602B oscilloscope.

4.2.2.3 Ultrasonic transducer

Panametrics Videoscan transducers V111-RB and V120-RB, with the central frequencies of 10 MHz and 7.5 MHz, respectively, were available for the tests. Videoscan transducers are untuned transducers, which provide heavily damped broadband performance. In previous studies, 10 MHz and 7.5 MHz transducers had shown the best responses for the system under investigation (Li, 2002). The results presented herein are those from the 7.5 MHz transducer.

4.3 MATERIALS

4.3.1 NBW source

The NBW from the Buffelsrivier municipal dam located in the Overstrand District, Western Cape, was used for tests in this study. This source was chosen for two reasons. There is less variation in the composition of large, stagnant, water bodies water (dams and lakes) than the running water, such as rivers (Frimmel & Hesse, 1996; Krasner *et al.*, 1996). The second reason was that the source was only one-hour's drive from Stellenbosch (where the experiments were undertaken). Table 4.1 shows a typical composition of the NBW used in this study.

Table 4.1: Typical composition of the NBW from Buffelsrivier municipal reservoir, used in this study.

Parameter	Units	Raw Water	Max. Allowable (SABS 241).
pH	-	7,60	4,0-10,0
Conductivity	mS/m	15,1	370
Turbidity	NTU	1,1	10
TOC	mg/l	8.3	-
DOC	mg/l	8.2	10
Colour	mg/l	205	50
Total alkalinity (as CaCO ₃)	mg/l	5,6	-
Total hardness (as CaCO ₃)	mg/l	18,0	-
Calcium hardness (as CaCO ₃)	mg/l	13,5	750
Magnesium hardness (as CaCO ₃)	mg/l	4,5	412
Chloride (as Cl)	mg/l	42,0	600

Organic carbon is a sum parameter for organic matter. Dissolved organic carbon (DOC) or total organic carbon (TOC) was used as the indicator of the NOM content in NBW. However, information about content of HS could not be obtained as NOM is a range of mixed organic substances (Peuravuori, *et al.*, 1999). The DOC content of the water was within the acceptable standards set by the South African Bureau of Standards (SABS 241). However, the colour content the water was extremely high.

The HA and FA content of NBW from a dam differs significantly from that of running water (Schäfer, 2001; Thurman, 1985). A comparison of the composition of dam water (Figure 4.7) to that of running water (Figure 4.8) is shown.

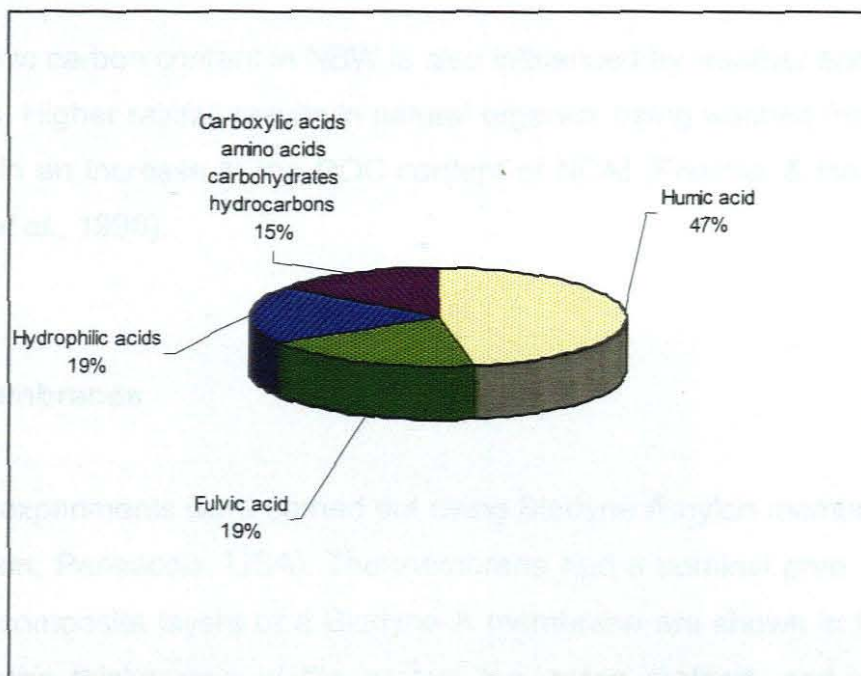


Figure 4.7: Typical composition of dam water (Schäfer, 2001).

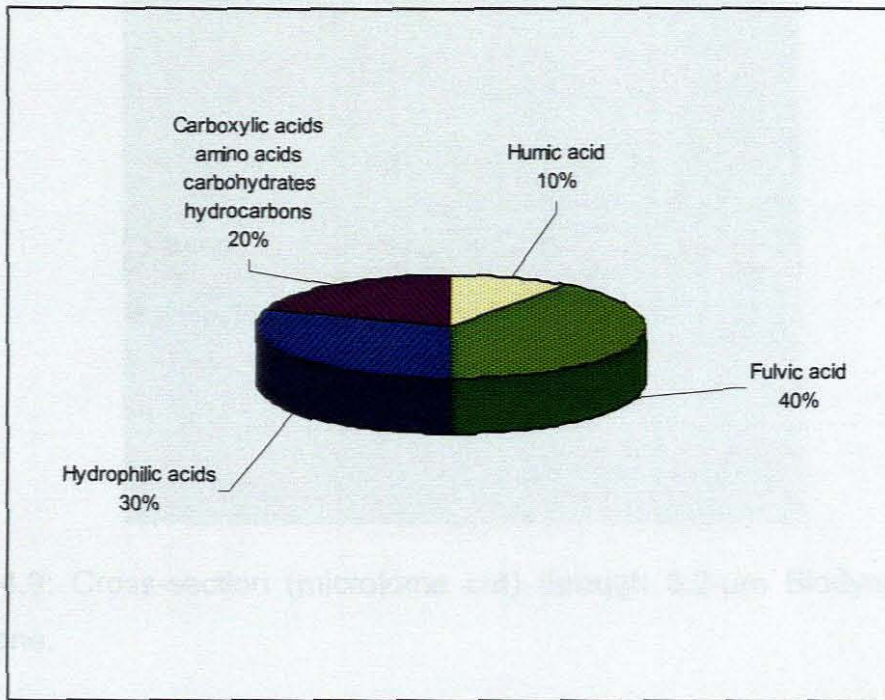


Figure 4.8: Typical composition of river water (Schäfer, 2001; Thurman, 1985).

The organic carbon content in NBW is also influenced by weather and seasonal variations. Higher rainfall results in natural organics being washed from the soil, resulting in an increase in the DOC content of NOM (Frimmel & Hesse, 1996; Krasner *et al.*, 1996).

4.3.2 Membranes

Filtration experiments were carried out using Biodyne A nylon membranes (Pall Corporation, Pensacola, USA). The membrane had a nominal pore size of 0.2 μm . The composite layers of a Biodyne A membrane are shown in Figure 4.9. The average thicknesses of the porous top, nylon support, and the porous bottom layer were 45 μm , 50 μm and 55 μm respectively.

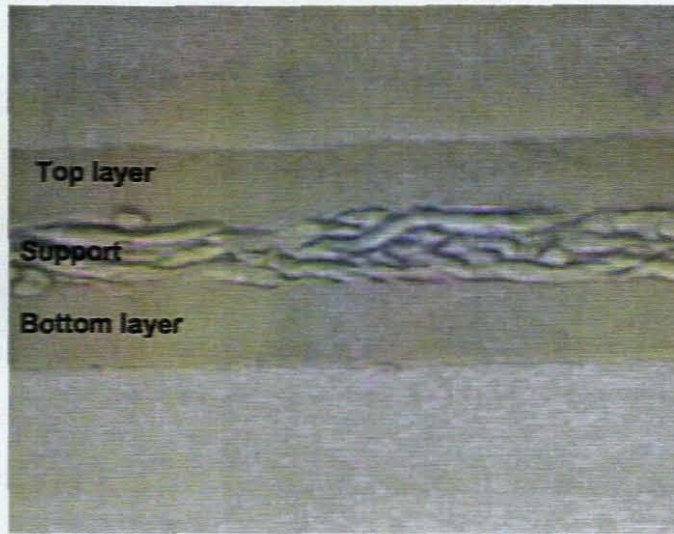


Figure 4.9: Cross-section (microtome cut) through 0.2- μm Biodyne A nylon membrane.

SEM and AFM were used for the morphological analysis of the membrane surfaces. Figure 4.10 shows a SEM micrograph of a clean Biodyne A membrane; the pores in the membrane are visible. The SEM image of this clean membrane was used for comparison with images of fouled membranes (to determine the extent of surface coverage by fouling).

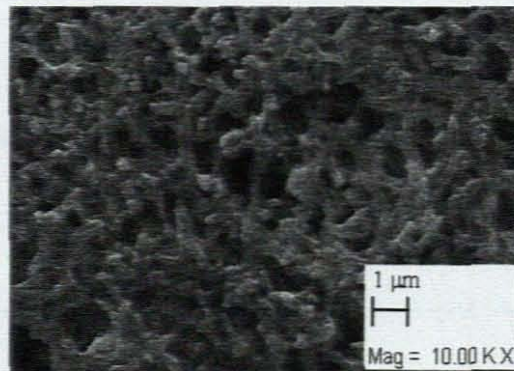


Figure 4.10: Electron micrograph of a Biodyne A membrane at 10 000 times magnification.

The Biodyne A membrane was also characterised by AFM (Figure 4.11). The AFM topography image of the membrane showed features similar to those of the electron micrographs.

4.4 METHODS

4.4.1 Fouling Experiments

The fouling experiments were conducted using a dead-end module. The feed flow rate was maintained at 100 mL/min and the pressures of between 10 and 150 kPa.

Initially, de-ionised water was filtered through the membrane for the experimental for 30 minutes. This was done to ensure that the membrane was fully wetted and to remove any air bubbles. The fouling experiments were then conducted using a feed solution of de-ionised water containing a known concentration of foulant.

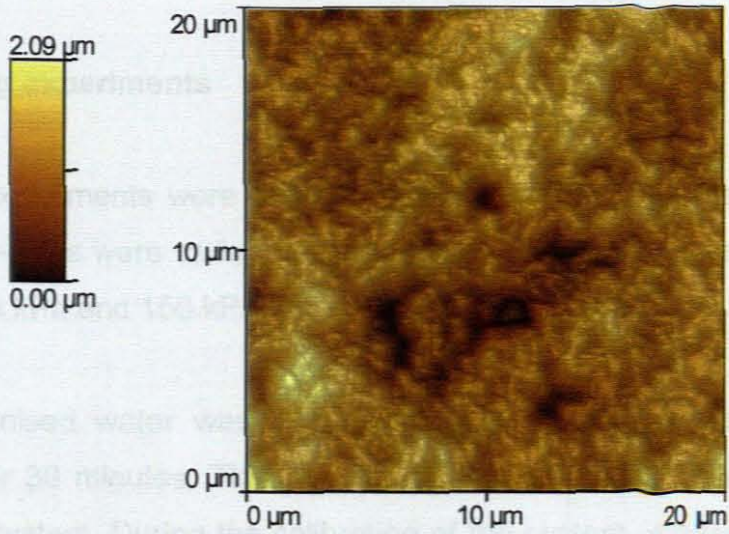


Figure 4.11: AFM image of a Biodyne A membrane.

The membrane was also characterised by PWF at dead-end filtration. This test was performed at dead-end at 25 °C with pressures between 10 and 150 kPa so, as to determine the PWF permeability of the membrane. Figure 4.12 shows the TMP versus PWF graph obtained by filtering de-ionised water through the membrane at dead-end.

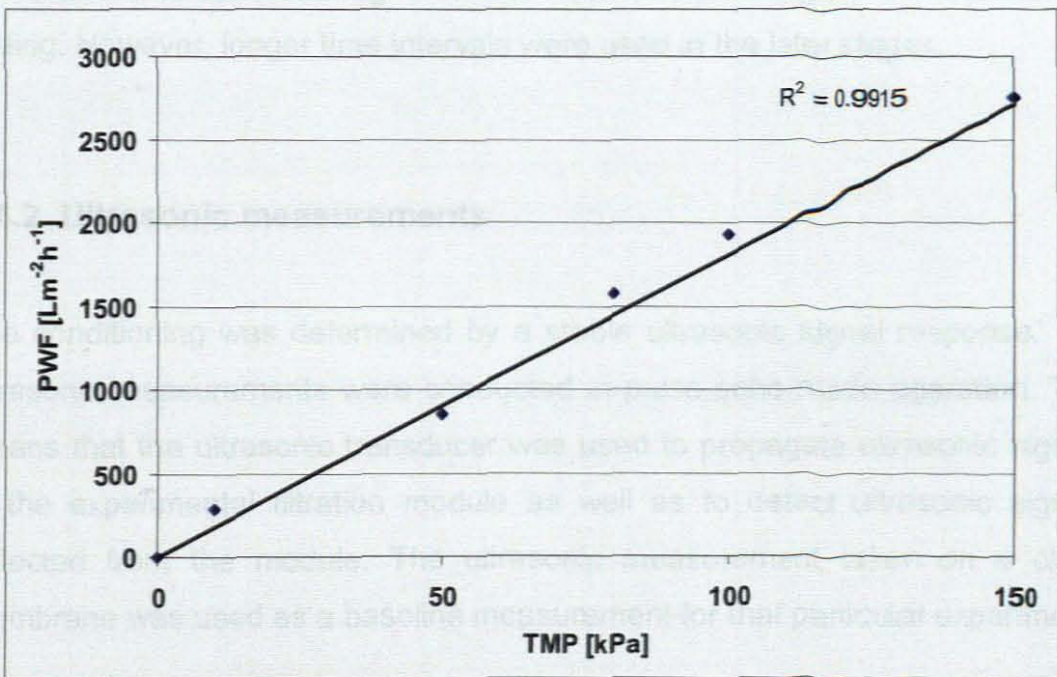


Figure 4.12: A graph of PWF plotted against TMP for a Biodyne A membrane.

4.4 METHODS

4.4.1 Fouling experiments

The fouling experiments were carried out in cross-flow and dead-end modes. The feed flow-rates were varied between 3 and 80 L/h, at operating pressures of between 10 kPa and 150 kPa.

Initially, de-ionised water was pumped through at the flowrate set for the experiment for 30 minutes. This was done to condition the membrane and to calibrate the system. During the calibration of the system, a baseline ultrasonic signal was recorded. Then the feed source was switched from de-ionised water to the effluent with a 3-way valve. The permeate flux was weighed with a balance and was timed with a stopwatch.

The fouling experiments were continued until a fouling layer formed on the membrane surface and until there was little change in flux decline. At the beginning of experiments, ultrasonic signal changes were recorded at 10-second intervals, starting from zero time, to investigate the initiation of fouling. However, longer time intervals were used in the later stages.

4.4.2 Ultrasonic measurements

The conditioning was determined by a stable ultrasonic signal response. The ultrasonic measurements were conducted in pulse-echo mode operation. This means that the ultrasonic transducer was used to propagate ultrasonic signals to the experimental filtration module as well as to detect ultrasonic signals reflected from the module. The ultrasonic measurement taken on a clean membrane was used as a baseline measurement for that particular experiment.

4.4.3 Data processing and analysis

The ultrasonic data obtained from the experiments were processed using the following algorithm:

- Analysis of ultrasonic waveforms data
- Determining of differential signals from baseline measurements
- Wavelet transformation of signals

The processing of ultrasonic data largely included the use of digital methods and mathematical software. Wavelet transformation of ultrasonic signals was performed by using a mathematical software program, AGU-Vallen Wavelet, which was developed in collaboration between Vallen-Systeme GmbH (Munich, Germany) and Aoyama Gakuin University (AGU) (Tokyo, Japan). This is a tool used to calculate the Gabor WT on individual waveform data sets. The wavelet data were stored as transient data files (*.tra). The settings for the calculations by the wavelet software program were configured as shown in Table 4.2:

Table 4.2: Settings for wavelet calculations by AGU-Vallen Wavelet software

WT setting	Description	Set value
Maximum frequency	The WT is calculated up to this maximum frequency	15 000 kHz
Frequency resolution	Interval to calculate the WT	10 kHz
Number of samples	Number of data points in waveform signal to be analysed	2000
Wavelet size	Size, in number of samples of the wavelet window	50

4.4.4 Fouling layer analysis

After the fouling experiments, the fouled membranes were removed from the filtration module and prepared for analysis by SEM and AFM. Comprehensive comparisons were made between the clean and the fouled membranes.

Membrane samples to be investigated by SEM were coated with platinum or gold in order to prevent electron charging effects from the sample, which interfere with imaging. Precautions were taken not to damage the samples with the electron beam during SEM analyses. The SEM measurements were performed with a LEO S440 SEM instrument. The instrument was set at 10 kV and a 20-mm working distance.

The AFM measurements were performed in contact mode, using a TopoMetrix® AFM Explorer instrument. The instrument was fitted with soft silicone probes (with a spring constant of between 0.07 and 0.4 N/m) (Nanosensors). These probes were suitable for measuring very soft samples such as the polymer membranes and membrane fouling. Extreme precautions were taken so as to avoid damaging the membrane samples with the AFM tip. The probe cantilever was 450 μm long, 50 μm wide and 2.0 μm thick.

CHAPTER 5

RESULTS AND DISCUSSION

5.1 INTRODUCTION

Results that were accomplished during this study are presented and discussed in this chapter. At the beginning of this study, preliminary experiments were conducted to investigate ultrasonic reflections of the filtration module under different conditions, other than when used in filtration. For example, the module was tested when it was in a dry state or when the membrane was removed from the module. A summary of these results is attached in Appendix 3. As mentioned in the previous chapter, the data analysis largely included the digital methods of ultrasonic signals. Each of the ultrasonic signal sets had 2000 data points. The wavelet files were very large, resulting in diagrams that were too elaborate to handle.

5.2 ULTRASONIC RESPONSES

The complete ultrasonic response spectrum obtained from measuring the filtration module shown in Figure 5.1. These echoes resulted from different interfaces in the module at which energy is reflected back to the transducer. The first echo is a reflection from the top perspex and water interface and the second echo is a reflection from the water membrane interface (encased by a square in Figure 5.1). The echoes that follow are reflections from the sintered brass membrane support and perspex interface.

It is important to note that the peaks in the spectrum resulted from the combinations of different pulses and multiple reflections that arrived at the transducer with energy that had not fully dissipated. However, under the same conditions, the compositions of these reflections remained unchanged.

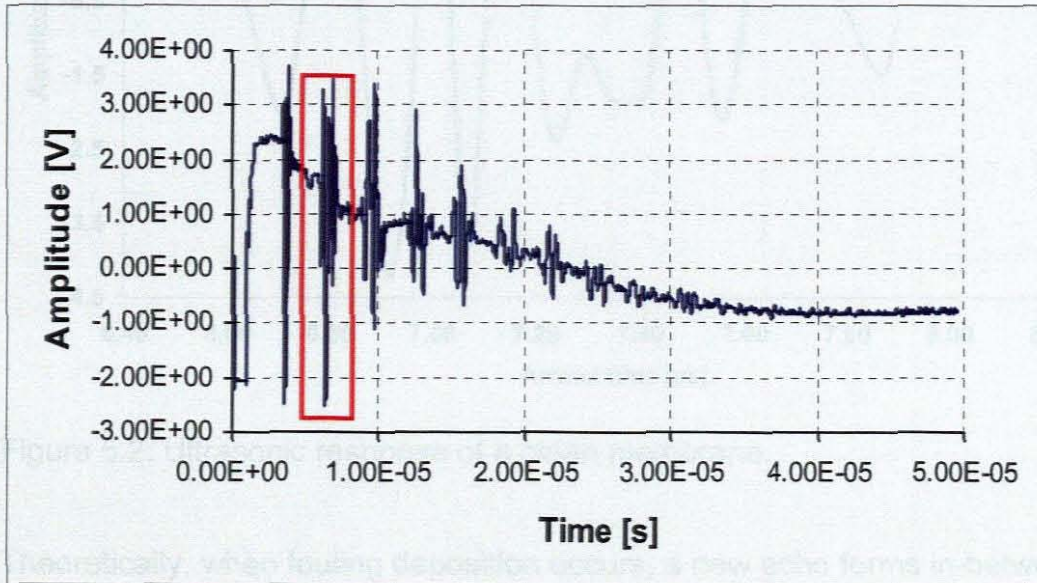


Figure 5.1: Ultrasonic response spectrum of the flat-sheet filtration module. The encased section represents the reflection from the water membrane interface.

The ultrasonic signals obtained from measuring the filtration module were thoroughly studied under varying specific conditions in order to fully understand the trailing echoes. A summary of these results is shown in Appendix 3.

The echo from the water membrane interface was identified as the echo at which changes with respect to membrane fouling occurred. The signal of the identified echo was then monitored for changes during the fouling experiments. Figure 5.2 shows a water-membrane echo from a clean membrane, which was recorded as a baseline measurement in each fouling experiment.

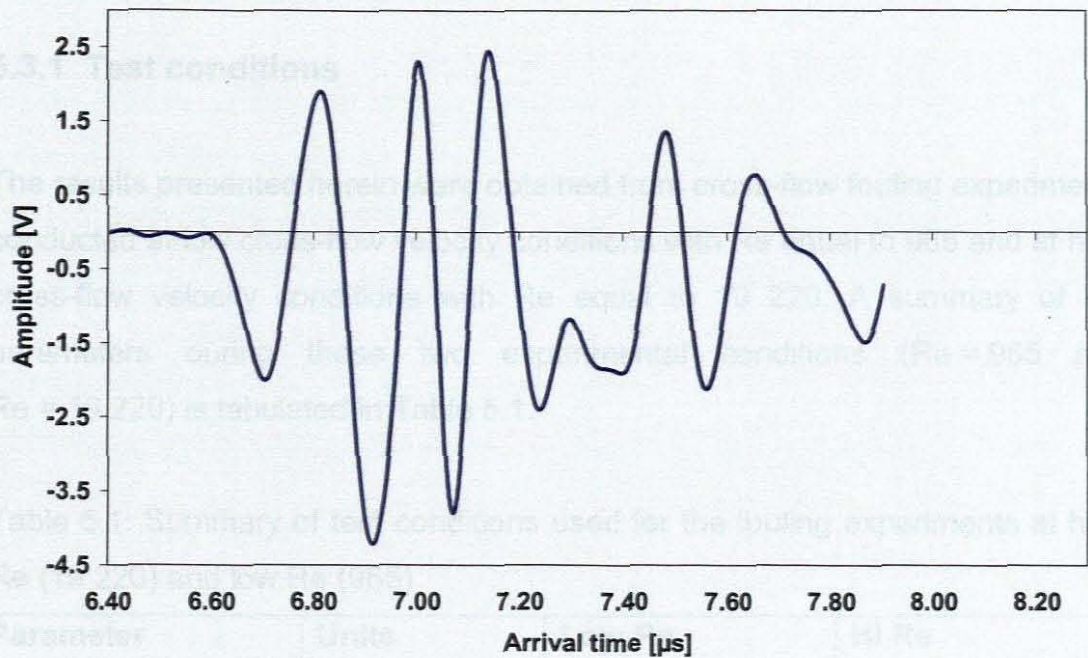


Figure 5.2: Ultrasonic response of a clean membrane.

Theoretically, when fouling deposition occurs, a new echo forms in-between the perspex-water interface and the water-membrane echo (Mairal *et al.*, 1999). However this is only possible if the thickness of the layer falls within the spatial resolution of the system (Koen, 2000). In the results obtained, changes due to fouling were observed on the first positive peak (Figure 5.2).

5.3 CROSS-FLOW FOULING EXPERIMENTS

The fouling experiments that were conducted in cross-flow filtration mode were performed in conditions of both low and high Reynolds numbers (Re). The results presented herein are of the fouling experiments at low cross-flow velocity (low Re) as well as at high cross-flow velocity (high Re). The ultrasonic technique was used and tested its effectiveness when used under these conditions.

5.3.1 Test conditions

The results presented herein were obtained from cross-flow fouling experiments conducted at low cross-flow velocity conditions with Re equal to 965 and at high cross-flow velocity conditions with Re equal to 19 220. A summary of the parameters during these two experimental conditions (Re = 965 and Re = 19 220) is tabulated in Table 5.1.

Table 5.1: Summary of test conditions used for the fouling experiments at high Re (19 220) and low Re (965)

Parameter	Units	Low Re	Hi Re
Feed flow-rate	L/h	3	50
Re	-	965	19 220
Cross-flow velocity	cm/s	2.08	22.4
Pressure	kPa	30	75
Temperature	°C	25	25
PWF	Lm ⁻² h ⁻¹	146.3	231.5
Initial flux	Lm ⁻² h ⁻¹	31	106

5.3.2 Low cross-flow experiment (Re = 965)

This fouling experiment was stopped after 13 hours (780 minutes) of filtration. The ultrasonic recordings were taken every 5 seconds for the first minute and then were taken every 5 minutes.

5.3.2.1 Permeate flux decline

Figure 5.3 shows a graph of the operation time versus the permeate flux for the cross-flow fouling experiment ($Re = 965$). The flux decreased very rapidly in the early stages of the experiment and then showed a more gradual decline after 10 minutes. The effect was due to the laminar flow conditions in the flow channel, allowing the foulant matter to settle. After 60 minutes, the initial permeate flux of $31 \text{ Lm}^{-2}\text{h}^{-1}$ had dropped to 77% ($24 \text{ Lm}^{-2}\text{h}^{-1}$). After 780 minutes of filtration, the flux had dropped by 55% to $14 \text{ Lm}^{-2}\text{h}^{-1}$.

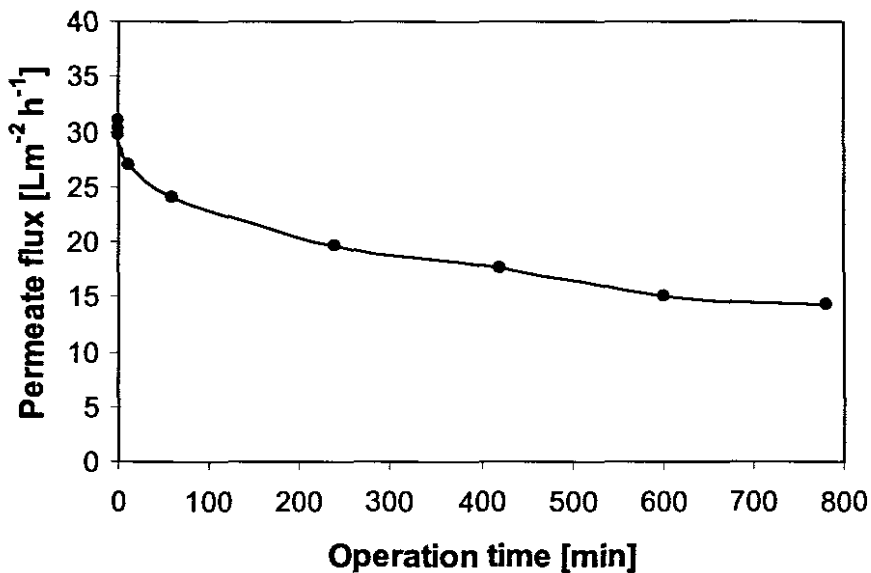


Figure 5.3: Flux decline as a time function for the low cross-flow velocity ($Re = 965$) fouling experiment.

The flux decrease of this nature was attributed to sealing of the pores by NOM fouling. At this point the signs of a cake layer were not yet observable from the membrane top (this was monitored through the transparent perspex module). The flux curve was correlated to the growth of the fouling thickness, the fouling resistance and the amplitude of the fouling peak on the waveform. The graphs plotted for these comparisons are presented in Figure 5.5.

5.3.2.2 Ultrasonic response

Figure 5.4 shows the ultrasonic response waveforms recorded during the low crossflow fouling experiment. The ultrasonic response waveforms are superimposed by 2 V above one another, with the initial or baseline (0 min) waveform at the origin of the amplitude axis.

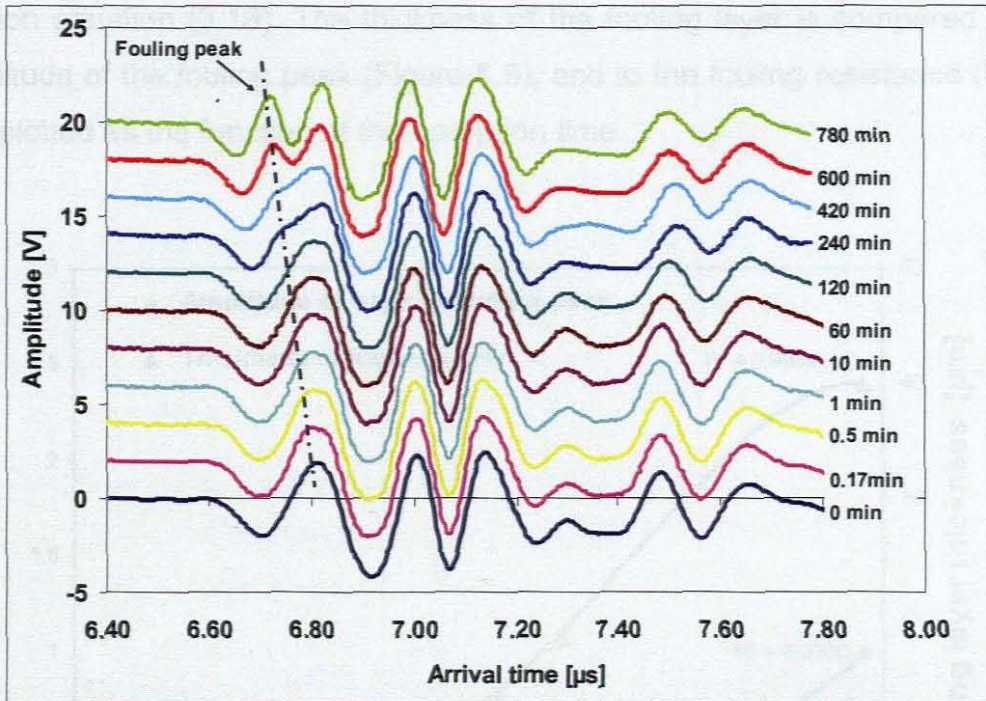


Figure 5.4: Ultrasonic response waveforms for low cross-flow MF fouling experiment ($Re = 965$).

The ultrasonic response signals show that a new peak developed as fouling progressed. These changes occurred on the first positive peak of the signal waveform. There are changes in the rest of the echo signal that also occurred for two main reasons. First, because less energy arrived at the water/membrane interface due to a new water/fouling layer interface. Second, the changes in amplitude were due to change in membrane properties (density), due to NOM adsorption on the membrane surface (Li, 2002). The changes in properties of the membrane influence both the propagation of sound wave in the membrane itself and on the reflection coming from the membrane/metal support interfaces. Hence, the difference between any signal

and the baseline signal contain not only information about the fouling layer but also about the other changes produced. Figure 5.4 shows that the changes in the region of approximately 6.7-6.9 μs of the waveforms occurred because of the continuously growing fouling layer. The higher reflection from the fouling layer reduces the strength of the reflected energy from the underlying layers of the module.

The thickness of the fouling layer was calculated using the time-distance relation equation (3.18). The thickness of the fouling layer is compared to the amplitude of the fouling peak (Figure 5.5), and to the fouling resistance (Figure 5.6) plotted as the function of the operation time.

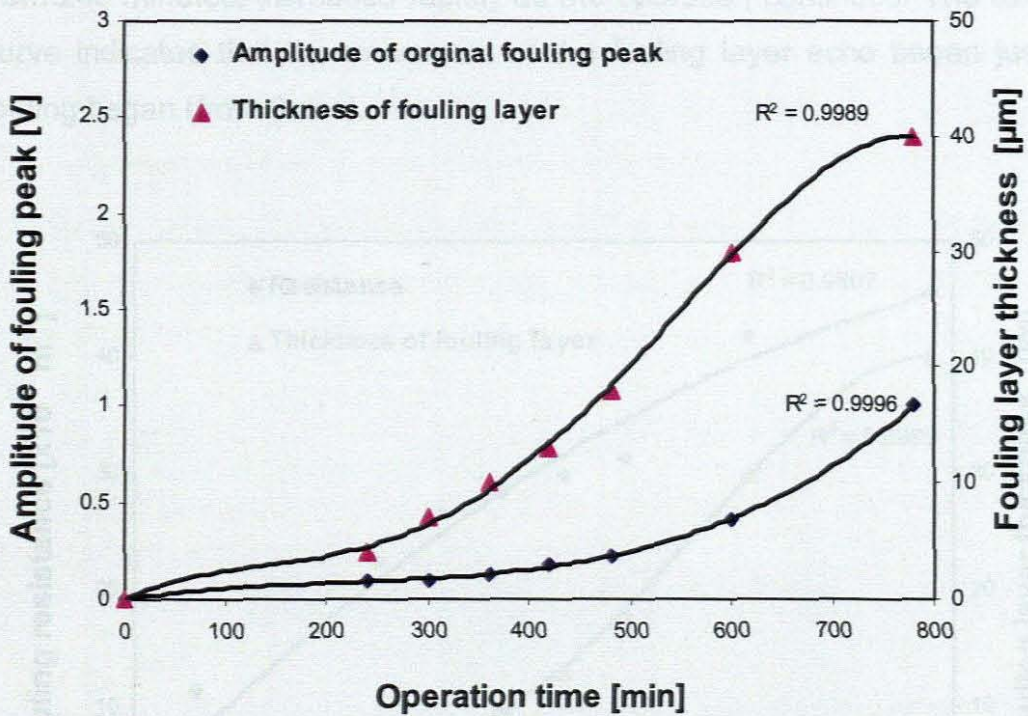


Figure 5.5: Increase of fouling layer thickness and fouling peak amplitude with time ($Re = 965$).

The amplitude of the first positive peak of the baseline waveform was taken as the corresponding point of the first visible fouling peak at 240 minutes (6.764 μs), which was 0.25 V. The graph in Figure 5.5 shows that the amplitude of the fouling peak increased slowly until about 400 minutes, but faster afterwards. For example, the fouling peak amplitude of the original shows an increase from 0.0 V in the beginning to 0.09 V after 240 minutes, 0.25 V after 520 minutes and 1.0 V after 780 minutes. This means that the density of the fouling layer was very low at the initial stage (up to about 400 minutes), a little higher than water, which resulted in a weak reflection echo. Afterwards, the density of the fouling layer increased because of the compaction and consolidation the layer by pressure and further deposition of NOM, the reflection echo from which became stronger. The thickness of the fouling layer, which could be determined from 240 minutes, increased rapidly as the operation continued. The thickness curve indicates that the movement of the fouling layer echo began just after fouling began (from 0 sec).

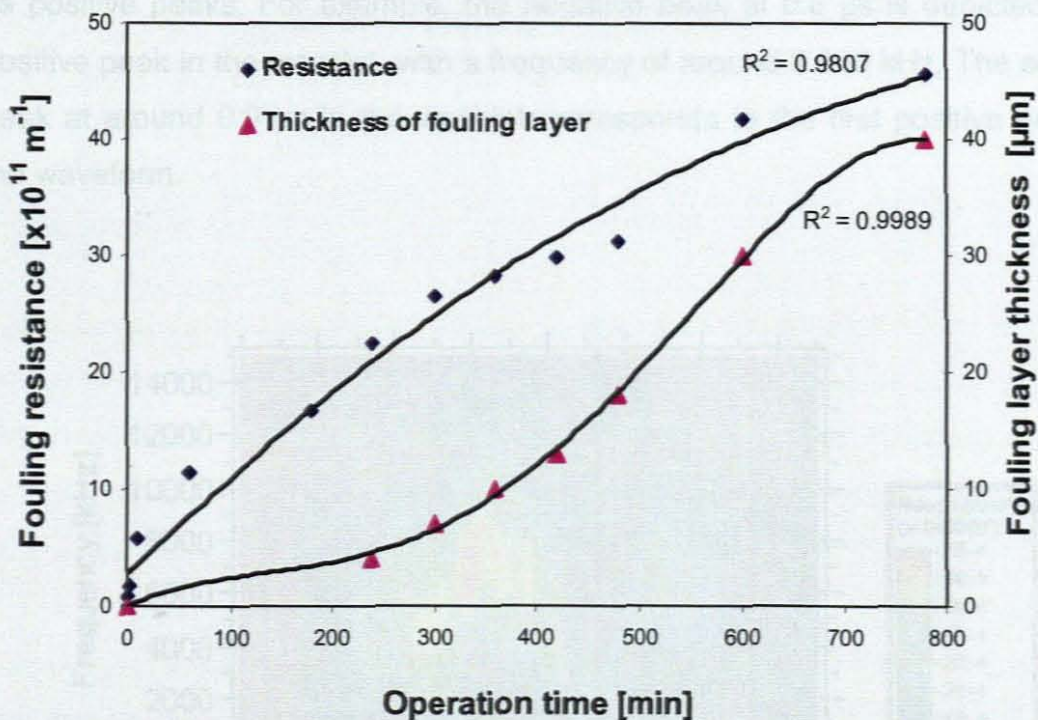


Figure 5.6: Increase of fouling resistance as fouling layer thickness increases time ($\text{Re} = 965$).

Figure 5.6 shows that the fouling resistance curve increased but almost flattened at the later stages of the experiment. At this stage, the curve corresponded to the fouling thickness curve which shows that at this stage fouling was growing slowly.

5.3.2.3 WTs of ultrasonic signals

Wavelet transformation was applied to each of the ultrasonic signals (waveforms) shown in Figure 5.4. Interpretation of the wavelets requires an understanding of the WT of the baseline signal waveform (from a clean membrane). Figure 5.7 shows the wavelet of the signal measured from a clean membrane during the initial stages of the experiment. The wavelet is displayed in a contour plot. The different contour shades in the wavelet represent the magnitude of the WT, as shown by the legend next to the wavelet (Figure 5.7). The negative peaks (in the waveforms) were portrayed by the wavelet program as positive peaks. For example, the negative peak at $0.8 \mu\text{s}$ is depicted as a positive peak in the wavelet, with a frequency of around 8 000 kHz. The second peak at around $0.9 \mu\text{s}$ in the wavelet corresponds to the first positive peak in the waveform.

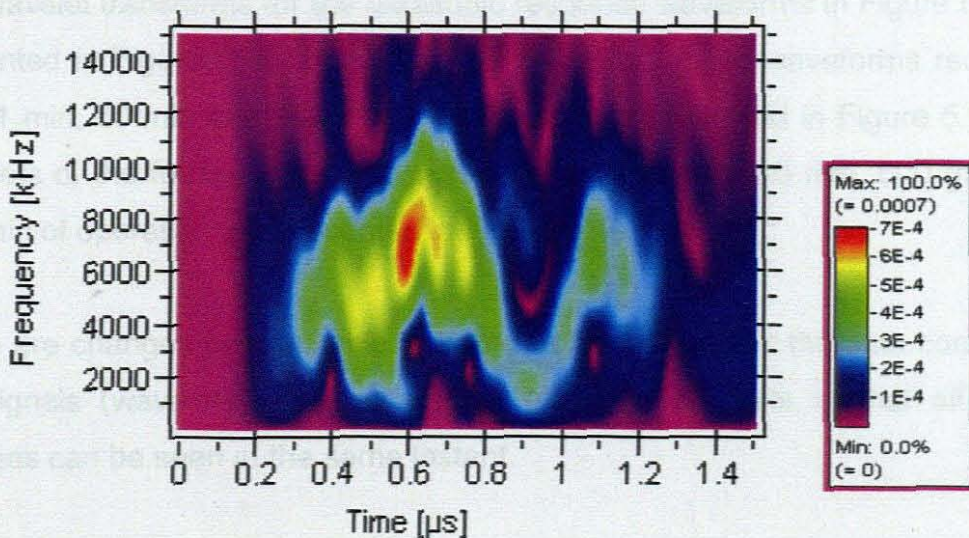


Figure 5.7: WT of an ultrasonic signal from a clean membrane.

A graphic software (SigmaPlot) was used to represent the wavelet in Figure 5.8 as a three-dimensional (3D) plot. The waveform was superimposed on the time scale of the wavelet. This plot provided more clarity, especially with the frequency and WT magnitude components of the wavelet. The major drawback of using these plots is that they are extremely slow to process using ordinary computer processors.

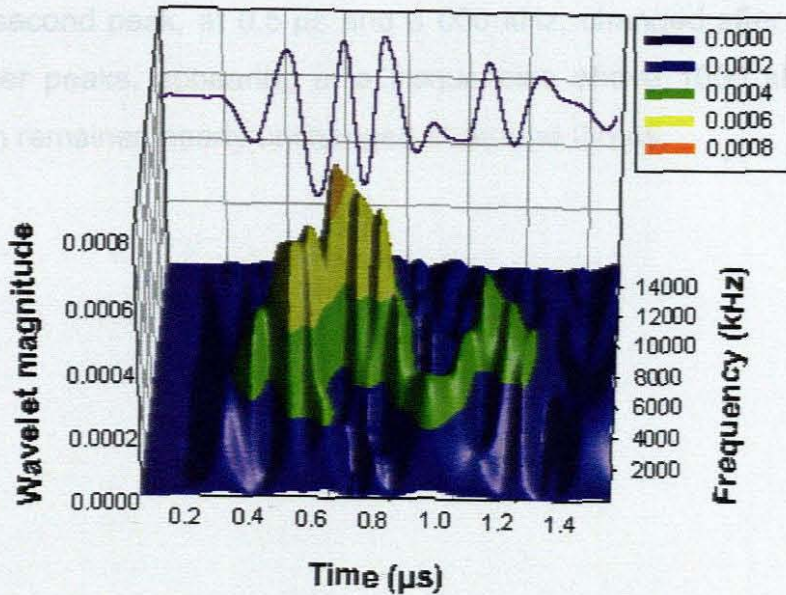


Figure 5.8: 3D representation of the WT of an ultrasonic signal of a clean membrane.

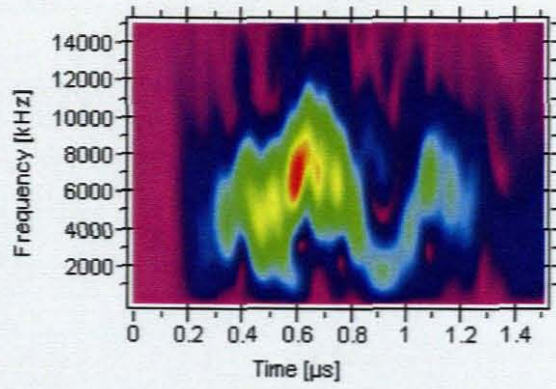
The wavelet transforms for the ultrasonic response waveforms in Figure 5.5 are presented in Figures 5.9 and 5.10. The wavelets for the waveforms recorded after 1 min, 60 min and 240 min of operation are presented in Figure 5.9. The wavelets of the fouling ultrasonic signals recorded after 420 min, 600 min and 780 min of operation are presented in Figure 5.10.

There are changes recognisable in both the frequency and the time content of the signals (wavelets). The advantage of using wavelets is that all these changes can be seen at the same instant.

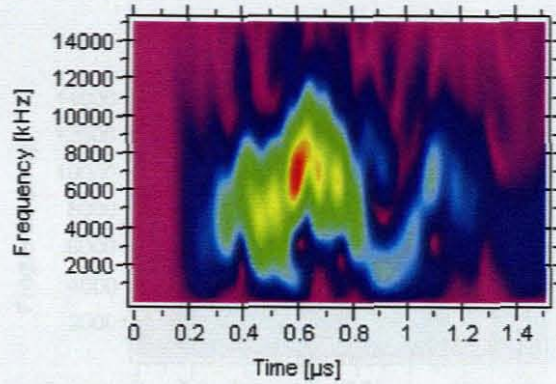
Up until 60 minutes (Figure 5.9), there were few, but significant, changes in the first two small peaks between 0.2 and 0.6 μ s. These changes were not clearly

observable on waveforms but became more evident with the wavelet analysis. The time and frequency composition of the first peak had not changed but the WT magnitude had decreased. This signified that there was an increase in reflected energy due to an increase in density of the fouling on the membrane surface.

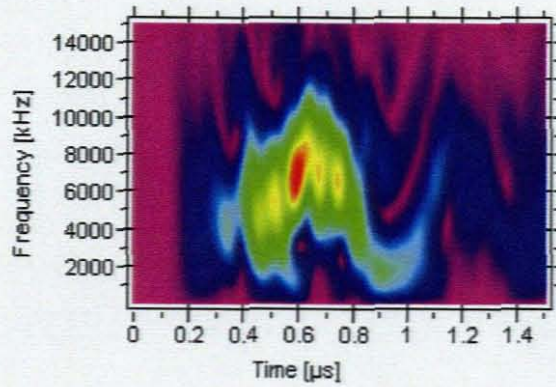
The frequency range or the width in the frequency domain of the third peak at 0.7 μs gradually increased from between 2 000 and 11 000 kHz to about 14 000 kHz. The second peak, at 0.5 μs and 8 000 kHz, changed after 600 min into three smaller peaks, appearing at a frequencies above 1000 kHz. The time composition remained nearly unchanged at around 0.5 μs .



1 min

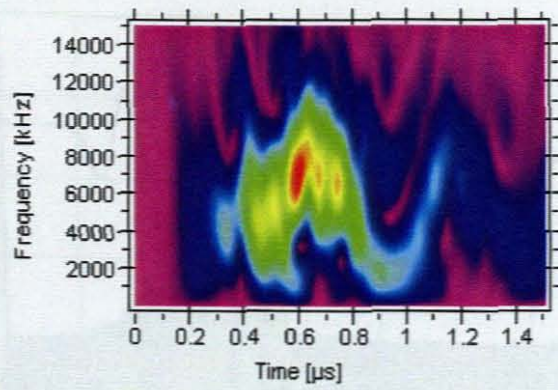


60 min

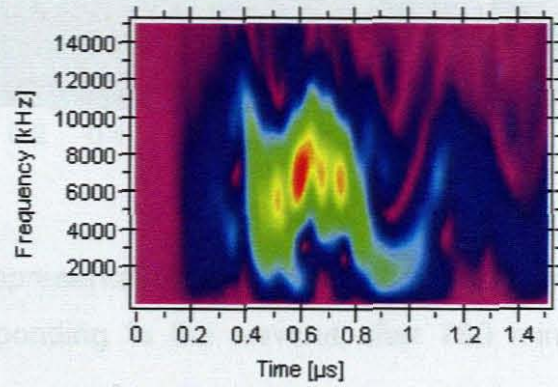


240 min

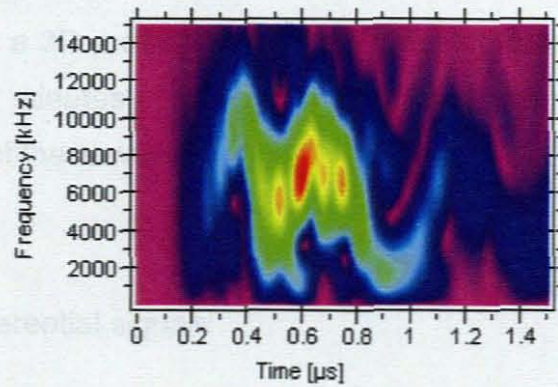
Figure 5.9: WTs of the ultrasonic signals after 1min, 60 min and 240 min of operation ($Re = 965$, cross-flow fouling experiment).



420 min



600 min



780 min

Figure 5.10: WTs of the ultrasonic signals after 420 min, 600 min and 780 min of operation (Re = 965, cross-flow fouling experiment).

Figure 5.11 shows a zoomed-in view of the waveform recorded after 780 min of operation on the time scale of 0.4 to 1.4 μs.

5.3.3.4 WTs of differential

Figure 5.12 shows the differential waveforms of the ultrasonic signals in Figure 5.4. These waveforms are superimposed by 2-V signals and shown one another with the original waveforms. The use of differential signals provided a more sensitive response to fouling than the original waveforms. For example, the first significant change from the baseline signal (ultrasonic response of clean membranes) occurs at a flux decline of about 20%.

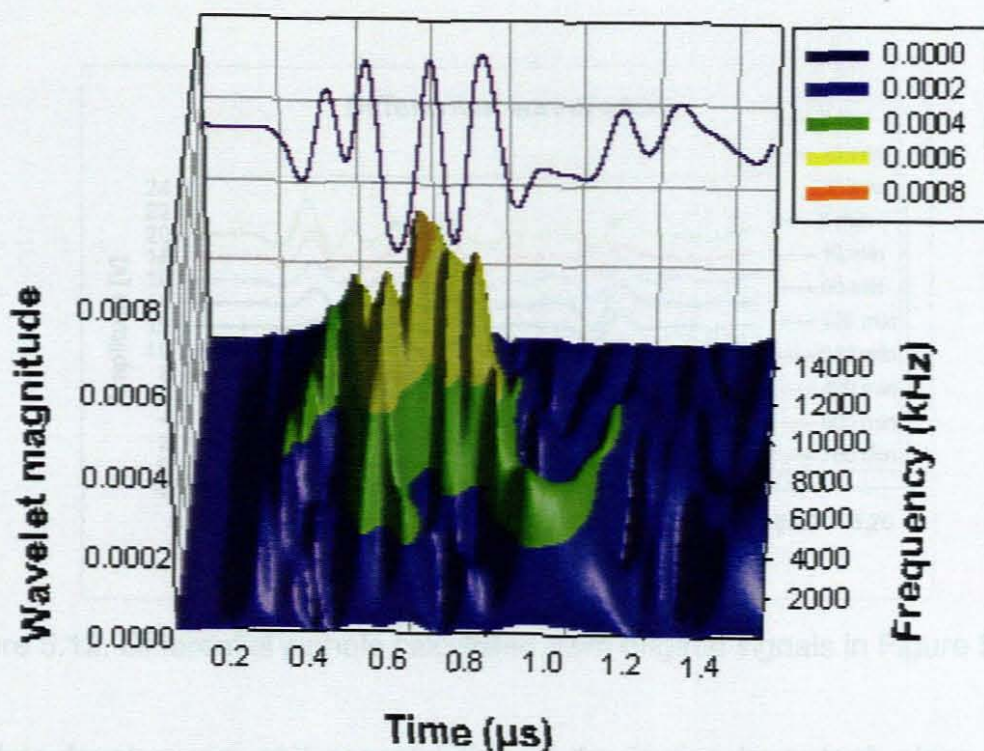


Figure 5.11: 3D representation of the WT of an ultrasonic signal for a fouled membrane corresponding to the wavelet after 780 min of operation (Figure 5.10)

The early peaks can be clearly seen when presented on a large scale (e.g. 0-3 μs). Figure 5.11 shows a 3D presentation of the wavelet transform of the waveform recorded after 780 minutes of fouling. The waveform signal was superimposed on the time scale of the wavelet.

5.3.3.4 WTs of differential signals

Figure 5.12 shows the differential waveforms of the ultrasonic signals in Figure 5.4. These waveforms are superimposed by 2 V above one another, with the initial (0 min) differential waveform at the origin of the amplitude axis. Therefore, the amplitude values corresponding to the arrival time of 6.4 μs were taken as 0 V. Hence, the amplitude values of the differential waveform peaks were calculated. The use of differential signals provided a more sensitive response to that the original ultrasonic response waveforms shown in Figure 5.4. For example, the first significant change from the baseline signal (ultrasonic response of clean membranes) occurs at a flux decline of about 20%.

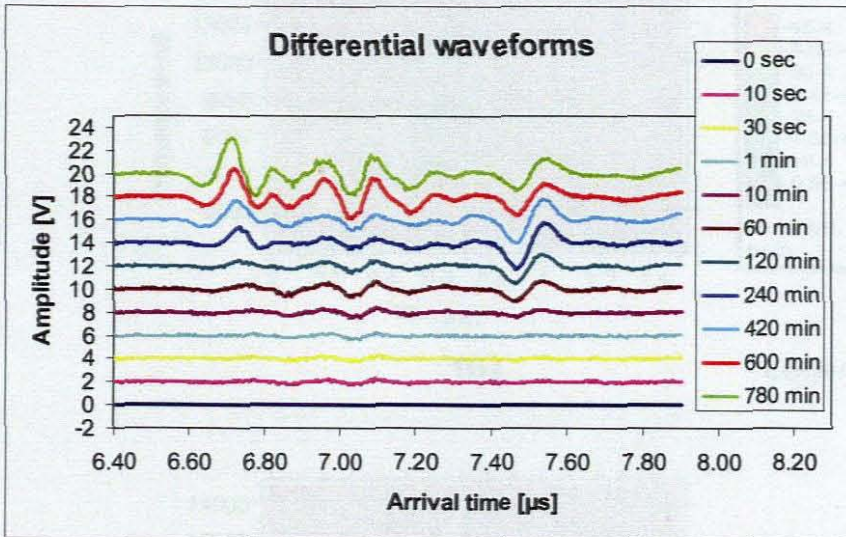


Figure 5.12: Differential signals calculated from original signals in Figure 5.4.

Further development and consolidation of the fouling layer took place as the fouling process progressed. This resulted in large increases in the amplitude of differential peaks, such as 1.96 V at 600 minutes and 2.84 V at 780 minutes.

The early peaks can be clearly seen when presented on a large scale (e.g. 0-3 V). Thus, a differential signal peak at 6.76 μs with amplitude of 0.09 V was evident after 10 seconds of operation. This indicated that there were small changes in waveforms due to fouling in the early stages, which could only be seen by differential waveforms.

The fouling peak (in the fouling layer region) was only visible after 60 minutes (with amplitude of 0.45 V) but when using the differential waveforms it was visible from 10s. The amplitude of the fouling peak in differential waveforms increased significantly to 1.25 V even after 240 minutes, indicating the development of a separate fouling layer. The wavelets of the differential waveforms are presented in Figures 5.13 and 5.14.

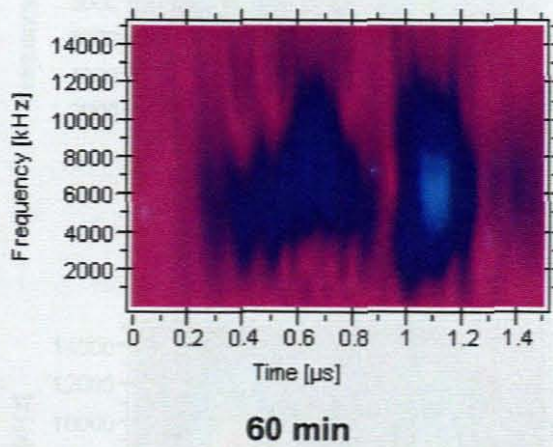
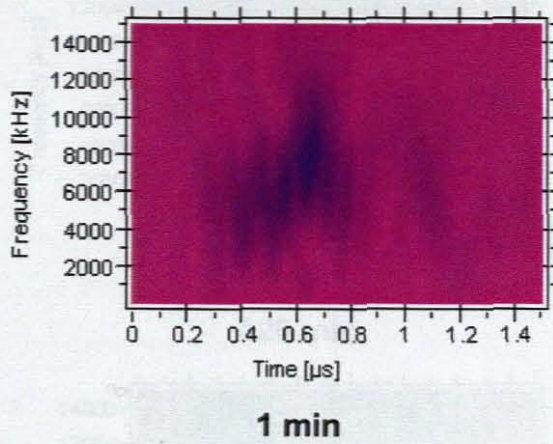
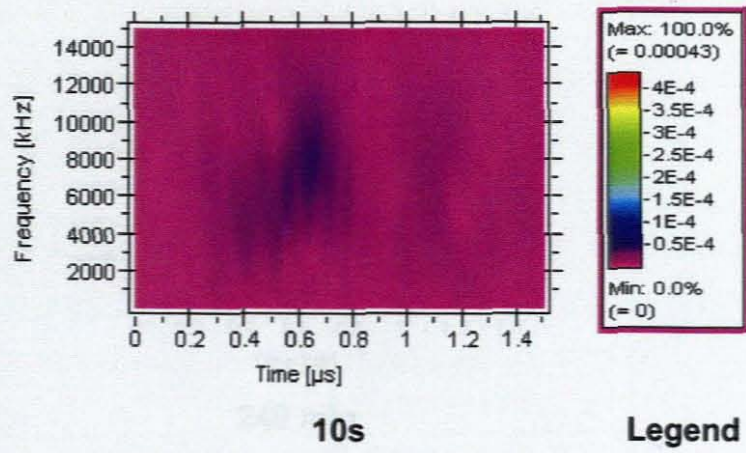
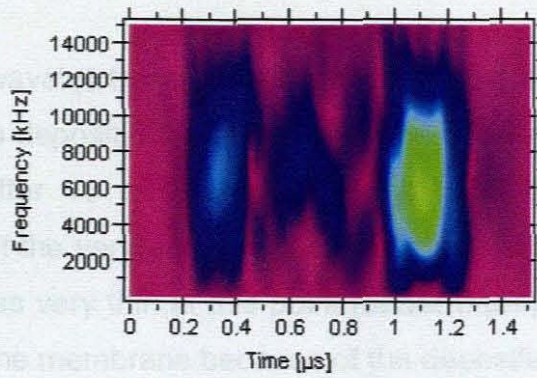
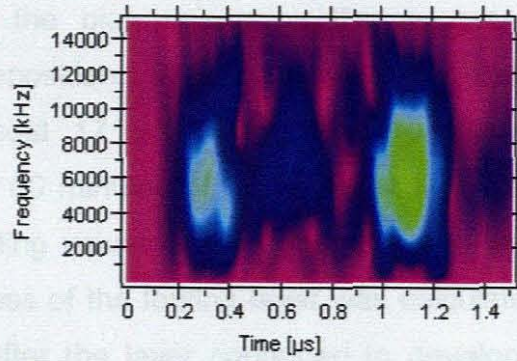


Figure 5.13: WTs of differential waveforms for the low cross-flow ($Re = 965$) fouling experiment after 10 s, 1 min and 60 min of operation.

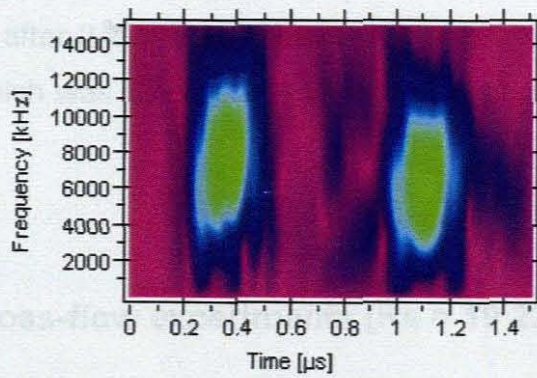
Figure 5.14: WTs of differential waveforms for the low cross-flow ($Re = 965$) fouling experiment after 240 min, 420 min, and 780 min of operation.



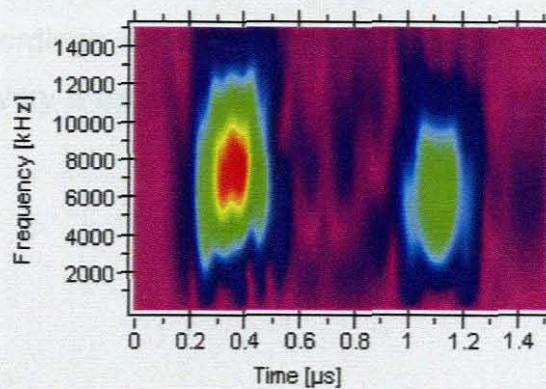
240 min



420 min



600 min



780 min

Figure 5.14: WTs of differential waveforms for the low cross-flow ($Re = 965$) fouling experiment after 240 min, 420 min, and 780 min of operation.

The area on the wavelet transformation of the initial differential waveform is purple signifying no deposition on the membrane. However, the appearance of the blue colour after 10 s (Figure 5.12) indicates that immediate fouling deposition began at the very early stages of filtration of NBW. Considering that the fouling layer was very thin at this point (about 3 μm), this suggested that a density change in the membrane because of the deposited matter.

The deepening of the blue colour on the successive wavelets indicates increasing NOM deposition. The thickness of the deposit, however, did not increase much (about 17 μm) even after 10 minutes. Significant fouling appeared only after 60 minutes of fouling operation, as seen from the wavelet and the corresponding waveform, indicating that a well defined fouling layer formed. The thickness of the fouling layer was calculated to be 41 μm after 60 minutes and thereafter the layer continued to develop both in thickness and density with time. The blue colour in the first few wavelets progressed to the next colour coding after 240 minutes, indicating a fully developed fouling layer, the thickness of which was 59 μm . The thickness increased to 69 μm after 780 minutes.

5.3.3 High Re cross-flow experiments ($Re = 19\ 220$)

This fouling experiment was stopped after 24 hours (1440 minutes) of filtration. The ultrasonic recordings were taken every 5 seconds for the first minute and then were taken every 5 minutes. After an hour, the measurements were taken every hour.

5.3.3.1 Permeate flux decline

The change in permeate flux over time during the high cross-flow velocity fouling experiment ($Re = 19\,220$) is shown Figure 5.15. The flux curve in Figure 5.15 shows a shape similar to that of the graph observed in the low cross-flow velocity fouling (Figure 5.3) but the flux took longer to drop because of the higher cross-flow velocity.

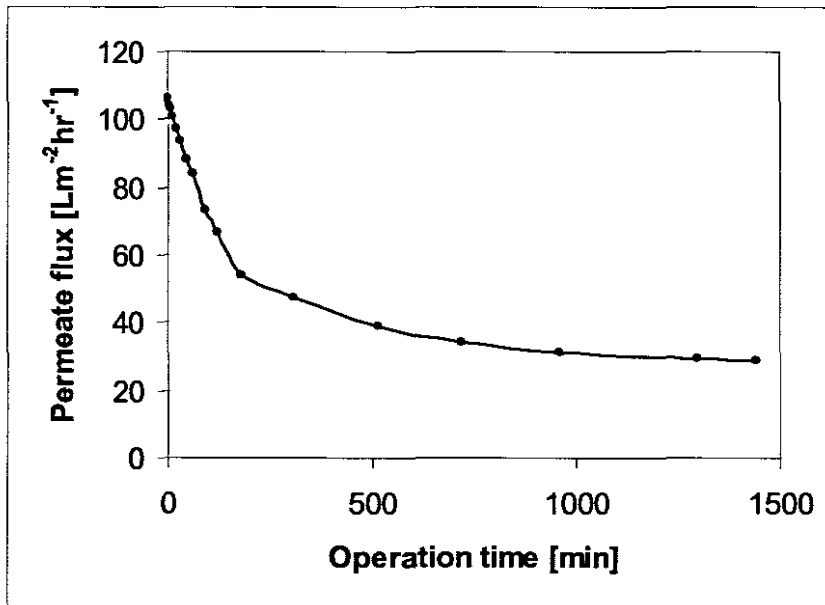


Figure 5.15: Flux decline as a time function for the high cross-flow velocity ($Re = 19\,220$) fouling experiment.

After 60 minutes of operation, the flux had dropped by only 21% of the initial flux, as compared to the flux drop in the experiment with a low pressure and low cross-flow velocity. The high cross-flow velocity and turbulence in the flow channel aided in minimising the extent to which the foulants accumulated at the surface of the membrane. After 500 minutes of operation, the decrease became more gradual, as seen in Figure 5.4. During this time the flux had decreased to 37% ($39.2 Lm^{-2}hr^{-1}$) of the initial permeate flux.

5.3.3.2 Ultrasonic response

Figure 5.16 shows the ultrasonic response waveforms for the low Re and high Re experiments, respectively. The ultrasonic response waveforms were superimposed by 2 V above one another, with the initial (0 min) waveform at the origin of the amplitude axis. Therefore, the amplitude values corresponding to the arrival time of 6 μ s in Figure 5.16 were taken as 0 V.

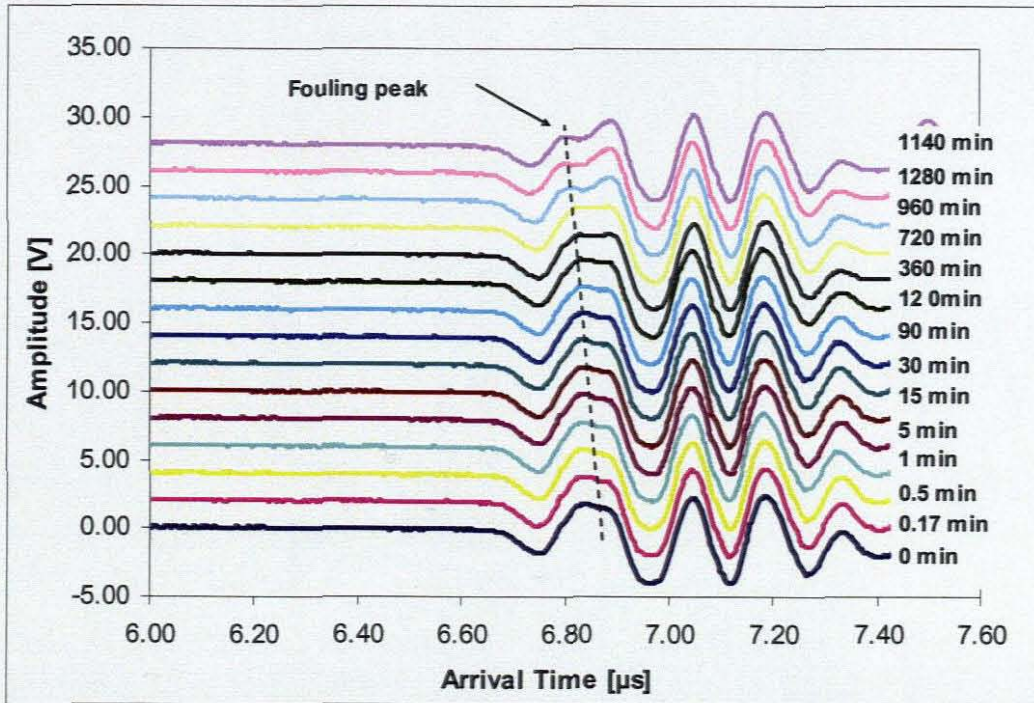


Figure 5.16: Changes in the ultrasonic response during high Re cross-flow MF fouling experiment ($Re = 19\,220$).

The ultrasonic response waveforms (Figure 5.16) show that the changes that were related to fouling occurred on the first positive peak of the echo. A new peak started to form as fouling progressed. This is agreement with the distance and time relation described by equation (3.18). As the fouling gradually increased in thickness, the distance of the reflected ultrasonic wave became shorter, resulting in the arrival time of the signal gradually decreasing.

5.3.3.3 WTs of ultrasonic signals

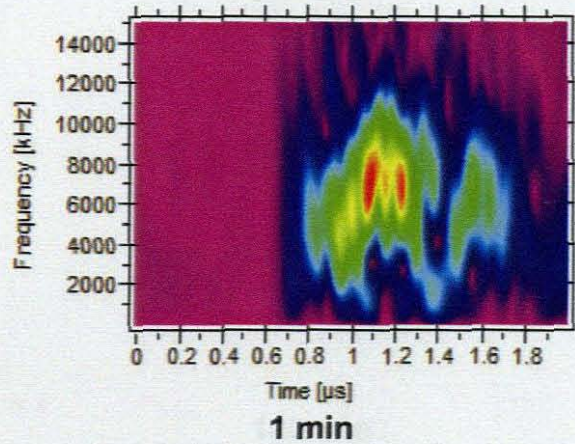
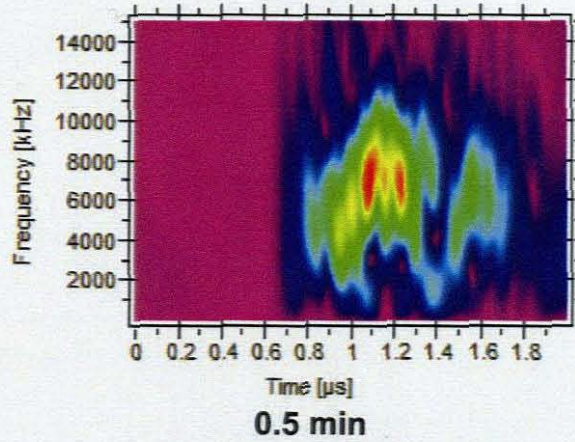
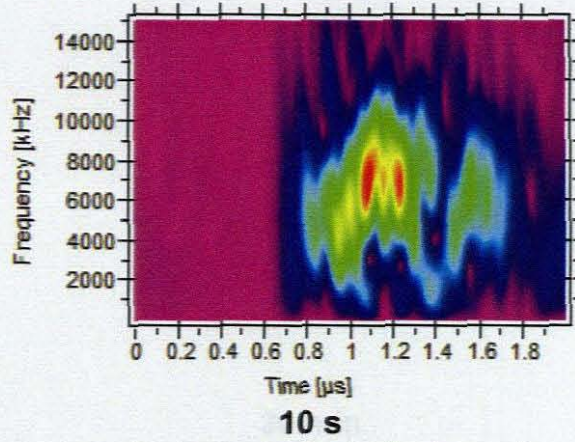
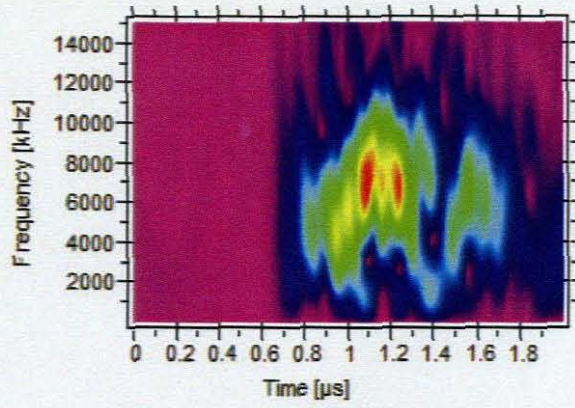
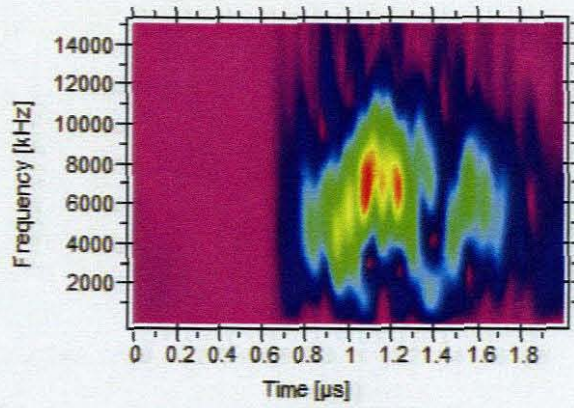
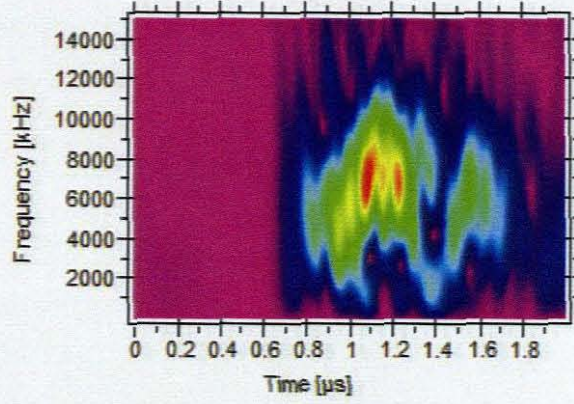


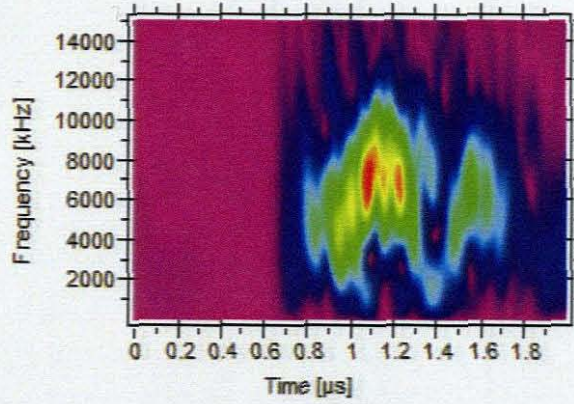
Figure 5.17: WTs of the ultrasonic signals at 0 min and after 10 s, 0.5 min and 1 min of operation ($Re = 19\,220$, cross-flow fouling experiment).



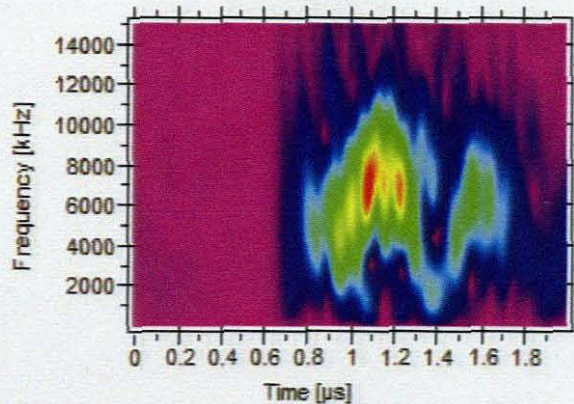
5 min



30 min



60 min



120 min

Figure 5.18: WTs of the ultrasonic signals after 5 min, 60 min and 120 min of operation ($Re = 19\ 220$, cross-flow fouling experiment).

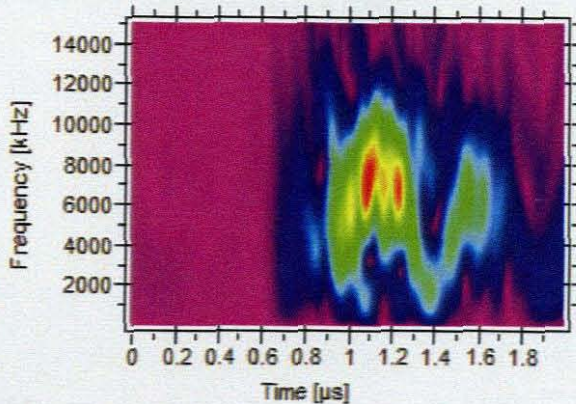
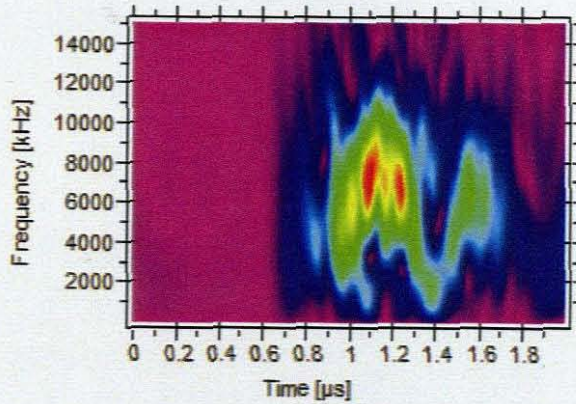
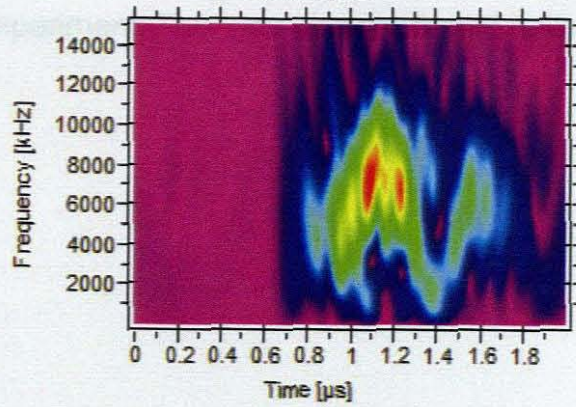
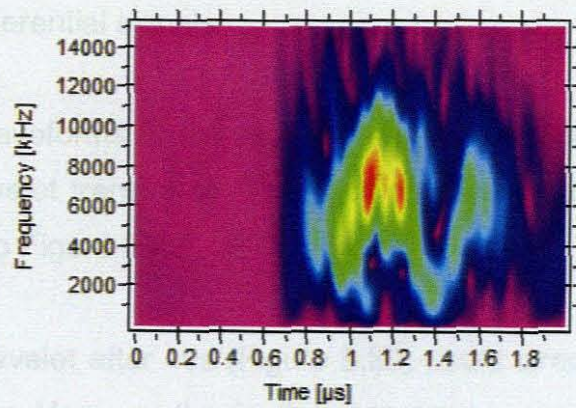


Figure 5.19: WTs of the ultrasonic signals after 360 min, 960 min and 1440 min of operation ($Re = 19\ 220$, cross-flow fouling experiment).

5.3.2.3 WTs of differential signals

The differential waveforms of the high Re cross-flow fouling experiment were analysed with wavelet transforms. These differential wavelets are presented in from Figure 5.20 to Figure 5.22.

The differential wavelet after 10s (Figure 5.20) could already show that fouling began immediately. However the fouling was not as severe as the low cross-flow velocity MF experiment. This was also confirmed by the flux decline graph.

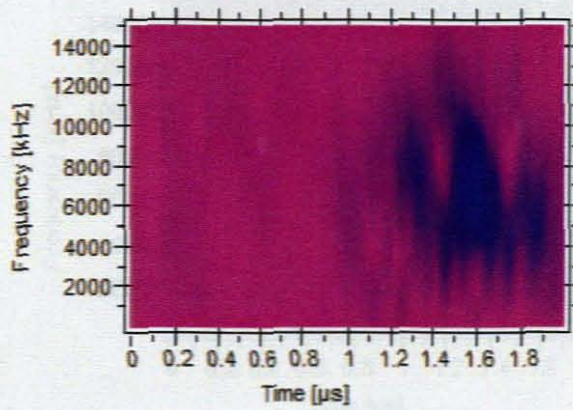
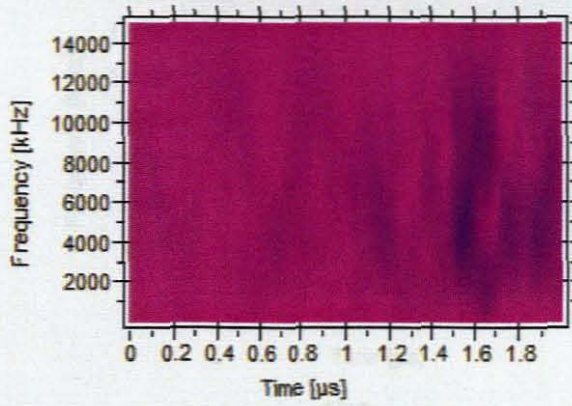
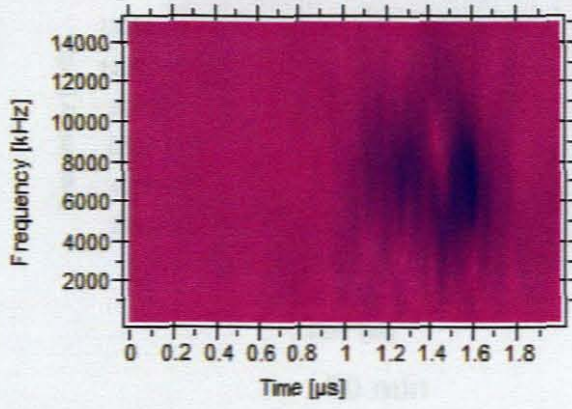
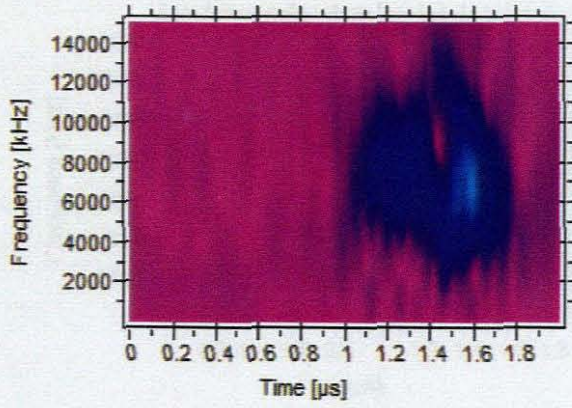
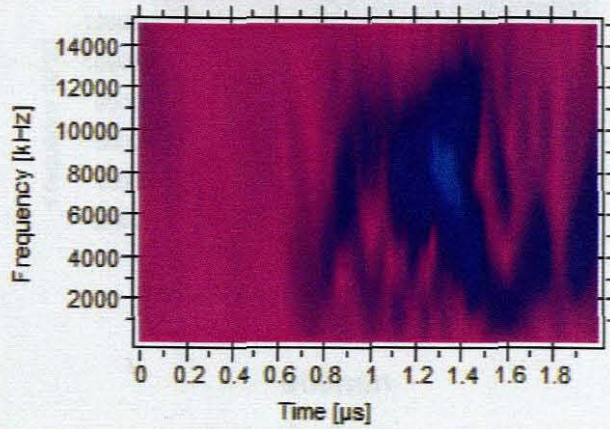


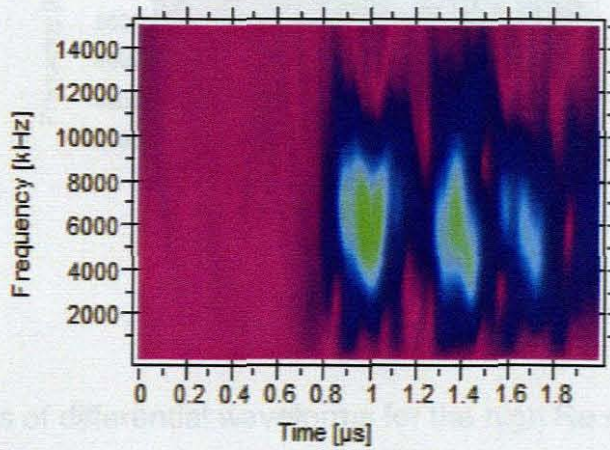
Figure 5.20: WTs of differential waveforms after 10s, 0.5 min, and 5 min of operation ($Re = 19\,220$, cross-flow fouling experiment).



30 min

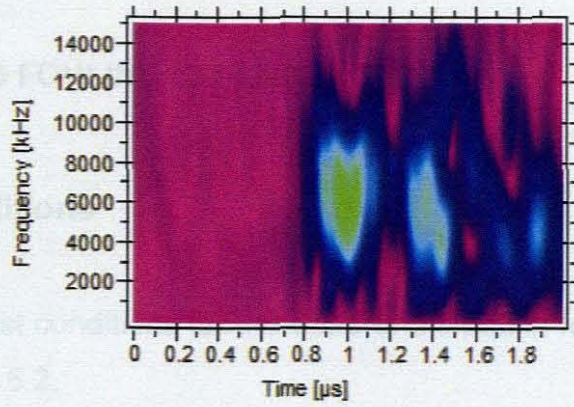


120 min

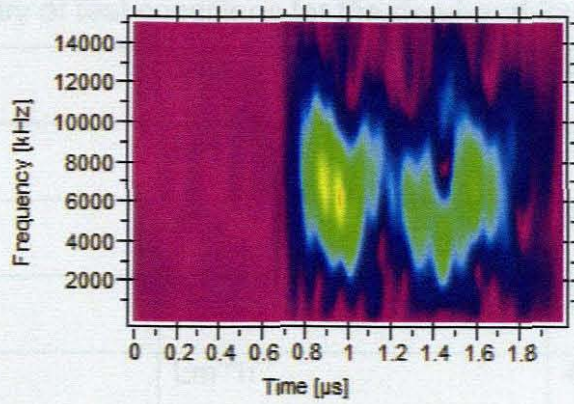


360 min

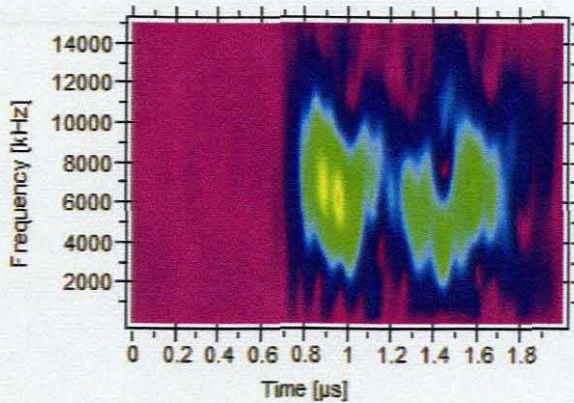
Figure 5.21: WT of differential waveforms after 30 min, 120 min, and 360 min of operation ($Re = 19\,220$, cross-flow fouling experiment).



720min



960min



1440 min

Figure 5.22: WTs of differential waveforms for the high Re cross-flow fouling experiment after 720 min, 960 min and 1440 of operation ($Re = 19\,220$, cross-flow fouling experiment).

5.4 DEAD-END FOULING EXPERIMENTS

5.4.1 Test conditions

Table 5.2 list of test conditions for the dead-end filtration fouling experiment are tabulated in Table 5.2.

Table 5.2: Summary of test conditions for the dead-end fouling experiment

Parameter	Units	Value
Feed flow-rate	L/h	25
Pressure	kPa	50
Temperature	°C	25
PWF	$\text{Lm}^{-2}\text{h}^{-1}$	445.2
Initial flux	$\text{Lm}^{-2}\text{h}^{-1}$	168.7

5.4.2 Permeate flux

5.4.3 Ultrasonic response

Figure 5.23 shows decrease in permeate flux during the microfiltration of NBW in dead-end mode. The flux declined very rapidly within the first 5 minutes of filtration. After 20 minutes of operation, the flux had fallen from $168.7 \text{ Lm}^{-2}\text{h}^{-1}$ to $96.9 \text{ Lm}^{-2}\text{h}^{-1}$. The flux decrease became more gradual after 100 minutes of operation. After 400 minutes the flux had decreased to below $20 \text{ Lm}^{-2}\text{h}^{-1}$. The filtration was stopped after 540 minutes because there was very little change in permeate volume.

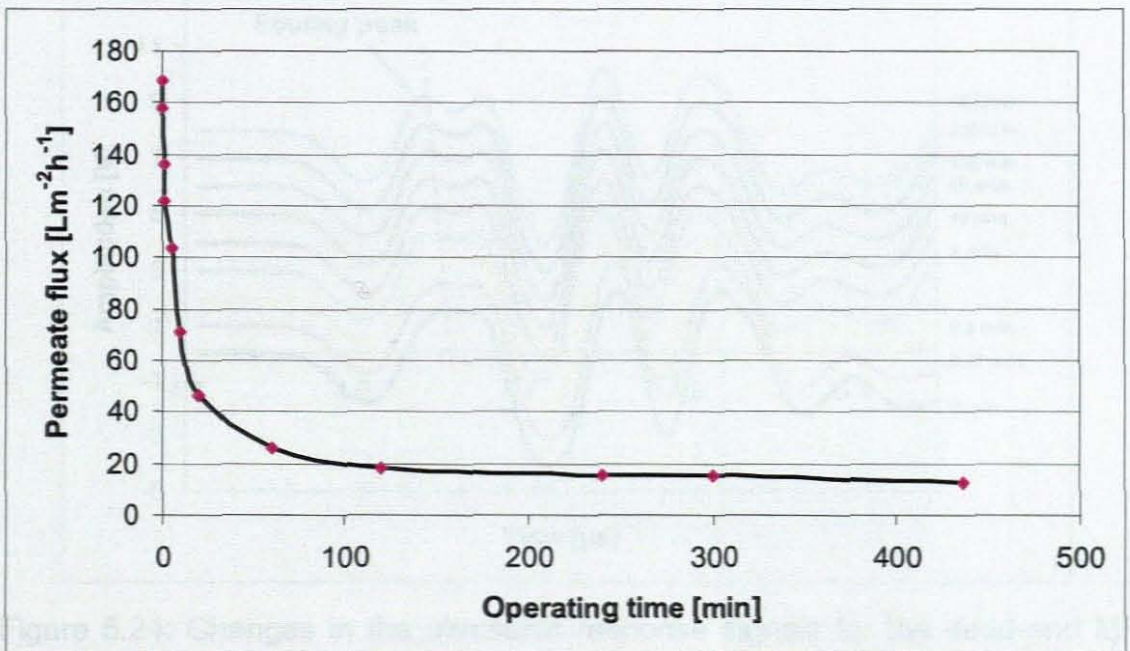


Figure 5.23: Flux decline as a time function for the dead-end fouling experiment.

5.4.3 Ultrasonic response

Ultrasonic response spectra for the dead-end fouling experiment are shown in Figure 5.23. From these waveforms it can be observed that the effects of NOM fouling were more severe than in cross-flow experiments. The fouling peak shows signs of development only after in less than 30 s of operation. After 5 minutes, the new peak is distinct from the original peak.

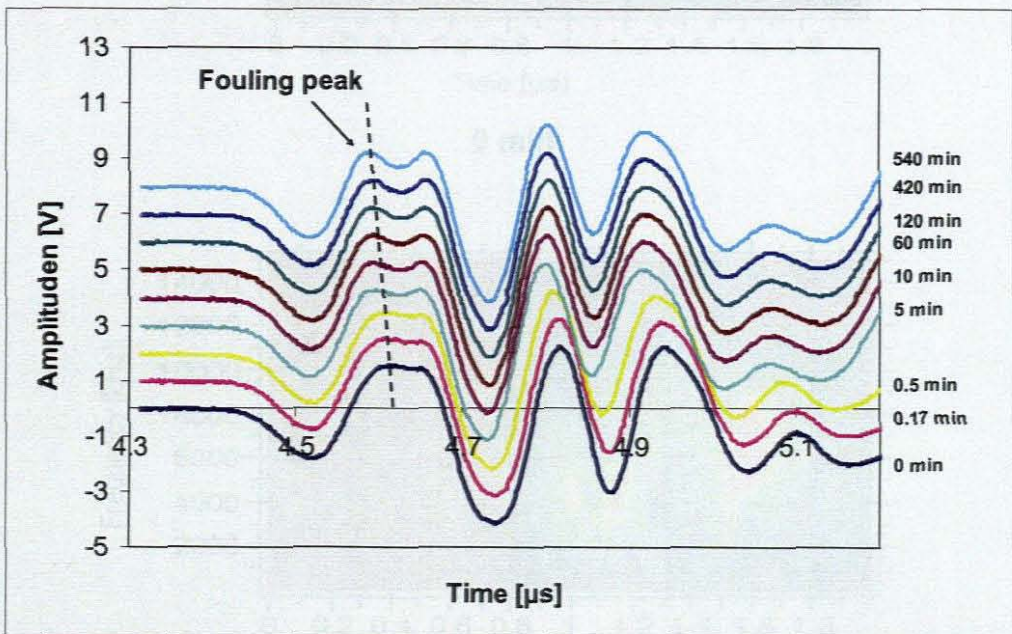
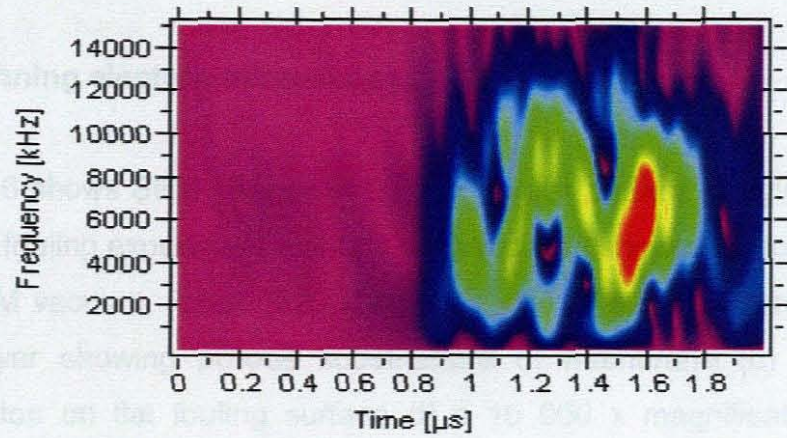


Figure 5.24: Changes in the ultrasonic response signals for the dead-end MF fouling experiment.

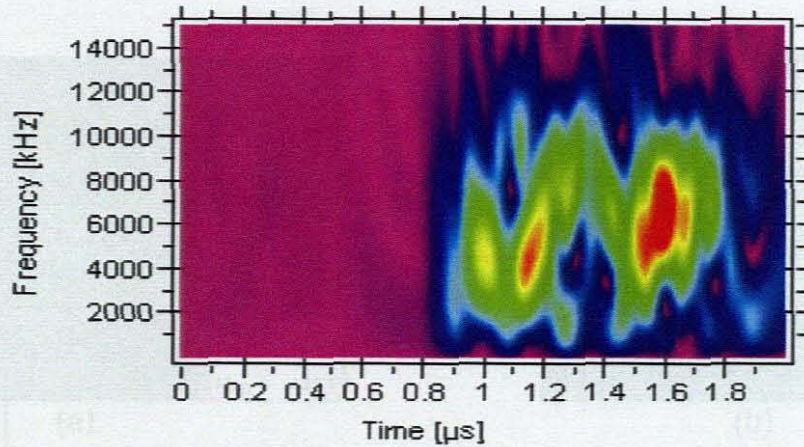
Figure 5.25: Plot of ultrasonic response signals at the start of the operation (0 min) and after 540 min of operation.

5.4.4 Wavelet transforms

Fouled membranes were removed from the reactor and analysed by scanning electron microscopy and atomic force microscopy.



0 min



540 min

Figure: 5.25: WT of ultrasonic response signals at the start of the operation (0 min) and after 540 min of operation.

5.5 CHARACTERISATION OF FOULING MEMBRANES BY MICROSCOPY

5.5.2 Atomic force microscopy

Fouled membranes were removed from the module and analysed by scanning electron microscopy and atomic force microscopy.

5.5.1 Scanning electron microscopy

Figure 5.26 shows SEM images of 0.2 μm porous surface of nylon membrane: (a) after a fouling experiment at 442 x magnification showing cracks formed due to the SEM vacuum, (b) at 6220 x magnification through a drying crack in the fouling layer showing porous substructure of membrane (c) at 14 440 x magnification on flat fouling surface (d) a 10 000 x magnification through a exposed membrane pores.

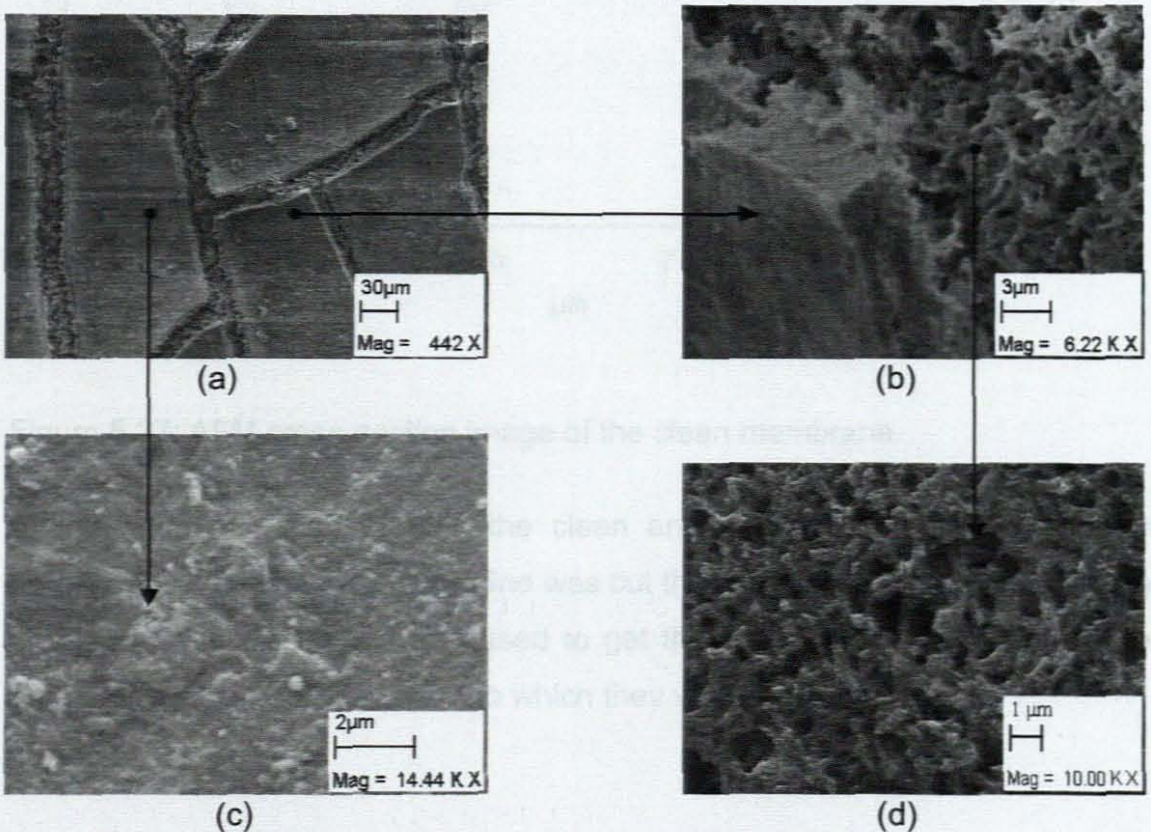


Figure 5.26: SEM images of 0.2 μm porous surface of nylon membrane after a fouling experiment: (a) 442 x magnification (b) 6220 x magnification (c) 14 440 x magnification on a fouling surface (d) 10 000 x magnification.

5.5.2 Atomic force microscopy

Results of the AFM measurements performed on a clean membrane were compared to those of the fouled membranes after the fouling experiments. Figures 5.27 and 5.28 show a cross-sectional analysis comparison of a clean and a fouled membrane.

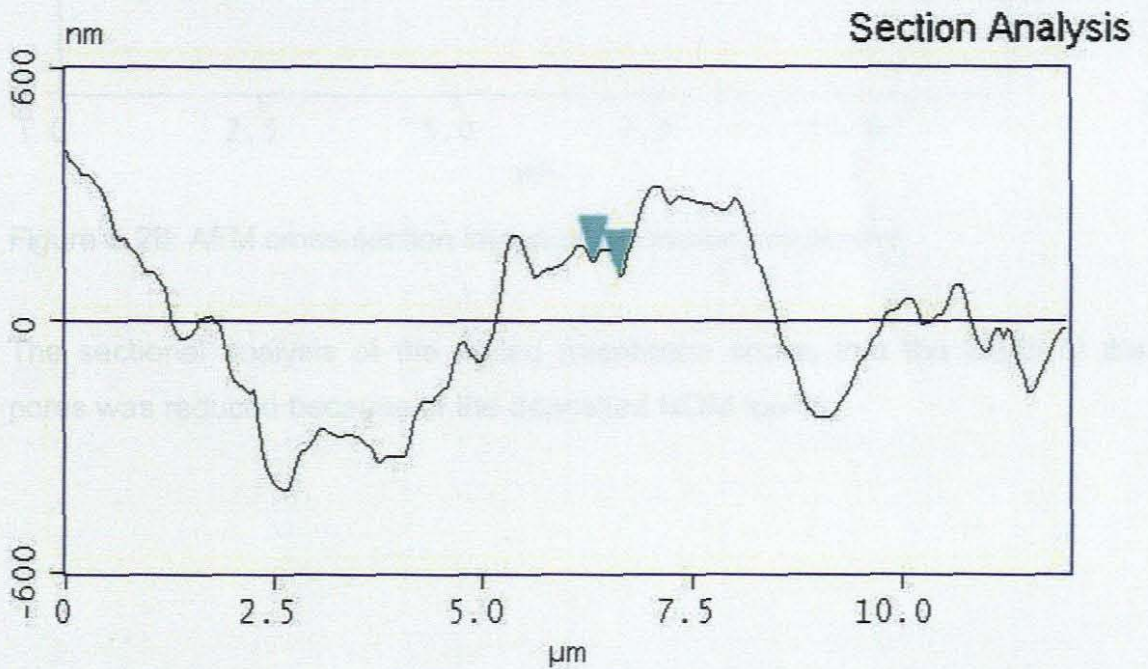


Figure 5.27: AFM cross-section image of the clean membrane.

Although the surfaces of both the clean and fouled membranes were not homogenous the cross-sectional line was cut through at random for comparison of the two. This technique was used to get the indication of the depth of the membrane pores and the extent to which they were fouled.

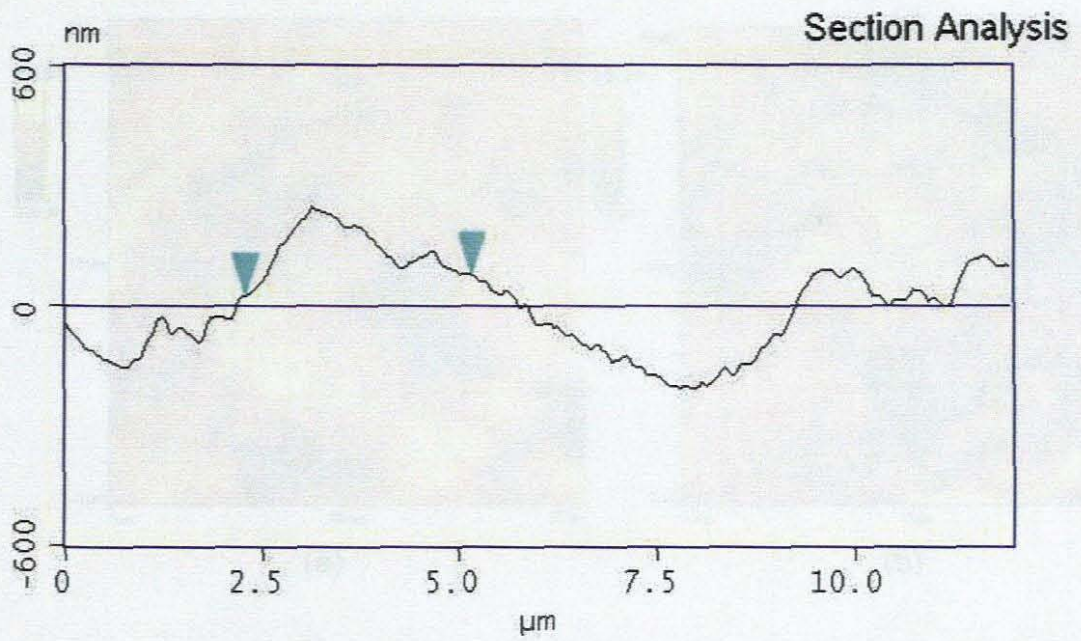


Figure 5.28: AFM cross-section image of the fouled membrane.

The sectional analysis of the fouled membrane shows that the depth of the pores was reduced because of the deposited NOM fouling.

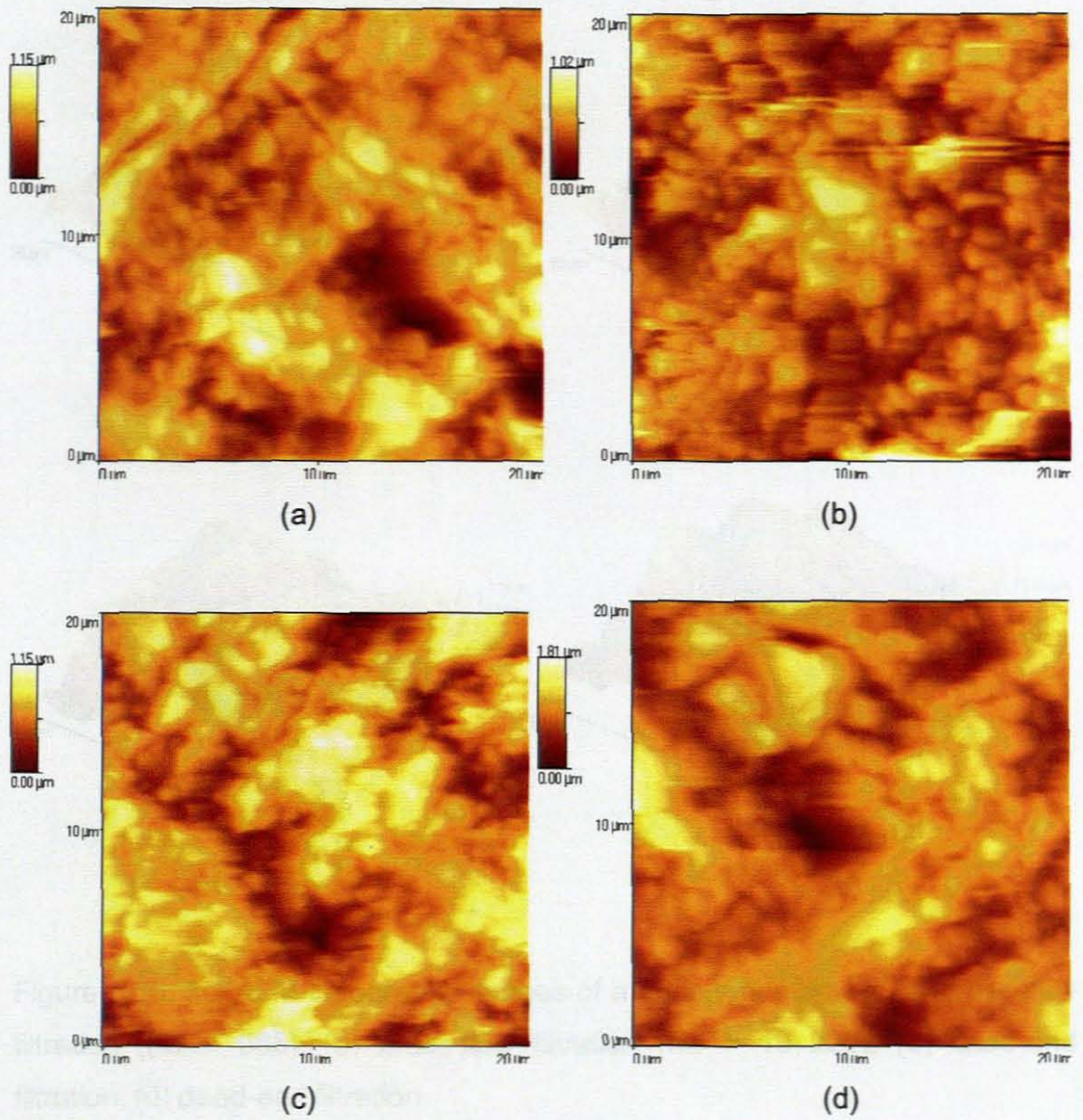


Figure 5.29 AFM Topography images of a fouled membrane: (a) cross-flow filtration ($Re = 965$), (b) cross-flow filtration ($Re = 19\ 220$), (c) dead-end filtration, (d) dead-end filtration

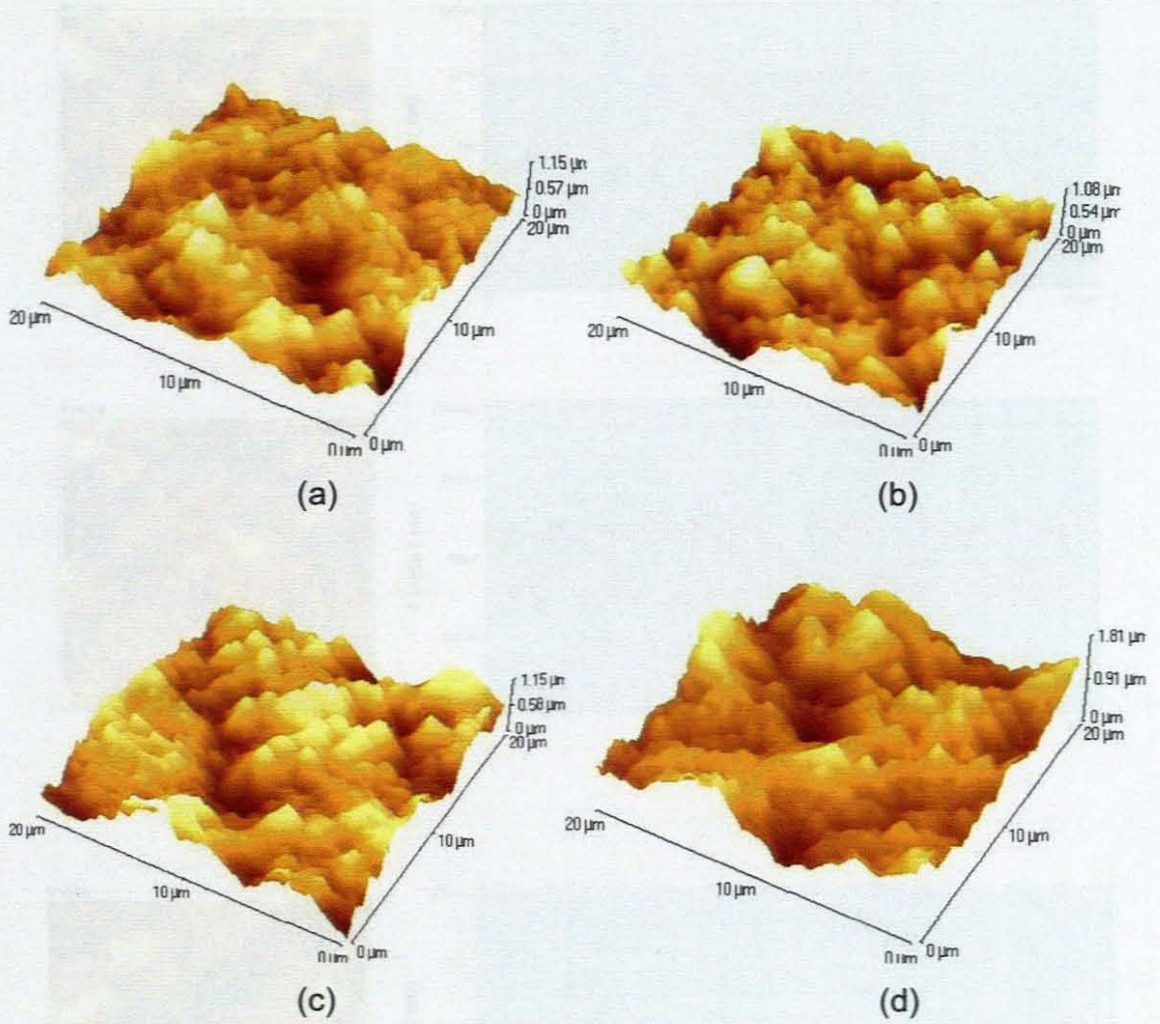


Figure 5.30: 3D AFM topography images of a fouled membrane: (a) cross-flow filtration ($Re = 965$), (b) cross-flow filtration ($Re = 19\,220$), (c) dead-end filtration, (d) dead-end filtration



Figure 5.31: Section view of AFM topography image of a fouled membrane

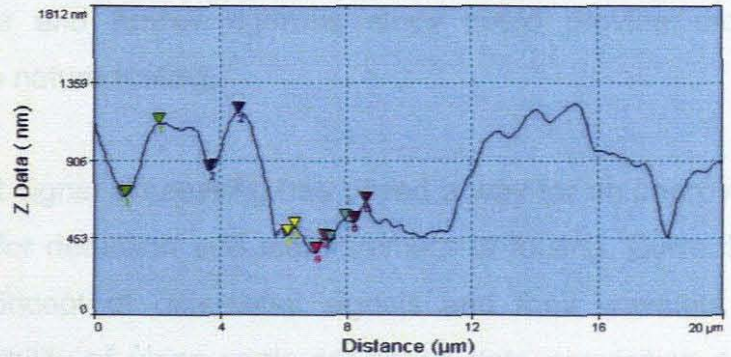
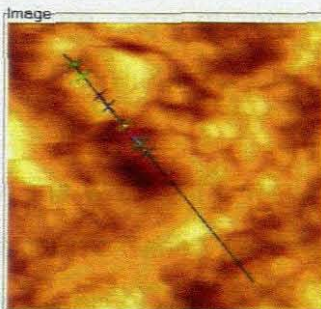
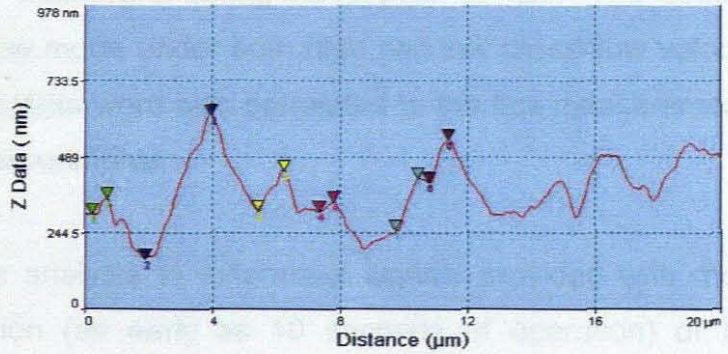
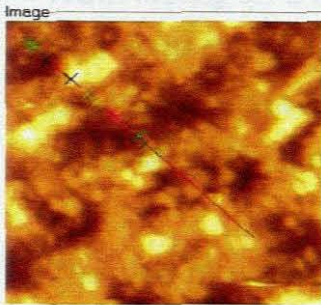
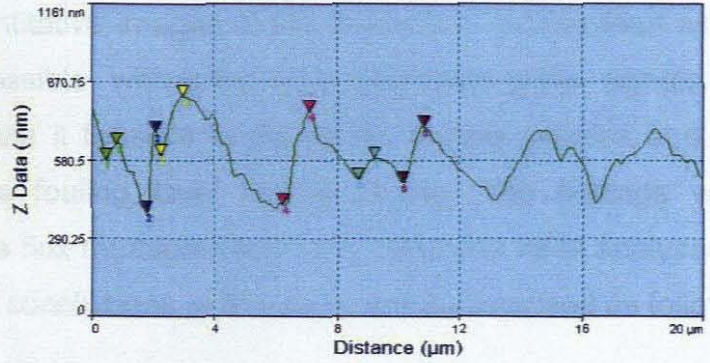
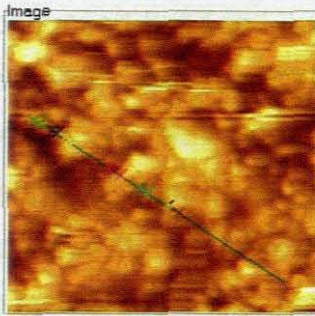
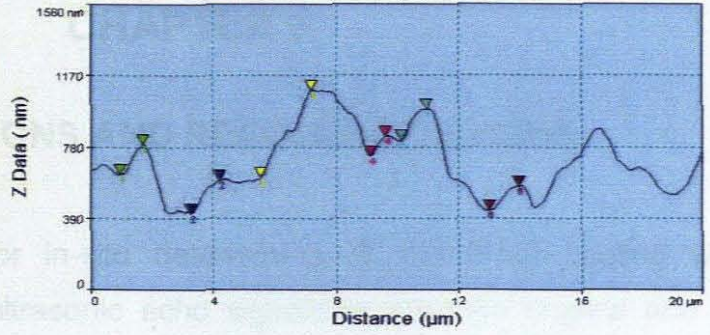
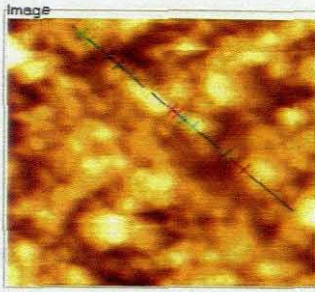


Figure 5.31: Section view on AFM topography image of a fouled membrane.

CHAPTER 6

CONCLUSIONS AND RECOMMENDATIONS

The ultrasonic signals for in-situ determining of membrane fouling were analysed using WTs of ultrasonic echo signals in both the original and the differential forms. The wavelets of differential signals showed a more pronounced but semi-quantitative images of the process of fouling than would otherwise have been possible with only time-amplitude echo signals. In addition, the wavelets make it feasible to follow the fouling process and the change in density of the fouling layer during fouling. The findings were supported by simultaneous flux measurements and SEM and AFM analyses of the membranes. The main conclusions of this study are summarised as follows:

- Ultrasonic measurement technique was used to monitor and measure NOM fouling on a MF membrane during the filtration of NBW. The filtration was done in cross-flow mode under both high and low cross-flow velocity conditions. Ultrasonic data were also correlated to the flux measurements obtained during the experiments.
- The use of wavelets analysis to differential signals provided with more immediate visualization (as early as 10 seconds of operation) of the fouling related changes. However, the results from differential wavelets are semi-quantitative and further rigorous study could provide more information about the nature fouling.

On the whole, the wavelet signal processing has paved a way for an improved ultrasonic-based method for detection and measurement of fouling. Currently, the application of the concept of differential signals and their wavelets is performed offline. A possibility of using computer-based data acquisition and signal processing in order to apply wavelets function in real-time can be investigated. The papers presented and published during this study are listed in Appendix 4.

REFERENCES

- Angrisani, L. & Daponte, P. 1997. Thin thickness measurements by means of a wavelet transform based method. *Measurement*, 20 (4): 227-242.
- Argüello, M.A., Álvarez, S., Riera, F.A. & Álvarez, R. 2003. Enzymatic cleaning of inorganic ultrafiltration membranes used for whey protein fractionation. *J. Membr. Sci.*, 216: 121-134.
- Baker, R.W. 2004. *Membrane technology and applications*. 2nd Ed. New York.: Wiley.
- Bian, R., Yamamoto, K. & Watanabe, Y. 2000. The effect of shear rate on controlling the concentration polarization and membrane fouling. *Desal.* 131: 225-23.
- Bowen, W.R., Doneva, T.A. & Yin, H.B. 2002. Separation of humic acid from a model surface water with PSU/SPEEK blend UF/NF membranes. *J. Membr. Sci.*, 206: 417-429.
- Bruce, A. & Gao, H. 1996. *Applied wavelet analysis with S-PLUS*. New York: Springer.
- Cakl, J., Bauer, I., Doleček, P. & Mikulášek, P. 2000. Effects of backflushing conditions on permeate flux in membrane cross-flow microfiltration of oil emulsion. *Desal.*, 127: 189-198.
- Carroll, T., Booker, N.A. & Meier-Haack, J. 2002. Polyelectrolyte-grafted microfiltration membranes to control fouling by natural organic matter in drinking water. *J. Membr. Sci.*, 203: 3-13.
- Cartz L. 1995. Ultrasonic Testing. In *Nondestructive Testing*. Ohio: ASM International. 81-125.

Chai, X.; Kobayashi, T. & Fujii, N. 1999. Ultrasound-associated cleaning of polymeric membranes for water treatment, *Sep. Purif. Tech.*, 15: 139-146.

Chen, V., Li, H. & Fane, A.G. 2004. Non-invasive observation of synthetic membrane processes: a review of methods. *J. Membr. Sci.*, 241 (1): 23-44.

Chona, R., Suh, C. S. & Rabroker, G. A. 2003. Characterizing defects in multi-layer materials using guided ultrasonic waves. *Optic. Laser. Eng.*, 40: 371-378.

Combe, C., Molis, E., Riley, R & Clark, M.M. 1998. The effect of CA membrane properties on adsorptive fouling by humic acid. *J. Membr. Sci.*, 154: 73-87.

Dudley, L.Y. & Darton, E.G. 1996. Membrane autopsy – a case study. *Desal.*, 105: 135-141.

Field, R.W., Wu, D., Howell, J.A. & Gupta, B.B. 1995. Critical flux concept for microfiltration fouling. *J. Membr. Sci.*, 100: 259-272.

Graps, A.L. 1995. An introduction to wavelets. *IEEE Comp. Sci. Eng.*, 2 (2): 50-61

Hoek, E.M.V., Kim, A.S. & Elimelech, M. 2002. Influence of cross-flow membrane filter geometry and shear rate on colloidal fouling in reverse osmosis and nanofiltration separations. *Env. Eng. Sci.*, 19 (6): 357-372.

Hong, S. & Elimelech, M. 1997. Chemical and physical aspects of natural organic matter (NOM) fouling of nanofiltration membranes. *J. Membr. Sci.* 132: 159-161.

Jacangelo, J. G., & Buckley, C. A. 2001. Influence of the characteristics of natural organic matter on the fouling of microfiltration membranes. *Water Res.*, 35: 4455-4463.

Jacobs, E.P., Pillay, V.L., Botes, J.P., Bradshaw, S.M., Pryor, M. & Swart, P. 2003. *Ultrafiltration capillary membrane process development for drinking water*. WRC Report No. 965/1/03

Jacobs, E.P., Pillay, V.L., Pryor, M. & Swart, P. 2000. *Water supply to rural and peri-urban communities using membrane technologies*. WRC Report No. 764/1/00

Jucker, C. & Clark, M.M. 1994. Adsorption of aquatic humic substances on hydrophobic ultrafiltration membranes. *J. Membr. Sci.*, 94: 37-52.

Li, J. & Hillis, P. 2001. Optimisation of combined coagulation and microfiltration for water treatment. *Water Res.*, 35: 2895-2904.

Kennedy, M., Kim, S., Mutenyo, I., Broens, I. & Schippers, J. 1998. Intermittent crossflushing of hollow fiber ultrafiltration system. *Desal.*, 118: 175-188.

Koen, L.J. 2000. Ultrasonic-time-domain-reflectometry as a real-time non-destructive visualization technique of concentration polarization in reverse osmosis membranes. M. Eng Thesis, University of Stellenbosch. South Africa.

Li, J. 2002. Measurement and modelling of organic fouling deposition in ultrafiltration by ultrasonic transfer signals and reflections. *Desal.*, 146: 177-185.

Li, J. & Sanderson R.D. 2002. In situ measurement of particle deposition and its removal in microfiltration by ultrasonic time-domain reflectometry. *Desal.*, 146: 169-175.

Li, J., Sanderson, R. D., Chai, G. Y., & Hallbauer, D. K. 2005. Development of an ultrasonic technique for in situ investigation of the properties of deposited protein during cross-flow ultrafiltration. *J. Coll. Int. Sci.*, 284: 228-238.

Li, J., Hallbauer, D.K. & Sanderson, R.D. 2003. Direct monitoring of membrane fouling and cleaning during ultrafiltration using a non-invasive ultrasonic technique. *J. Membr. Sci.*, 215: 33-52.

Li, J.V.Y., Hallbauer D. K. & Sanderson, R.D. 2002a. Cake-layer deposition, growth, and compressibility during microfiltration measured and modelled using a non-invasive ultrasonic technique. *Ind. Eng. Chem. Res.*, 41: 4106-4115.

Li, J., Sanderson, R.D., Hallbauer, D.K. & Hallbauer-Zadorozhnaya, V.Y. 2002b. Measurement and modeling of organic fouling deposition in ultrafiltration by ultrasonic transfer signals and reflections. *Desal.*, 146:177-185.

Li, J., Sanderson, R.D. & Jacobs, E.P. 2002c. Non-invasive visualization of the fouling of microfiltration membranes by ultrasonic time-domain reflectometry *J. Membr. Sci.*, 201: 17-29.

Li, J., Sanderson, R. D., & Jacobs, E.P. 2002d. Ultrasonic cleaning of nylon microfiltration membranes fouled by Kraft paper mill effluent. *J. Membr. Sci.* 205: 247-257.

Loy, G. 2002. Fast Computation of the Gabor Transform, *DICTA 2002: Digital Image Computing Techniques and Applications*, 21-22 January 2002, Melbourne, Australia, 6p.

Lu, X.Q., Hanna, J.V. & Johnson, W.D. 2000. Source indicators of humic substances: an elemental composition, solid state ^{13}C CP/MAS NMR and Py-GC/MS Study. *Appl. Geochem.*, 15: 1019-1033.

Maartens, A. 1998. A biological approach to foulant characterisation and cleaning. PhD Thesis. University of Stellenbosch, South Africa.

Maartens, A., Swart, P. & Jacobs, E.P. 1999. Removal of natural organic matter by ultrafiltration: characterisation, fouling and cleaning. *Wat. Sci. Tech.*, 40: 113-120.

Maartens, A., Swart, P. & Jacobs, E.P. 1998. Humic membrane foulants in natural brown water: characterization and removal. *Desal.*, 115: 215-227.

Mairal, A.P. 1998. Development of novel ultrasonic technique for real-time measurement of membrane fouling in reverse osmosis desalination. PhD thesis, University of Colorado. USA.

Mairal, A.P., Greenberg, A.R., Krantz, W.B. & Bond, L.J., 1999. Real-time measurement of inorganic fouling of RO desalination membranes using ultrasonic time-domain reflectometry. *J. Membr. Sci.*, 159: 185-196.

Mairal, A.P., Greenberg, A.R. & Krantz, W.B. 2000. Investigation of fouling cleaning using ultrasonic time-domain-reflectometry. *Desal.*, 130: 45-60.

McDonald, S., Bishop, A.G., Prenzler, P.D. & Robards K. 2004. Analytical chemistry of freshwater humic substances. *Anal. Chim. Acta*, 527 (2): 105-124.

McIntire, P. 1991. *Nondestructive Testing Handbook*, Vol. 7, 2nd Ed. American Society for Nondestructive Testing.

Meier-Haack, J., Booker, N.A. & Carroll, T. 2003. A permeability-controlled microfiltration membrane for reduced fouling in drinking water treatment. *Water Res.*, 37: 585-588.

Mulder, M. 1991. *Basic Principles of Membrane Technology*. Dordrecht: Kluwer Academic Publishers. 281.

Peterson, R.A., Greenberg, A.R., Bond, L.J. & Krantz, W.B. 1998. Use of ultrasonic TDR for real-time non-invasive measurement of compressive strain during membrane compaction. *Desal.*, 116: 115-122.

Reinsch, V.E., Greenberg, A.R., Kelley, S.S. Peterson, R & Bond L.J. 2000. A new technique for the simultaneous, real-time measurement of membrane

compaction and performance during exposure to high-pressure gas. *J. Membr. Sci.*, 171: 217–228.

Roland-Mieszkowski, M. & Young, W.R. 1991. Consequences of Nyquist theorem for acoustic signals stored in digital format, *Proceedings of CAA Conference*, Edmonton, Alberta, Canada, 7-10 October.

Sanderson R.D., Hallbauer D.K. & Li, J. 2004. Detecting the first onsets of bio-fouling on membrane filters using ultrasonic NDT and wavelet transform of signals. 1st National NDT Symposium, Pretoria, South Africa.

Sanderson, R.D., Hallbauer D.K., Li, J., Hallbauer-Zadorozhnaya V.Y., Marke, S. & Schiller, J. 2002. Flat bed type slave unit for the detection and monitoring of fouling of membranes used in liquid separation processes. SA Provisional Patent: SA 2002/4753.

Schäfer, A.I. 2001 *Natural organics removal using membranes: Principles, performance and cost*. Lancaster: Technomic.

Schäfer, A.I., Fane, A.G. & Waite, T.D. 2000a. Fouling effects on rejection in the membrane filtration of natural waters. *Desal.*, 131: 215-224.

Schäfer, A.I., Fane, A.G. & Waite, T.D. 2000b. Cost factors and chemical pretreatment effects in the membrane filtration of waters containing natural organic matter. *Water Res.*, 35: 1509-1517.

Schäfer, A.I., Schwicker, M.M. Fane, A.G. & Waite, T.D. 2000c. Microfiltration of colloids and natural organic matter. *J. Membr. Sci.*, 171: 151-172.

Scott, K. 1996. *Handbook of industrial membranes*. Oxford: Elsevier. 240.

Seidel, A. & Elimelech, M. 2002. Coupling between chemical and physical aspects of natural organic matter (NOM) fouling of nanofiltration membranes: implications for fouling control. *J. Membr. Sci.*, 203: 245-255.

Shetty, G.R. & Chellam, S. 2003. Predicting membrane fouling during municipal drinking water nanofiltration using artificial neural networks. *J. Membr. Sci.*, 217: 69-86.

Shon, H.K., Vigneswaran, S., Kim, I.S., Cho, J. & Ngo, H.H. 2004. Effect of pretreatment on the fouling of membranes: application in biologically treated sewage effluent. *J. Membr. Sci.*, 234: 111-120.

Suzuki H., Kinjo T., Hayashi Y., Takemoto M., Ono K., 1996. Wavelet Transform of Acoustic Emission Signals. *J. Acous. Emiss.* 14 (2): 69-84.

Swart, P., Maartens, A., Engelbrecht, J., Allie, Z. & Jacobs, E.P. 1998. *The development and implementation of biological cleaning techniques for ultrafiltration and reverse osmosis membranes fouled by organic substances.* WRC Report No 660/1/99.

Swartz, C.D. & De Villiers, H.A. 1998. *Guidelines for the treatment of Cape coloured waters.* WRC Report No 534/1/98.

Takemoto M., Nishino H. & Ono K. 2000. Wavelet Transform - Applications to AE Signal Analysis. *Acoustic Emission - Beyond the Millenium*, Elsevier: 35-56.

Thurman, E.M., Wershaw, R.L. Malcolm, R.L. & Pinckney, D.J. 1982. Molecular size of aquatic humic substances. *Organ. Geochem.* 4 (1): 27-35.

Tsujimoto, W., Kimura, H & Ono, K. 2000. Wavelet Transform – Applications to AE Signal Analysis. *Acoustic Emission – Beyond the Millennium*, Elsevier: 35-56.

Tsujimoto, W., Kimura, H., Izu, T. & Irie, T. 1998. Membrane filtration and pre-treatment by GAC. *Desal.*, 119: 323-326.

Wang, Z., Pant, B.C. & Langford, C.H. 1990. Spectroscopic and structural characterization of a Laurentian fulvic acid: notes on the origin of the color. *Anal. Chim. Acta*, 232: 43-49.

Yuan, W. & Zydney, A.L. 1999. Effects of solution environment on humic acid fouling during microfiltration. *Desal.*, 122: 63-76.

APPENDIX 1

ULTRASONIC FOULING/PLUGGING INDEX METER

The UFPIM is an instrument that was developed in a joint collaboration between the Department of Chemistry and Polymer Science, University of Stellenbosch (Stellenbosch, South Africa) and IfU GmbH (Lichtenau, Germany). This work was funded by the Water Research Commission of South Africa (WRC) under the framework of Project K5/1441. The idea of the UFPIM was established to help in the mitigation of membrane fouling. The concept of the instrument is the measurement and monitoring of membrane fouling using the ultrasonic technique to achieve the following:

- To check fouling potential of raw water/effluent for membrane treatment or pretreatment.
- To be used as a slave cell for large membrane plants (monitor and control cleaning regimes). The instrument is designed to be installed parallel to existing membrane plants for the purpose of monitoring membrane fouling.
- To help develop preventive methods.



Figure A1.1: A photograph of the UFPIM.

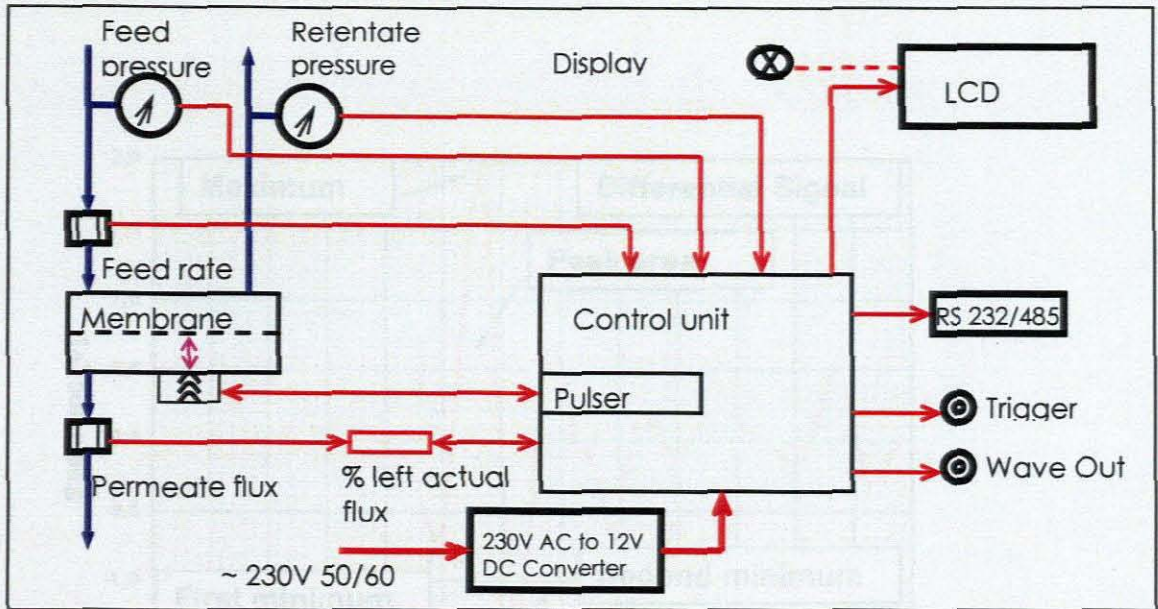


Figure A1.2: Schematic presentation of the operation of UFPIIM.

The algorithm of operation is summarised as follows:

- Calibration / reference measurement
- Form differential signal/data
- Determine minimum of differential signal
- Identify peak position of fouling signal
- Calculate peak area
- Obtain data on actual flow
- Smoothing of values
- Display value on LCD

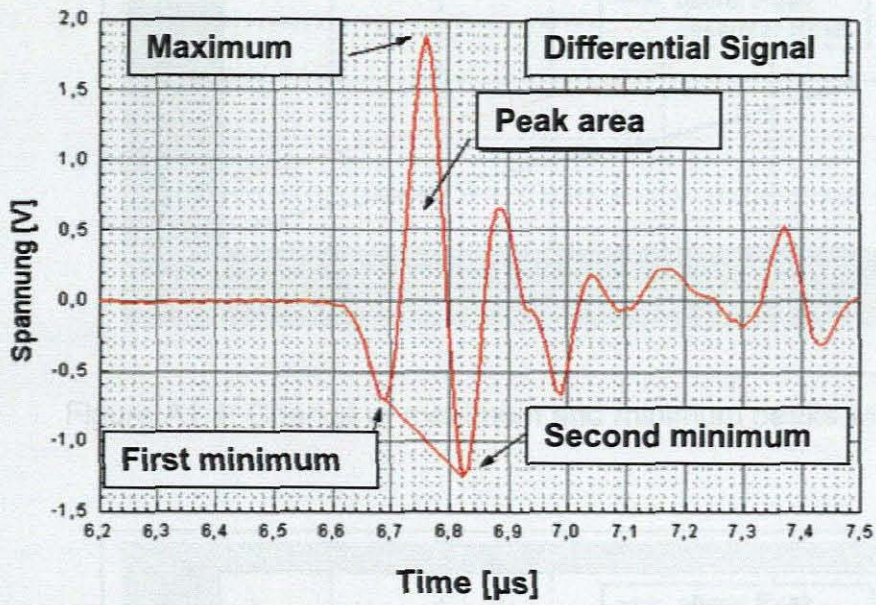


Figure A1.3: Differential signal from the UFPIM.

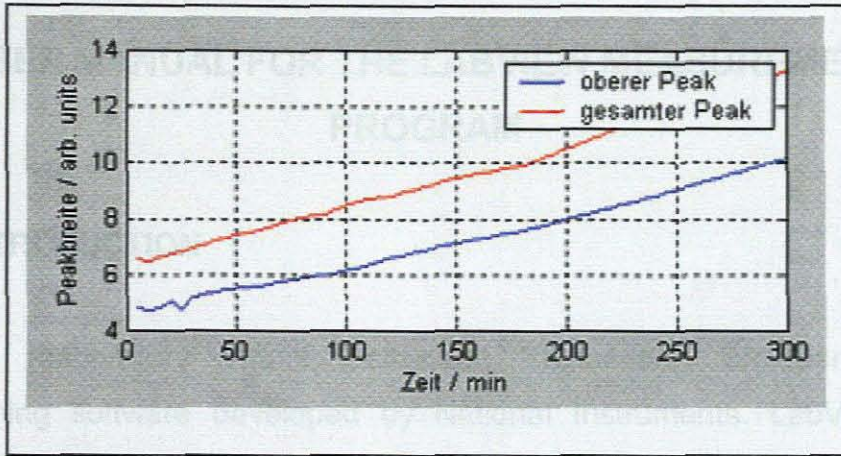


Figure A1.4: Change of maximum and minimum peaks with time.

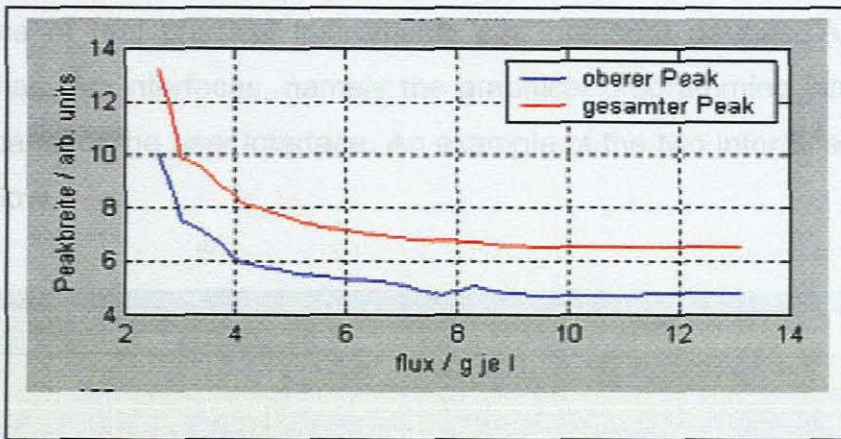


Figure A1.5: Change of maximum and minimum peaks with flux.

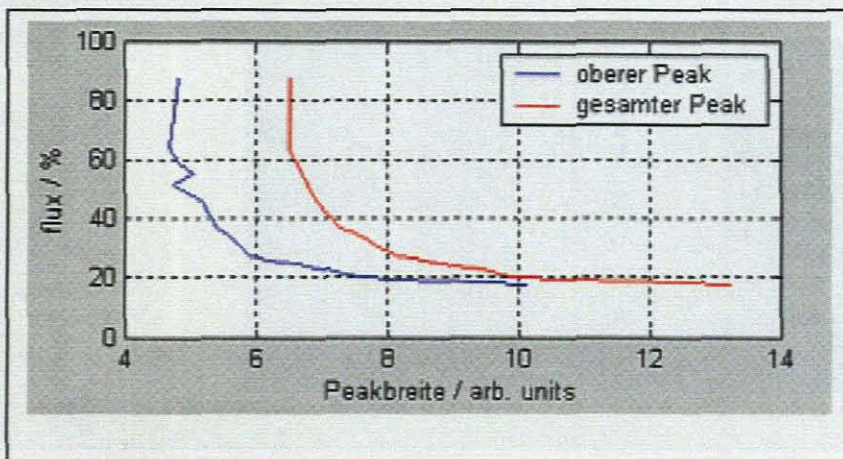


Figure A1.6: Change of percentage flux with change in peak area.

APPENDIX 2

USER MANUAL FOR THE LABVIEW MEASUREMENT PROGRAM

A2. 1. INTRODUCTION

LabVIEW (Laboratory Virtual Instrument Engineering Workbench) is a programming software developed by National Instruments. LabVIEW uses graphical programming language instead of text language to write measurement control programs. The programs created using LabVIEW (called virtual instruments or VI's) are designed to function like and have an appearance of real physical instruments e.g. pressure gauges. A LabVIEW program has two interfaces, namely the graphical programming interface and the front panel or the user interface. An example of the two interfaces of a VI is shown below.

Figure A2.1: LabVIEW programming (block diagram) interface showing

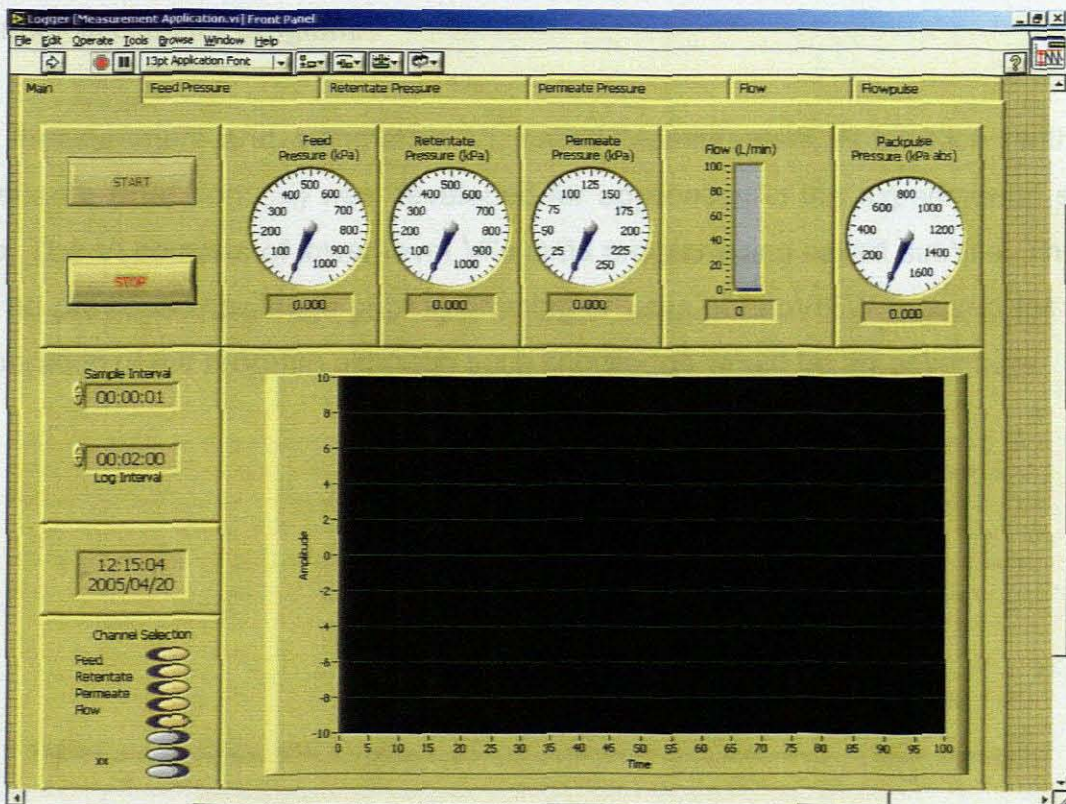


Figure A2.1: User interface of the measurement program designed with LabVIEW.

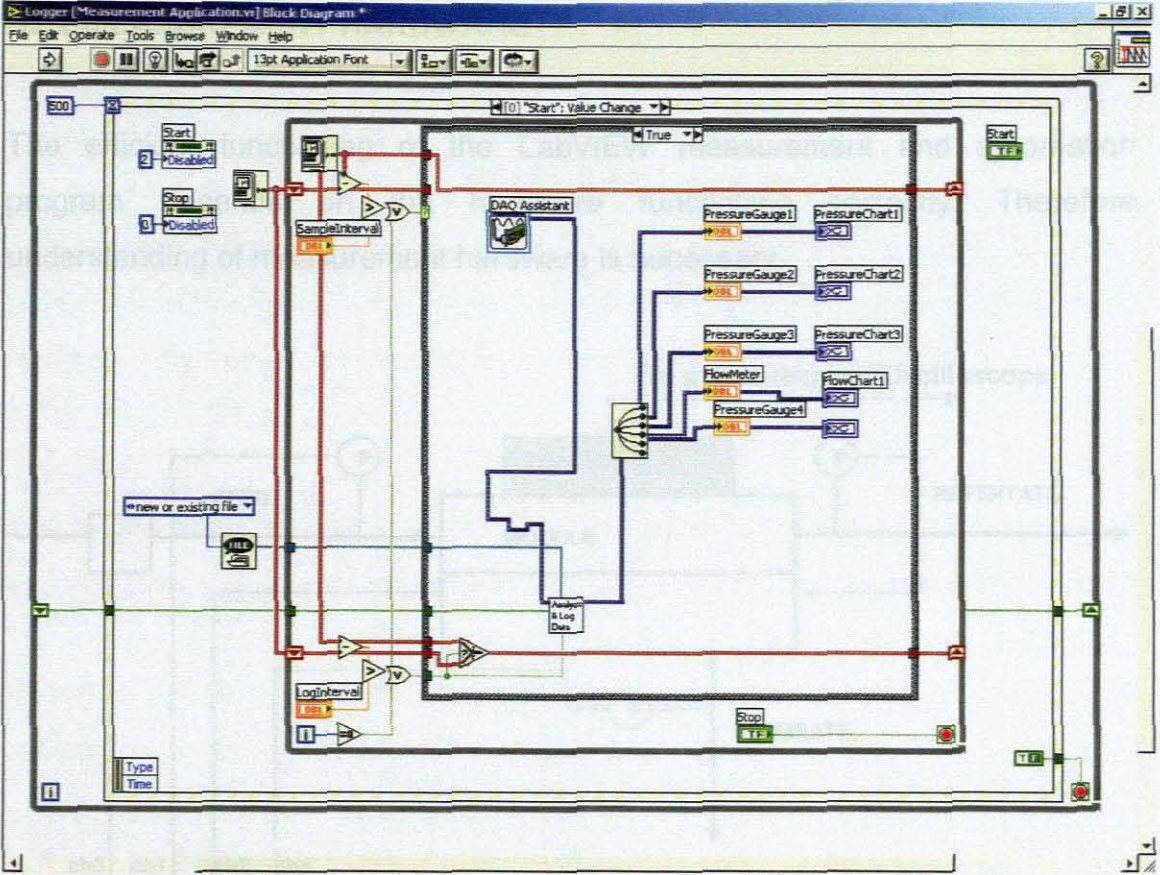


Figure A2.2: LabVIEW programming (block diagram) interface showing graphical code for program.

A measurement and automation VI, called Measurement Application (with a filename extension: .vi) was developed for application in the experimental set-up. The VI consists of lower level VI's in its programming called subVI's. There is no previous knowledge of programming or uses of LabVIEW required for the operation of the program although such knowledge would be an advantage.

A2.2 MEASUREMENT HARDWARE

The efficient functioning of the LabVIEW measurement and automation program depends on the hardware functioning correctly. Therefore understanding of measurement hardware is necessary.

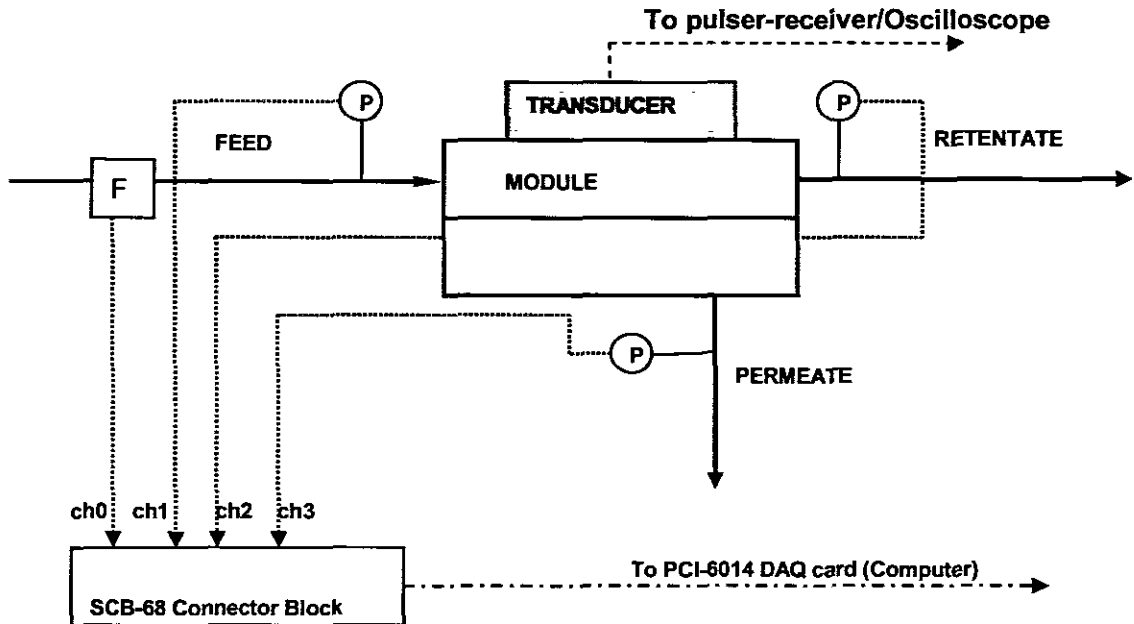


Figure A2.3: Schematic representation of the measurement hardware in the experimental set-up.

The set-up consists of the filtration and pulsing system, pressure and flow sensors, the data acquisition interface and the computer (and software).

The filtration and pulsing filtration part of the set-up consists of a filtration cell with its flow tubes, as shown in the schematic in Figure A2.3. The system consists of four pressure sensors and a magnetic flow sensor (WIKA Instruments, Milnerton). The pressure sensors use piezo-electrical elements to convert between physical changes and electrical signals, while the flow sensor uses principle of the principle of magnetic resonance for measurement. All these sensors have analog current output of between of 4 and 20 mA

(milliamperes) and have a power supply of 24 V DC, from an IQ 1000 power supply (IQ Instruments, Randburg). This power supply is used to invert energy from a 230V AC source.

The pressure meters for measuring the feed and retentate pressures have the measurement range of 0 to 10 bar (0 to 1000 kPa) gauge pressure. The range measured by the permeate pressure meter is between 0 and 2.5 bar (0 to 250 kPa) gauge pressure.

The sensors are connected to a SCB-68 shielded connector accessory, which is connected to a computer-installed 16-bit NI PCI-6014 data acquisition card via a 1-metre SH68-68-EP 68-pin cable. The NI PCI-6014 card creates an interface of communication between the sensors and the measurement software.

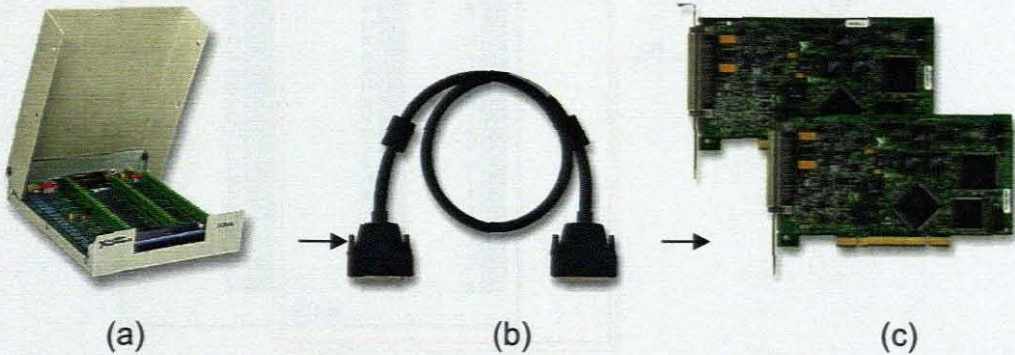


Figure A2.4: Components of the data acquisition interface consisting of (a) SCB-68 connector block, (b) SH68-68-EP 64 pin cable and (c) NI PCI-6014 data acquisition (digitising) card.

The four diagrams in Figures A2.5 to A2.8 show the connection diagrams for the signal input from the sensors. The circle with an upward arrow represents the signal source (sensor) and zigzag lines (labelled R) represent the resistors across which the signal cables are connected.

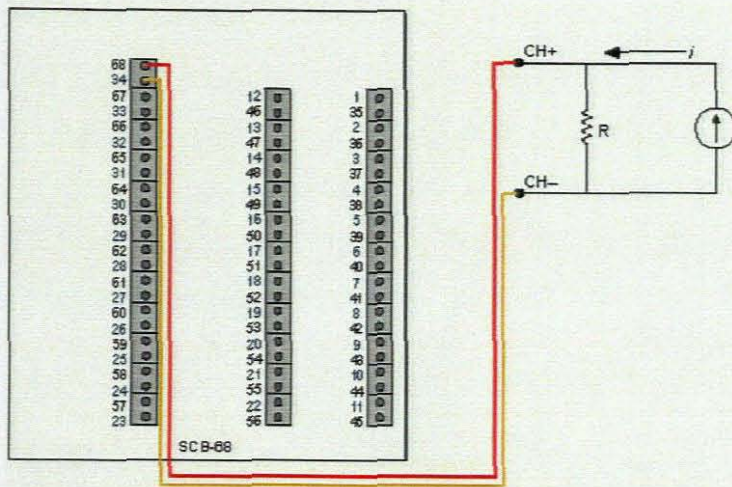


Figure A2.5: Connection diagram for the feed pressure measurement on AICH0 (ACH0-ACH8).

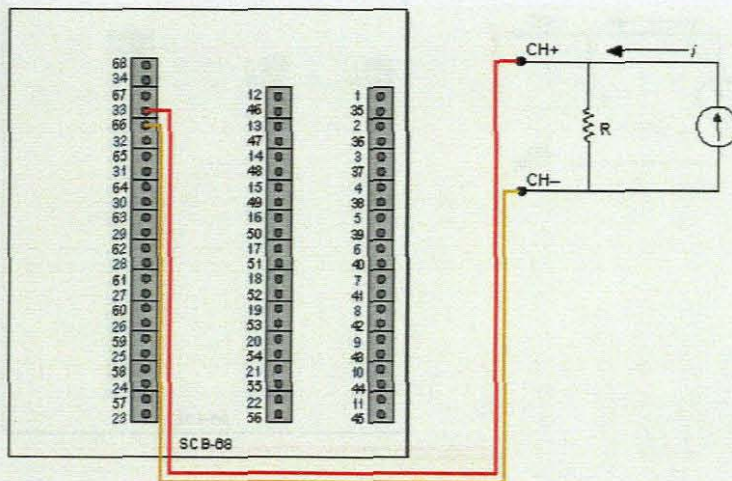


Figure A2.6: Connection diagram for the retentate pressure measurement on AICH1 (ACH1-ACH9).

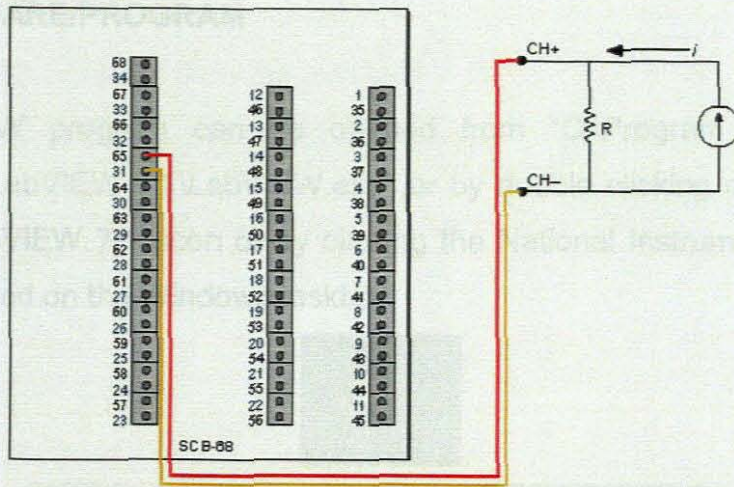


Figure A2.7: Connection diagram for the permeate pressure measurement on AICH2 (ACH2-ACH10).

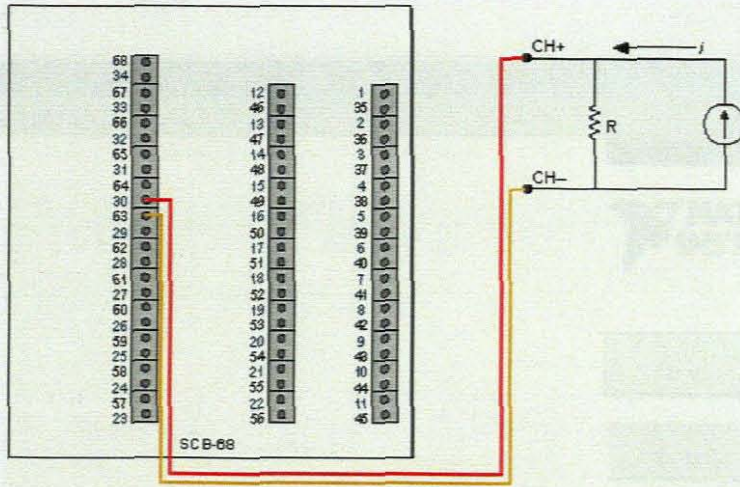


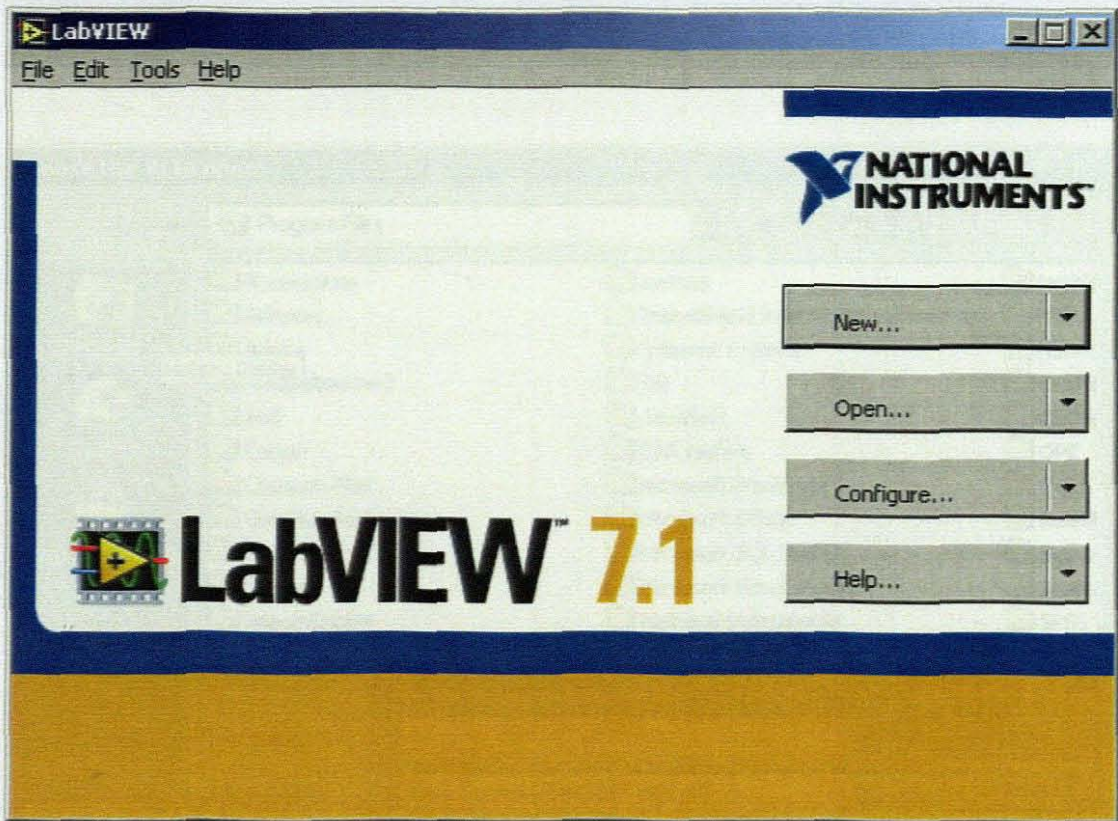
Figure A2.8: Connection diagram for the flow measurement on AICH3 (ACH3-ACH11).

A2.3 SOFTWARE/PROGRAM

The LabVIEW program can be opened from "C:\Program Files\National Instruments\LabVIEW 7.1\LabVIEW.exe" or by double clicking on the desktop shortcut "LabVIEW 7.1" icon or by clicking the National Instruments LabVIEW 7.1 icon located on the Windows taskbar.

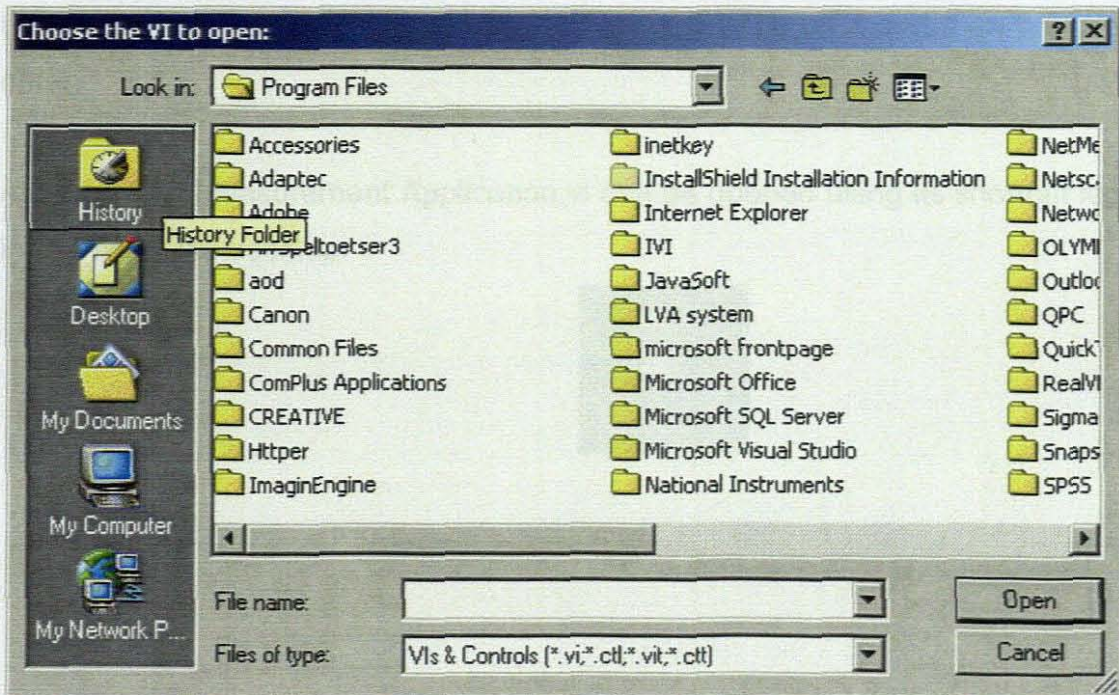
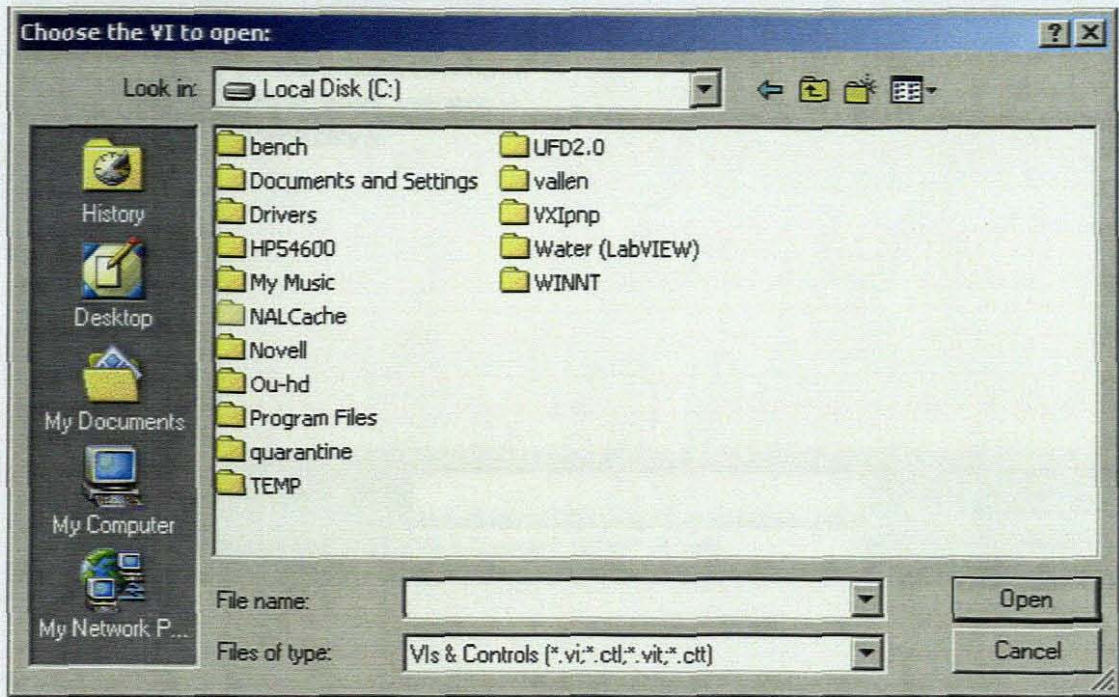


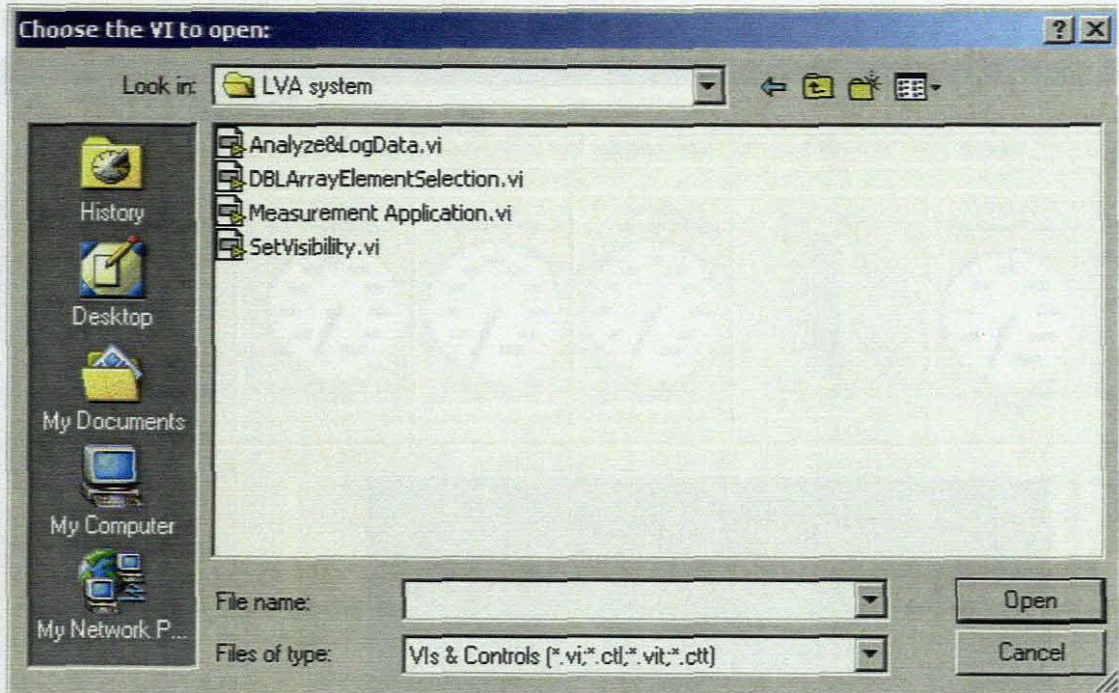
When LabVIEW has loaded and is ready, a LabVIEW dialog box will appear as shown below:



A 'Choose VI to open' dialog box can then be opened by clicking the 'Open' button on the LabVIEW dialog box. Then Measurement Application.vi file, which is the VI used for the measurement and automation system can be opened

from its directory, c:\Program files\LVA System. The dialog boxes below illustrate how this directory can be reached:



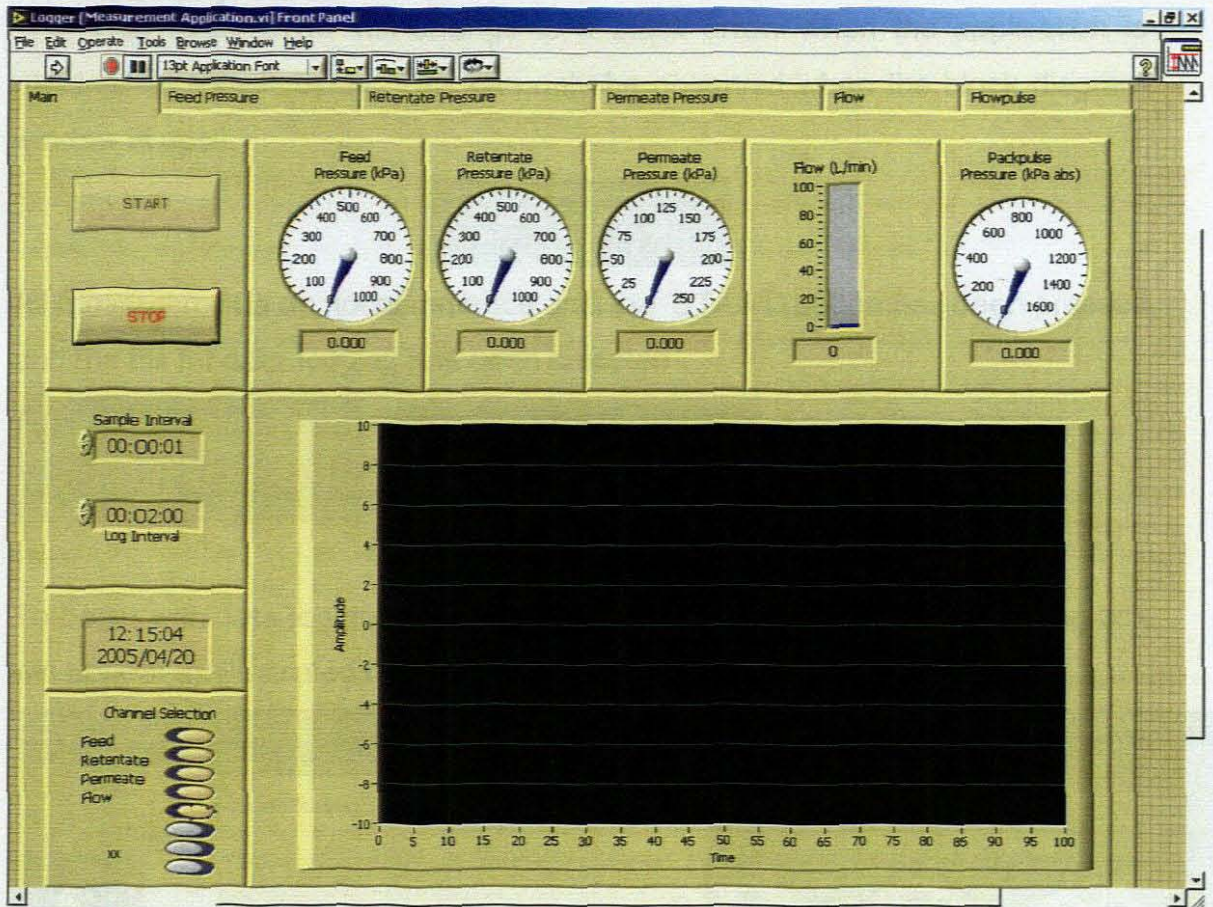


When the file directory has been located the Measurement Application.vi can be opened by double-clicking on it or by clicking once on it and then pressing enter.

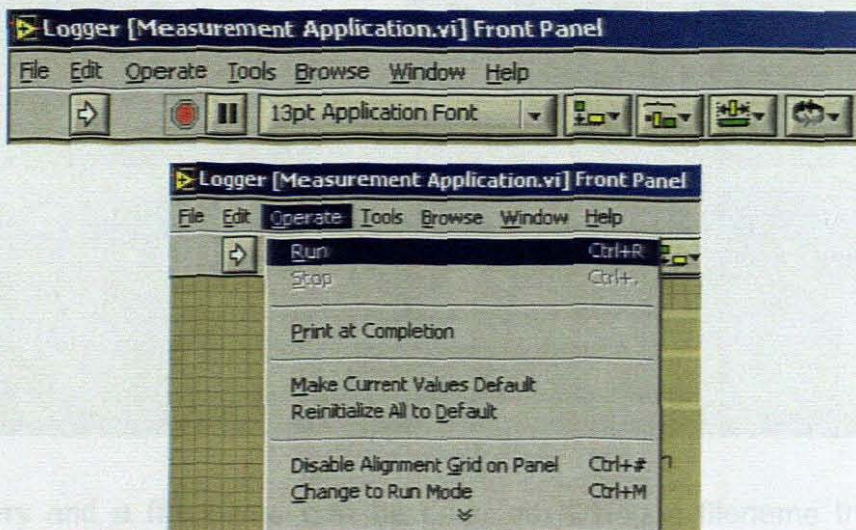
Alternatively, Measurement Application.vi can be opened using its shortcut icon in the Windows desktop.



The program will load and appear as below:



To begin running the program a run button (solid white arrow as shown below) can be selected. Alternatively, the run option can be selected from 'Operate' menu.



Pressing Ctrl and R keys on the keyboard simultaneously will also run the VI.

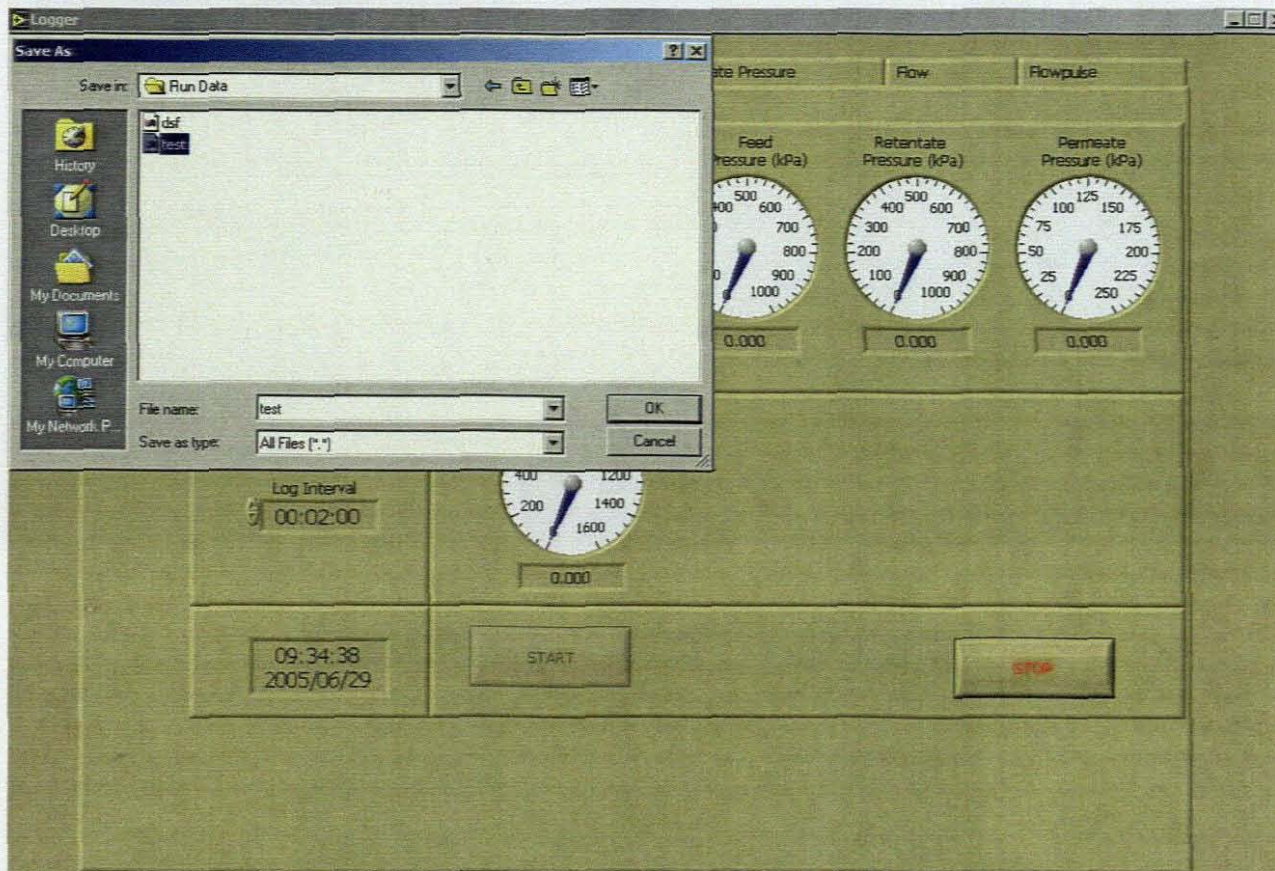
The solid white arrow will change to a black arrow when the application is running, as shown below. This can only be observed when the block diagram window is open.



All measurements do not commence until the 'START' button has been pressed and the file for data logging has been selected.



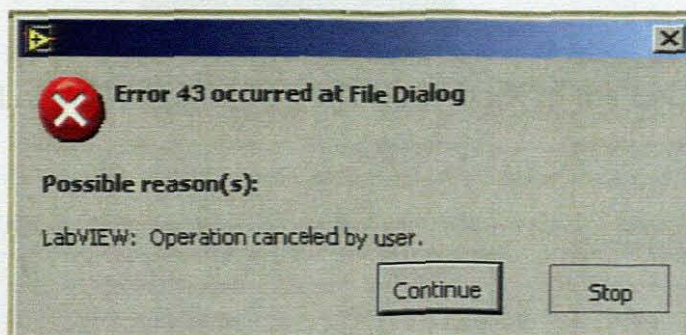
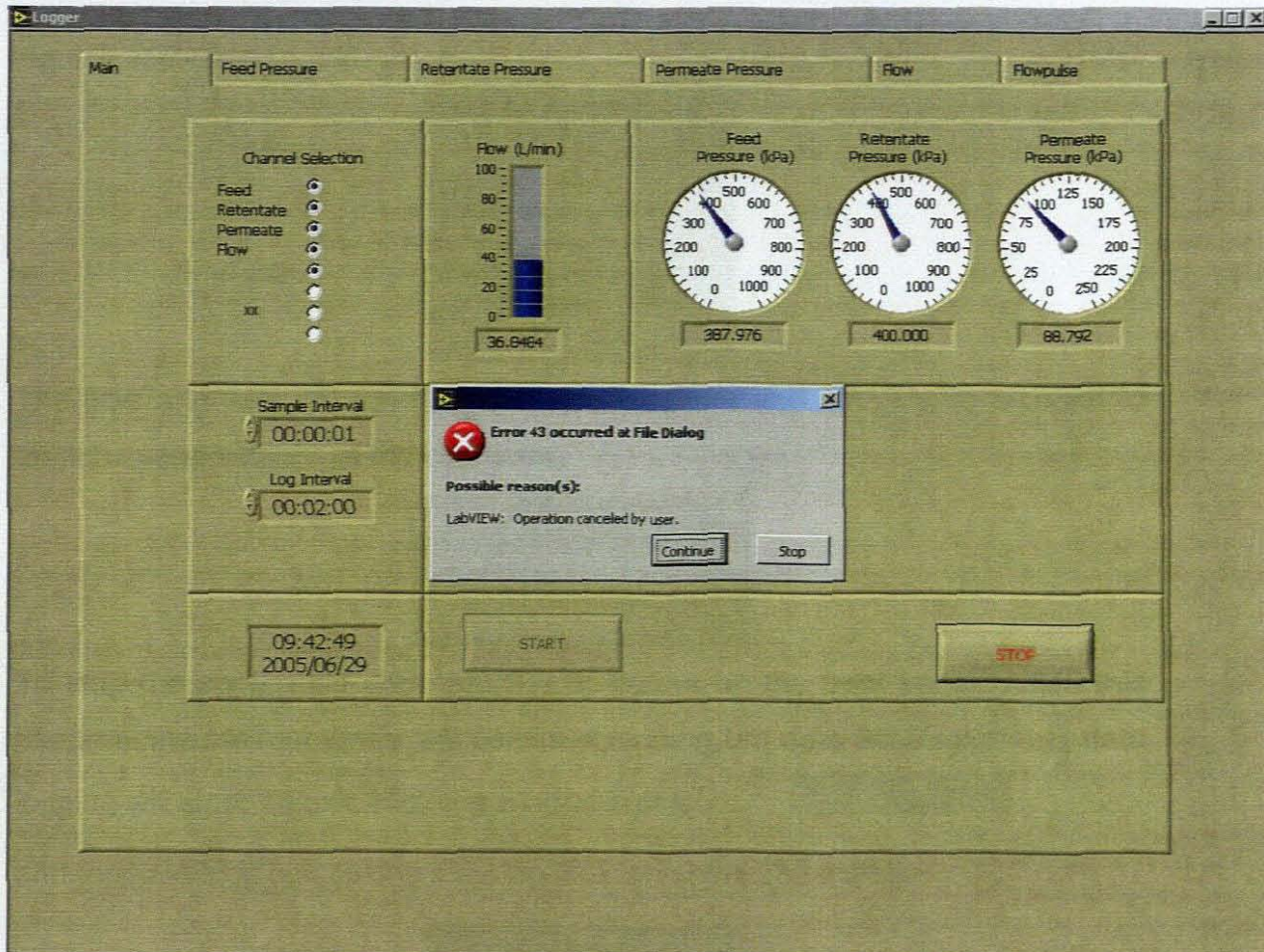
To begin with data logging press the 'START' button. The 'Save As' dialog box will appear as illustrated below:



A directory and a file name can be selected. Using a filename that already exists will result in the file being overwritten by the new one. There is a warning message for this. It is important to ensure that the previous data are backed-up as accidental losses may occur.

After the directory and the file name have been selected, press 'Save' on the 'Save As' dialog box or press Enter on the keyboard to begin measurements.

If 'Cancel' has been selected on the 'Save As' dialog box, then an error message will appear as shown:



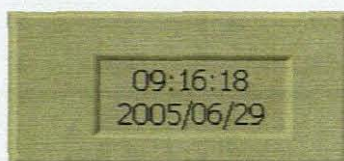
Choose to 'Continue' to return to the 'Save As' dialog box or 'Stop' to terminate or stop the running application.




The sampling interval and the data logging interval can be controlled from the time control buttons shown below:

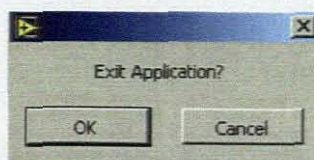


The time and date will run from the time indicator and will only correspond to the time and date settings of the computer.



To stop the application click the 'STOP' button on the front panel. When this happens the main program will continue running but data acquisition and data logging will stop. To exit, click the window exit icon 

and then a dialog box asking if the application should be exited.



Click 'Ok' and the LabVIEW application will close back to the LabVIEW dialog box.

APPENDIX 3

Summary of preliminary ultrasonic results

The following spectra (Figure A2.1-A2.5) were obtained from the filtration module under different conditions. A 10 MHz transducer was used in these tests.

Test	Time [μ s]	Amplitude [V]
Figure A3.1	6.68	2.27
Figure A3.2	6.78	3.53
Figure A3.3	6.95	3.78
Figure A3.4	7.10	3.75
Figure A3.5	6.95	3.28

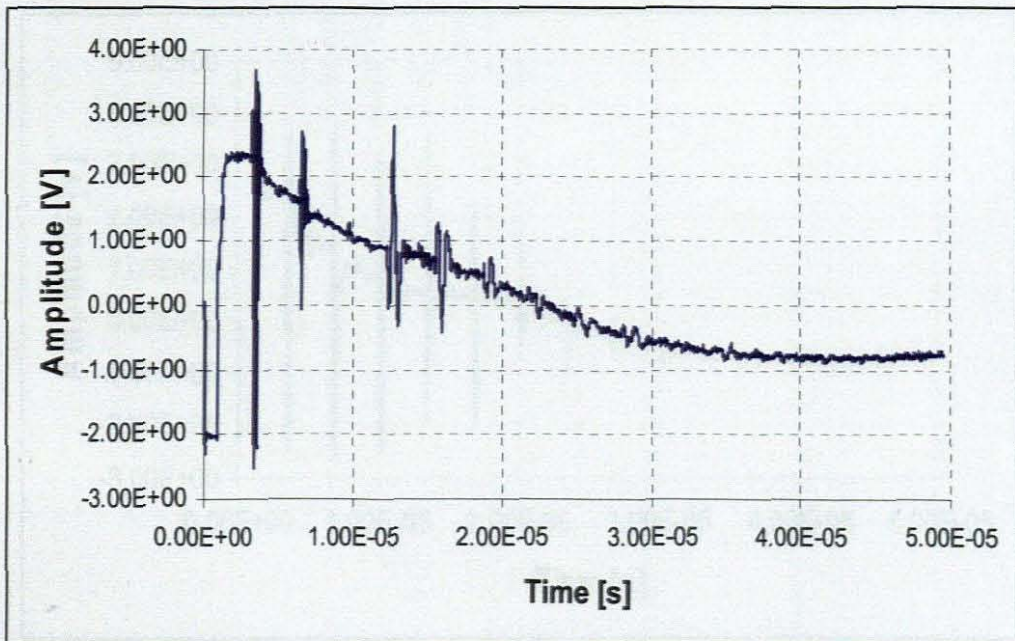


Figure A2.1 Ultrasonic response spectrum from a filtration module immersed in water

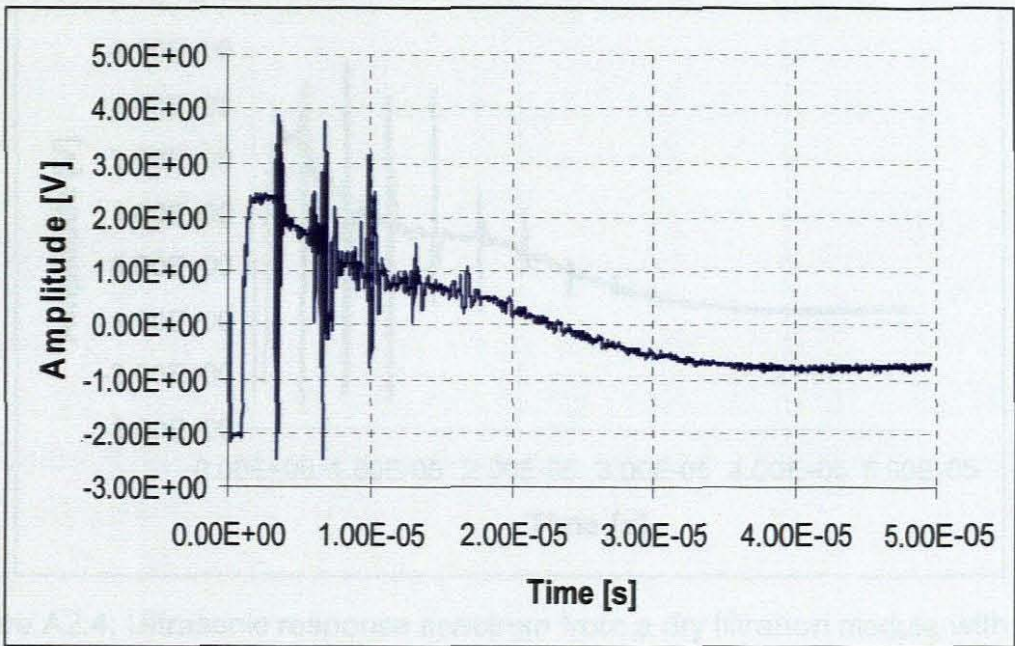


Figure A2.2 Ultrasonic response spectrum from a filtration module with a membrane immersed in water

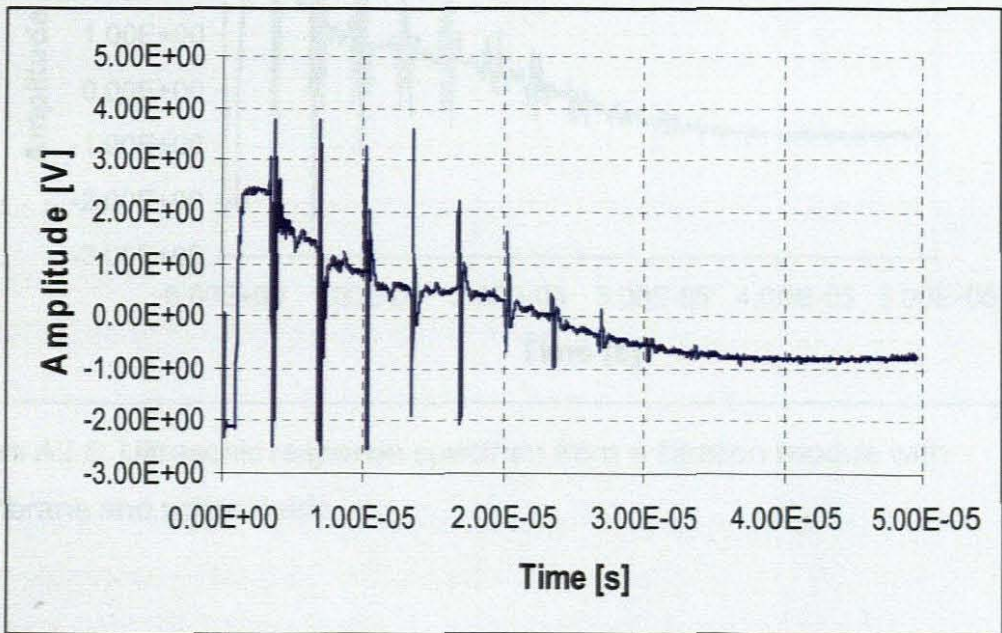


Figure A2.3: Ultrasonic response spectrum from a dry filtration module

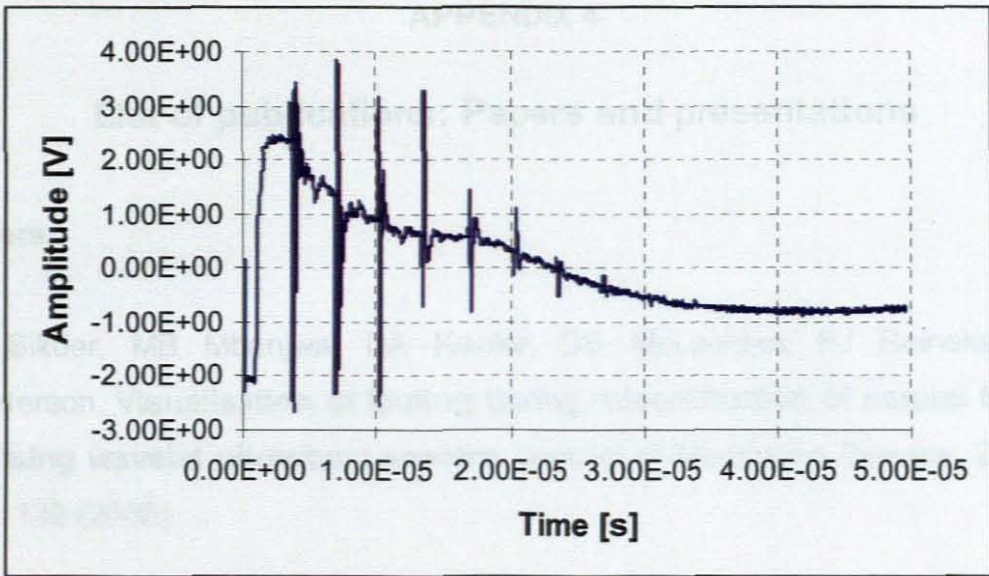


Figure A2.4: Ultrasonic response spectrum from a dry filtration module with membrane

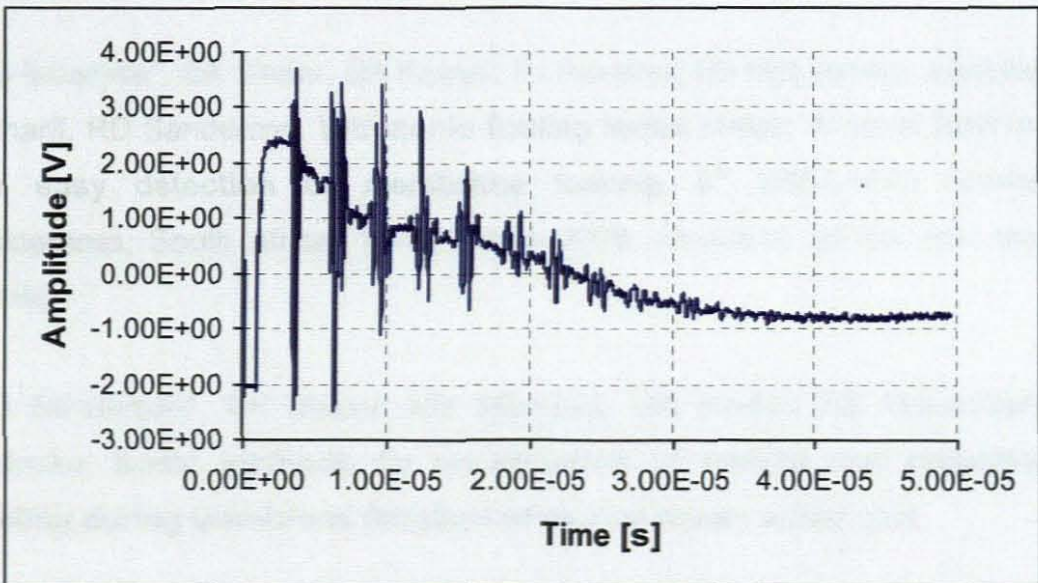


Figure A2.5: Ultrasonic response spectrum from a filtration module with membrane and water inside

microfiltration of beer brewing wastewater

MR Mbarika*, SK Sidiq, DA Kuyini, FJ Pieterse, M Mphahlele, M Mphahlele
 Detection and measurement of membrane fouling in cross-flow microfiltration
 using an ultrasonic technique – A review of literature, *Journal of Chemical
 Engineering R & D* 2005, University of Cape Town, Cape Town, South Africa, 3
 June 2005 (poster)

APPENDIX 4

List of publications: Papers and presentations

Papers:

SK Sikder, MB Mbanjwa, DA Keuler, DS McLachlan, FJ Reineke, RD Sanderson. **Visualisation of fouling during microfiltration of natural brown by using wavelet ultrasonic spectra.** Journal of Membrane Science, 271 pp 125- 139 (2006).

Presentations:

MB Mbanjwa*, SK Sikder, DA Keuler, FJ Reineke, DS McLachlan, J Schiller, W Scharff, RD Sanderson. **Ultrasonic fouling index meter: A novel instrument for easy detection of membrane fouling.** 6th WISA-MTD Workshop, Wilderness, South Africa, 13-15 March 2005. (Awarded as the best student paper).

RD Sanderson*, SK Sikder, MB Mbanjwa, DA Keuler, DS McLachlan, FJ Reineke. **Sonic methods for visualisation of fouling and reduction of fouling during membrane filtration of natural brown water.** Ibid.

SK Sikder*, MB Mbanjwa, DA Keuler, DS McLachlan, FJ Reineke, RD Sanderson. **Wavelets-based ultrasonic method of visualising fouling in microfiltration of beer-brewing wastewater.** ibid

MB Mbanjwa*, SK Sikder, DA Keuler, FJ Reineke, RD Sanderson, MS Sheldon. **Detection and measurement of membrane fouling on commercial modules using an ultrasonic technique – A review of viability.** SAICHe, Chemical Engineering R & D 2005, University of Cape Town, Cape Town, South Africa, 3 June 2005. (poster)